Materials Science and Engineering R 101 (2016) 1–38

Contents lists available at ScienceDirect

Materials Science and Engineering R

journal homepage: www.elsevier.com/locate/mser

Thin-film semiconductor perspective of organometal trihalide perovskite materials for high-efficiency solar cells

Zhengguo Xiao, Yongbo Yuan, Qi Wang, Yuchuan Shao, Yang Bai, Yehao Deng, Qingfeng Dong, Miao Hu, Cheng Bi, Jinsong Huang *

Department of Mechanical and Materials Engineering and Nebraska Center for Materials and Nanoscience, University of Nebraska-Lincoln, Lincoln, NE 68588-0526, USA

ARTICLE INFO

Article history:
Available online

Keywords:
Organometal trihalide perovskites
Optoelectronic property
Solar cells
Efficiency enhancement
Morphology control
Photocurrent hysteresis
Stability

ABSTRACT

Organometal trihalide perovskites (OTPs) are arising as a new generation of low-cost active materials for solar cells with efficiency rocketing from 3.5% to over 20% within only five years. From "dye" in dye-sensitized solar cells (DSSCs) to "hole conductors" and "electron conductors" in mesoscopic heterojunction solar cells, there has been a dramatic conceptual evolution on the function of OTPs in photovoltaic devices. OTPs were originally used as dyes in Grätzel cells, achieving a high efficiency above 15% which, however, did not manifest the excellent charge transport properties of OTPs. An analogy of OTPs to traditional semiconductors was drawn after the demonstration of highly efficient planar heterojunction structure OTP devices and the observation of their excellent bipolar transport properties with a large diffusion length exceeding 100 nm in $CH_3NH_3PbI_3$ ($MAPbI_3$) polycrystalline thin films. This review aims to provide the most recent advances in the understanding of the origin of the high OTP device efficiency. Specifically, we will focus on reviewing the progress in understanding (1) the characterization of fantastic optoelectronic property of OTPs, (2) the unusual defect physics that originate the optoelectronic property, (3) morphology control of the perovskite film from fabrication process and film post-treatment, (4) device interface and charge transport layers that dramatically impact device efficiency in the OTP thin-film devices, (5) photocurrent hysteresis, (6) tandem solar cells and (7) stability of the perovskite materials and solar cell devices.

Contents

* Corresponding author. Tel.: +402 472 2640; fax: +402 472 1465.
E-mail address: jhuang2@unl.edu (J. Huang).

http://dx.doi.org/10.1016/j.mser.2015.12.002
0927-796X/

1. Introduction

Organometal trihalide perovskites (OTPs) are emerging as a new generation of solution processable photovoltaic materials which are low-cost and nature-abundant [1–16]. The OTP materials have a typical three-dimensional (3D) perovskite structure with chemical formula of ABX_3, where A is the organic cation, B is lead (Pb), tin (Sn) or germanium (Ge), and X represents halide. The two-dimensional (2D) OTP materials were first used for thin-film transistors in the early 1990s pioneered by Mitzi [17,18]. In 2009, Miyasaka et al. used $CH_3NH_3PbI_3$ and $CH_3NH_3PbBr_3$ to replace organic dyes in the dye-sensitized solar cells (DSSCs) for the first time, where the mesoporous titanium oxide (TiO_2) and a liquid electrolyte were used, with the device structure shown in Fig. 1a [3]. A power conversion efficiency (PCE) of 3.8% was achieved. Two years later, Park et al. increased the efficiency of

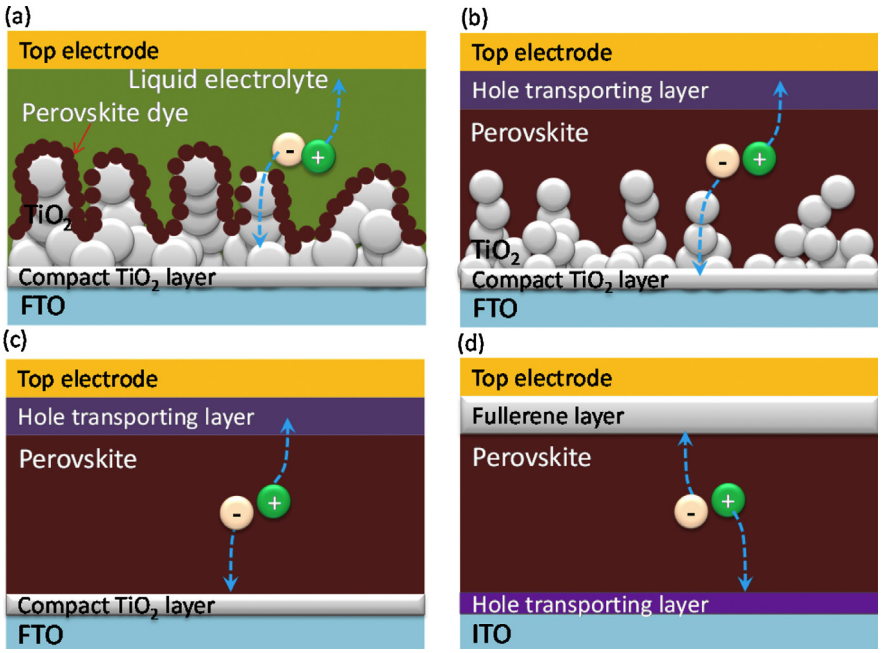

Fig. 1. (a) Liquid DSSC structure perovskite solar cells with mesoporous TiO_2 layer and liquid electrolyte where the perovskite material worked as a sensitizer. (b) Solid-state DSSC structure perovskite solar cells with mesoscopic TiO_2 layer. (c) N-i-p planar heterostructure perovskite solar cells with a compact TiO_2 layer. (d) P-i-n planar heterostructure perovskite solar cells with a flat hole transporting layer at the bottom and fullerene transporting layers at the top.

$CH_3NH_3PbI_3$-sensitized solar cells to 6.5% [19]. The next breakthrough occurred in 2012 when the solid-state hole transporting layers was used to replace liquid electrolyte. Park et al. reported 9.7% efficiency by using mesoporous TiO_2 as the electron transporting layer and solid organic small molecule 2,2′,7,7′-tetrakis(N,N-di-p-methoxyphenyl-amine)-9,9′-spirobifluorene (spiro-OMeTAD) as the hole transporting layer [20]. Almost at the same time, Snaith et al. reported an efficiency of 10% in the mesoporous structure device by replacing mesoporous TiO_2 with aluminum oxide (Al_2O_3) [4]. What really made these new materials attracted a broad interest from photovoltaic society is the quick rising of the device efficiency since 2013. Gratzel et al. reported that a two-step sequential deposition process, PbI_2 first and then CH_3NH_3I, could form high quality perovskite film in the solid-state DSSC devices, yielding a certified device efficiency close to 15%. Snaith et al. also demonstrated a high efficiency of 15% but in planar heterojunction structure solar cells where the mesoporous TiO_2 layer was replaced with only a compact TiO_2 layer [2]. The schematics of the mesoporous structure and planner structure devices are shown in Fig. 1b–c. This was a very exciting result which indicates that the perovskites are bipolar semiconductor materials, and OTP solar cells can be category of traditional inorganic thin-film solar cells. Jeng et al. first applied OTP to the traditional planar heterojunction organic photovoltaic structure by replacing organic donor material with $MAPbI_3$, yielding a device efficiency of 3.9% [8]. We increased the PCE to above 15% using this structure within several months by forming continuous and pin-hole free perovskite films using a two-step interdiffusion process [21] and double-layer fullerene electron acceptors [22]. The schematics of the device structure are shown in Fig. 1d. This is an important progress in that it allows the adoption of the established knowledge, materials, infrastructure for scaling up and manufacture in the last two decades of organic photovoltaic research and development into OTP solar cell research.

A PCE close to 20% has been achieved in both mesoporous structure devices as well as PHJ devices recently [23–25]. The highest certified efficiency has reached 20.1% (non-stabilized) in late 2014 [24]. Fig. 2 shows the PCE table of several types of thin-film photovoltaics. It took less than five years for the efficiency of perovskite solar cells to increase from 3.8% to above 20%, while it takes several decades for other kinds of inorganic solar cells to achieve this and most photovoltaic materials never reach 20% efficiency. In addition to the vacuum deposition process, the OTP materials can be processed in some polar solvents like N,N-Dimethylformamide (DMF), Dimethyl sulfoxide (DMSO), and gamma-Butyrolactone (GBL) etc., so that they can be deposited by using low-cost solution process at a low temperature of less than 150 °C [26,21,6].

After the demonstration of very high device efficiency out of these OTP materials, the unique optoelectronic properties that give rise to the very high photovoltaic performance have being slowly squeezed out. These attractive optoelectronic properties for photovoltaic applications mainly include: (1) The OTP materials are almost the best solar absorbers, with light absorption coefficient larger than almost all other existing inorganic thin-film PV absorbers. (2) The OTP materials have appropriate optical bandgap. The bandgap of the perovskite materials can be tuned from 1.20 eV for $CH_3NH_3SnI_3$, to 1.55 eV for $CH_3NH_3PbI_3$, to 3.1 eV for $CH_3NH_3PbCl_3$ using the alloys [28,29]. (3) The OTP materials easily form crystals, either from solution process or other vapor deposition processes [1,2,21]. (4) The OTP materials have large and balanced electron and hole mobilities as well as long carrier diffusion lengths [12,14,30]. The carrier mobility measured by Hall effect was estimated to be in the order of 10–200 $cm^2/V\,s$ for $CH_3NH_3PbI_3$ polycrystalline films and single crystals [30,31], due to the small electron and hole effective mass [32]. The carrier diffusion length is reported to be longer than their optical absorbing length in both solution processed $CH_3NH_3PbI_3Cl_{3-x}$ and $CH_3NH_3PbI_3$ polycrystalline films [33]. (5) $CH_3NH_3PbI_3$ has an exciton binding energy smaller than 50 meV [34,35], so that free charges can be easily generated after light excitation. (6) The OTP materials have unique defect properties with only shallow point defects formed while most of the traps stay in the conduction and valance bands. The deep charge traps, however, have too large formation energy barrier to be formed [36]. (7) There is possible ferroelectricity of $MAPbI_3$ which enables fast extraction of free charges by the fast channels, while the existence of ferroelectricity is still under debate [37,38].

Although the PCE of perovskite solar cells have been increased dramatically to 20.1% which is close to that of single crystal solar cells, there are still many major challenges for this type of solar cells before they can be commercialized. One challenge is the toxicity of the lead, although alternative metals such as Sn has been attempted to replace Pb. Another grand challenge is its instability, including both extrinsic and intrinsic instability. This review focuses on the understanding why the OTP materials work so well

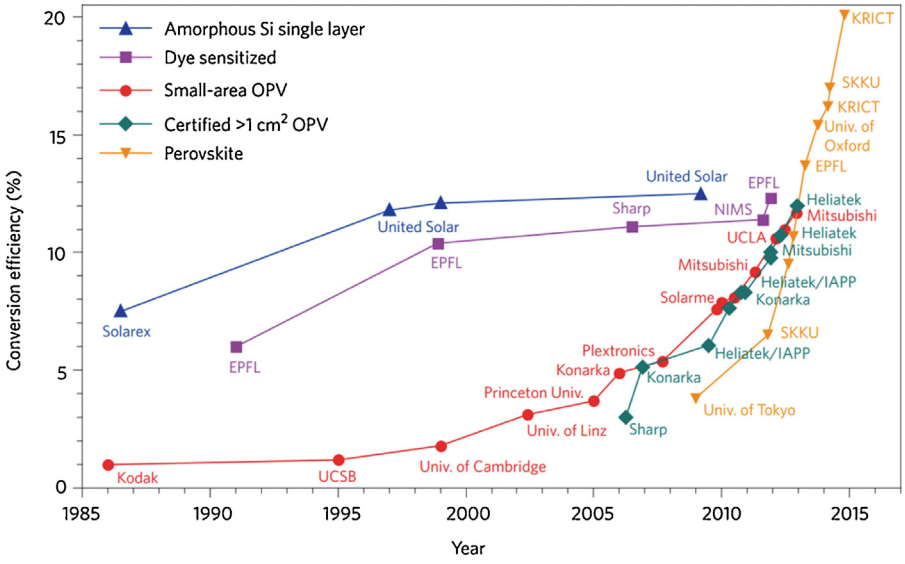

Fig. 2. Power conversion efficiency table for thin-film solar cells [27].

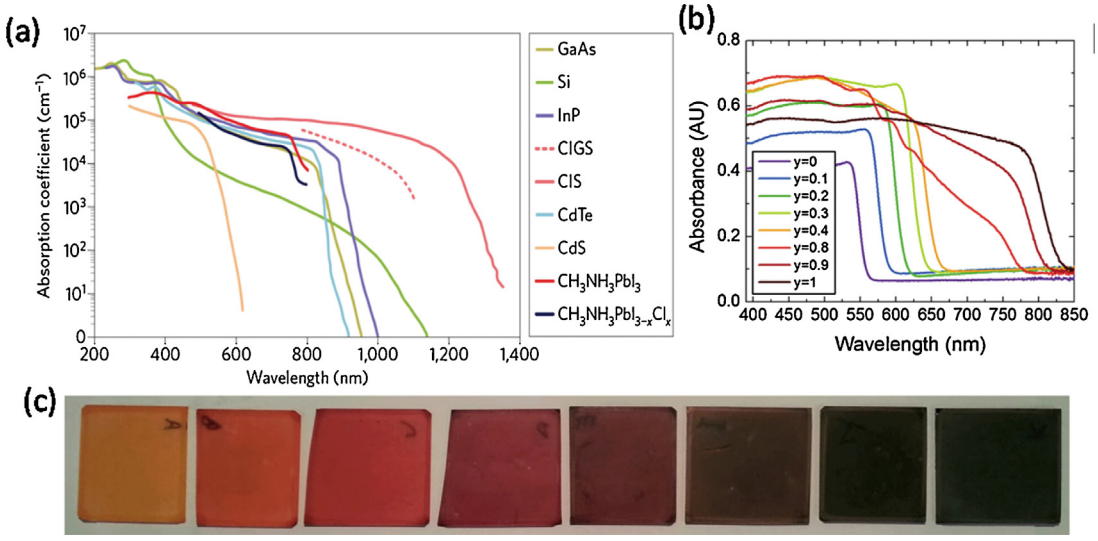

Fig. 3. (a) Absorption coefficient of $CH_3NH_3PbI_3$ and $CH_3NH_3PbI_{3-x}Cl_x$ compared to other solar cell materials [33]. (b) UV–Vis absorbance of the $FAPbI_yBr_{3-y}$ perovskites with varying y, measured in an integrating sphere. (c) Photographs of the $FAPbI_yBr_{3-y}$ perovskite films with y increasing from 0 to 1 (left to right) [39].

from the aspects of the thin-film solar cells. Starting from its optoelectronic properties, all aspects that influence the performance of perovskite solar cells will be reviewed including defects and traps, perovskite film fabrication techniques and morphology control, interfacial layers, etc.

2. Optoelectronic properties of OTPs

2.1. Absorption and bandgap

A good photovoltaic absorber needs to have strong absorption over a wide range of spectrum to minimize the amount of material usage and reduce charge and energy loss during extraction to electrodes. One superior property of the OTP materials to this end is its very high absorption coefficient with sharp onset of absorption edge. Material computation showed that the OTP materials are direct bandgap semiconductor materials [40]. As shown in Fig. 3a, OTPs materials have very high absorption coefficient compared with other inorganic thin-film photovoltaic materials. The absorption coefficient is above 3.0×10^4 cm^{-1} in the visible range, which indicates that the OTP material only needs 380 nm to absorb 90% of the visible light by taking into consideration the electrode reflection [33]. As a matter of fact, most of the reported high-efficiency devices had a thickness around 300–600 nm. The absorption edge of the $MAPbI_3$ film shows a very sharp onset which indicates the absence of deep states. The Urbach energy (slope of the exponential part of the absorption coefficient curve) of the $MAPbI_3$ film reached a low value of 15 meV, which is close to the monocrystalline gallium arsenide (GaAs) [41]. The sharp onset of the absorption edge can also explain the small offset between its optical bandgap (~1.55 eV) and V_{OC} of the solar cell device (~1.10 V).

Another advantage of the OTP materials is the maneuverability of its bandgap. The bandgap can be tuned by changing the atoms at any sites of A, B or X in the ABX_3 structure. It is established that the corner-sharing BX_6 octahedral plays a major role in determining the band structure [33,42]. Theoretical calculations show that conduction band minimum (CBM) of $CH_3NH_3PbI_3$ is mainly from Pb *p* orbital with negligible coupling with I *s* orbital, and the valance band maximum (VBM) has strong Pb *s* and I *p* antibonding character [36,43,44]. Nevertheless, the size of A cation also plays an important role in controlling the B–X bond length and electron cloud overlap between B and X atoms. A larger or smaller A cation can cause the whole lattice to expand or contract [39]. A longer B–X bond length induces the reduction of the electron cloud overlap between B and X atoms, which causes the decreased bandgap. Eperon et al. first used a slightly larger formamidinium cation (FA^+) to replace MA^+, the bandgap was reduced from 1.55 to 1.48 eV, corresponding to an absorption edge shift from 800 nm to around 840 nm [39]. The formamidinium lead iodide ($FAPbI_3$)-based perovskite solar cell devices delivered a photocurrent of 23 mA/cm^2 due to the extended light absorption. On the contrary, a smaller cesium cation (Cs^+) at A site causes the bandgap to increase to 1.73 eV [39]. For the X halide site, by replacing I^- with Br^- or Cl^-, the bandgap can be tuned from 550 nm for $MAPbBr_3$ to 400 nm for $MAPbCl_3$, respectively. Fig. 3b–c shows the continuous tuning of the optical bandgap of $FAPbI_yBr_{3-y}$ ($0 \leq y \leq 1$) based materials [39]. It is clear that the absorption edge was tuned from 840 nm for $FAPbI_3$ to 550 nm for $FAPbBr_3$ perovskite. For the metal B site, experiment results showed that larger B cation size results in increased bandgap. The bandgap of the $MAPbI_3$ was decreased to 1.2 eV by replacing the Pb^+ with smaller Sn^+ [28]. Similarly, the bandgap of the cesium lead iodide ($CsPbI_3$, 1.67 eV) was decreased to 1.30 eV for cesium tin iodide ($CsSnI_3$) and 1.08 eV for cesium germanium iodide ($CsGeI_3$) [28,45]. The trend of the bandgap change with respect to each atom size of the perovskite structure is shown in Fig. 4.

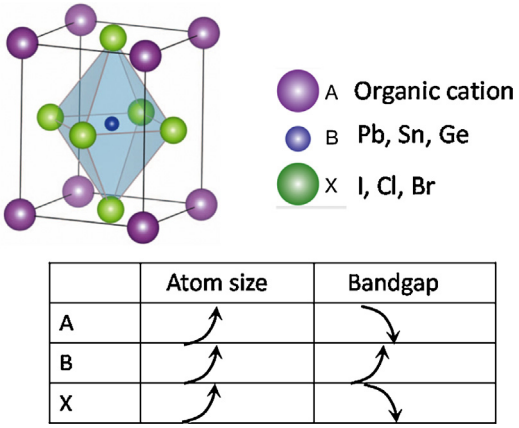

Fig. 4. Bandgap tuning of the perovskite by change the atom size of different sites in the perovskite structure.

There is continued and likely increasing research activity in the material composition discovery in the future for the purpose of bandgap tuning, removing toxic Pb and improve material's water stability. It should be noted that the sizes of A, B and X ions should fulfill the requirement of both tolerance factor t and octahedral factor μ in order to form 3D perovskite, where $t = (R_A + R_X)/\sqrt{2}(R_B + R_X)$ (R_A, R_B and R_X are the ionic radii of the corresponding ions), and $\mu = R_B/R_X$ [33]. Generally, the range of t and μ values are: $0.81 < t < 1.11$ and $0.44 < \mu < 0.90$, respectively [33].

2.2. Exciton binding energy

The hybrid nature of OTP material naturally renders one wonder whether incident photon generate free charges like in regular inorganic thin-film semiconductor, or bound excitons like in organic exciton semiconductors. In this section, we review the recent progress in understanding of optoelectronic properties of OTP materials, including the dielectric constant, exciton binding energy and exciton dissociation mechanism.

The dielectric constant of a material determines the exciton binding energy by $E_B = \frac{\mu}{m_0}\frac{1}{\in^2}\frac{m_0 e^4}{2(4\pi\in_0)^2}$, where μ is the exciton effective mass, m_0 the electron mass, e the unit charge and $\in_0$ the vacuum permittivity [46]. To calculate exciton binding energy, the dielectric permittivity of $MAPbX_3$ has been experimentally measured by several methods, including optical absorption [46], magneto absorption [47] and impedance analyzer, etc. [48]. In Fig. 5a, Lin et al. have reported the real part of dielectric permittivity is about 35 at kHz range, and about 70 at the low frequency (20 Hz–3 kHz). These values were obtained by measuring two parameters in the dielectric function $\in = (n + ik)^2$, refractive index (n) and extinction coefficients (k), by combining spectroscopic ellipsometry and total transmittance and near-normal incidence reflectance. This result is consistent with the dielectric constant measured by electrochemical impedance spectroscopy (EIS) at room temperature [49,50]. The challenge of EIS method is to obtain a high quality pin-hole-free perovskite thin film to avoid any leakage. Besides the experimental characterization, dielectric constant has also been theoretically analyzed by ab initio molecular dynamic simulation [51] and by polarization calculation [48]. Both calculations reported a dielectric constant of about 25, which agrees well with the experimental results at a high-frequency range, but smaller than the static dielectric constant. This is likely originated from the ionic dielectric response at low-frequency range.

The dynamic dielectric property upon the external stimuli is an exotic character for OTP hybrid compounds than the inorganic semiconductors. The MA ion has a permanent electric dipole moment, which could experience extremely rapid reorientation along C–N axis in the perovskite structure [52,53]. This dynamic dipole moment introduces the possibility of orientation polarization, which contributes to the dielectric response. A discontinuous dielectric constant of OTP has been observed at the phase transition temperature, which confirms the correlation between the dielectric permittivity of OTPs and the dynamic motion of MA ion dipole [47,49]. Being confident on this, the dielectric relaxation time was estimated by measuring MA cation rotational relaxation time of 5.7 ps [54]. Besides temperature-induced phase transition, the external stimuli, such as incident light and charge injection, also induced a huge change on dielectric permittivity of OTP materials. This was explained by the tilting and rotation of the BX_6 polyhedra in ABX_3 structure, under the stimuli including temperature and electric field [48,55]. A carrier induced giant dielectric constant (GDC), was reported by Bisquert et al. in $MAPbI_3$ [49]. The real part of the dielectric constant is over 1000 in the dark low-frequency region (shown in Fig. 5b) and increases 1000 times under illumination. Such high dielectric constant results in a large capacitance which is reported to be one of the main factors contributing to the slow impedance response in the low-frequency region [56]. However, such a GDC might come from measurement artifacts because it has been frequently observed in other materials with a lot of charge traps. Another possibility of the GDC is due to the ion migration, which has been simulated by Meredith, as shown in Fig. 5b.

The photogenerated species of OTP materials has been investigated by several studies. The large dielectric constant in OTP discussed above suggests the dielectric screening must be too strong to form an exciton. However, it has also been observed that exciton peaks rise in the optical absorption spectrum of OPTs at both room temperature and low temperature [47], which indicates that OTPs are plausibly excitonic materials. As a consequence, the exciton dissociation might be one of the reasons for energy loss which reduces device V_{OC}. The binding energy of the lowest energy exciton of $MAPbI_3$ was determined to be about 45 meV at room temperature from temperature dependence of luminescence intensity, indicating a Wannier–Mott type exciton [34,47]. A lower value of 16 meV at low temperature orthorhombic phase was also reported recently by Kutes et al., which was measured by using high magnetic fields inter-band magneto-absorption [35]. The reported exciton binding energy continued to fall to only a few meV when $MAPbI_3$ transits from orthorhombic to the tetragonal phase, which occurs above 160 K [35].

The photogenerated species are hard to be determined by evaluating the exciton binding energy, since it varies from a few meV to 45 meV. Thus this question has been investigated from device aspects. The fraction of free charges over the total density of excitation was reported by D'Innocenzo et al., which is shown in

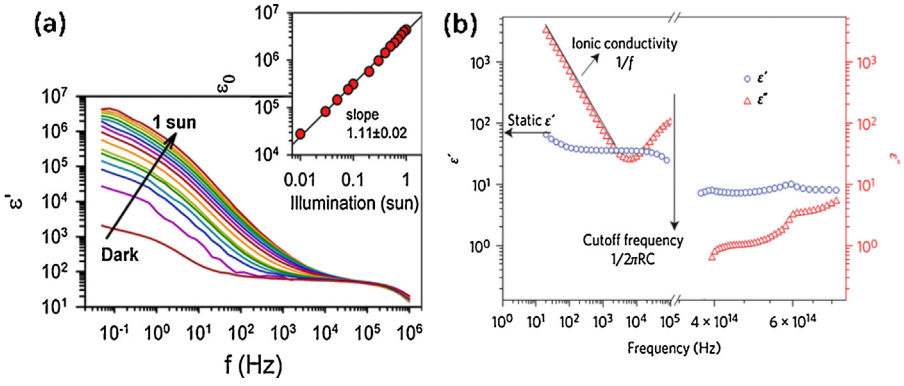

Fig. 5. (a) Real and imaginary parts of dielectric constants of $MAPbI_3$, in the optical (high) frequency regime as determined from n, k and low-frequency and static values from impedance analysis and CELIV [46]. (b) Plot of the real permittivity as a function of frequency for different incident light intensity from dark to one sun, for $MAPbI_{3-x}Cl_x$ perovskite at room temperature [49].

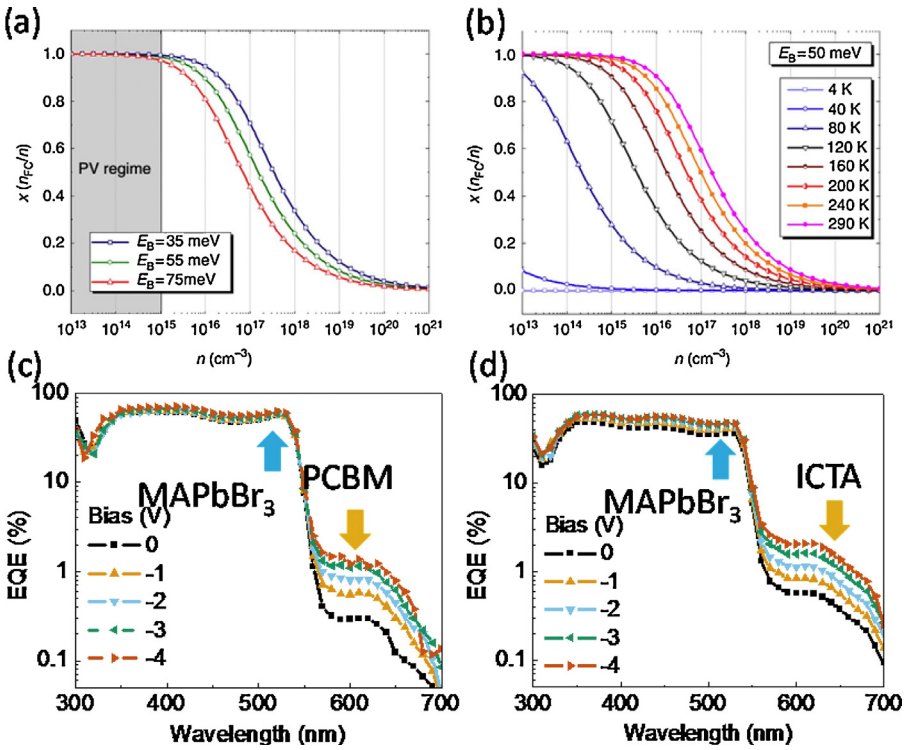

Fig. 6. (a) Simulation of the free charge fraction over the total excitation density with an exciton binding energy of (55 ± 20) meV; (b) Simulation of the free charge fraction over the total excitation density with different temperature [57]. External quantum efficiency (EQE) spectra of the $MAPbBr_3$ devices with different electron collection layers of PCBM; (c) ICTA; (d) Under the increasing reverse bias from 0 to −4 V; EQE signals between 560 and 700 nm are contributed by fullerenes.

Fig. 6a–b [57]. The simulation of the ratio of free charge in total excitation density was carried out with various exciton binding energy as shown in Fig. 6a. However, free charge dominates the photogenerated species at photovoltaic working conditions, even though the exciton binding energy was estimated to be 75 meV, which is larger than the room temperature thermal activation energy [57]. Fig. 6b shows that the exciton population starts to increase with decreasing temperature, becoming dominant below 120 K.

The exciton binding energy was found by us to be different for different halide perovskite. By measuring the full width at half-maximum of the exciton absorption peaks [58], the exciton binding energy of $MAPbBr_3$ was estimated to be 80 meV, which is larger than that of $MAPbI_3$ [50]. The exciton dissociation dynamics was studied by comparing electric field dependent incident photon to charge carrier efficiency (IPCE) of $MAPbBr_3$ and the conventional excitonic semiconductors in the same device (shown in Fig. 6c–d) [50]. It was observed that the excitons in $MAPbBr_3$ could get a maximum dissociation without any external field or heterogeneous interface, while exciton dissociation in excitonic materials, like Phenyl-C_{61}-butyric acid methyl ester (PCBM) and indene-C_{60} trisadduct (ICTA), was strongly field dependent [50]. These results indicate that OTP photovoltaic cells should be treated as traditional inorganic thin-film photovoltaic devices rather than organic or hybrid ones.

The recombination kinetics of excitons in OTP was reported by Samuel et al. [59]. The time dependent photoluminescence results with different excitation intensity indicate that the charge-trapping pathways limit the photoluminescence quantum efficiency at low fluence, while radiative bimolecular recombination dominates the photogenerated species' recombination when the excitation light is enough to fill the trap states. An analytical model was also build to lead a conclusion that both free charges and small amount of excitons were presented taking the consideration of the presence of electronic subgap trap states [59].

2.3. Charge carrier mobility

One important reason for OTP working as promising photovoltaic materials is their high charge carrier mobilities. Up to now, the mobilities of the perovskite materials have been studied by several methods such as Hall effect measurement, time of flight (TOF) measurement and transient photoconductivity measurement, which gives a spectrum of mobility value from 10 to 2000 cm^2/V s (Table 1) [28,30,60–62]. In this section, the mobilities of some common perovskite materials are first reviewed and summarized, and the factors influencing measured carrier mobilities are discussed.

2.3.1. Hall effect measurement

The Hall effect was first discovered in 1879 by Edwin H. Hall, which enabled a direct measurement of the charge carrier polarity and concentration in materials. After knowing carrier concentrations, carrier mobilities can be calculated as the material's conductivity can be measured at the same configuration by Van der Pauw method, hall bar method or else. Hall effect measurement is a routine method in the electrical characterizations of most of the semiconductor materials.

Up to now, the highest measured mobility value in perovskite materials was the electron Hall mobility of $MASnI_3$ crystal (2320 cm^2/V s) [28]. This μ_e value is similar to theoretical value (1300–2700 cm^2/V s) calculated by He et al. with a simplified Kane model [63]. Meanwhile, the Hall mobility of holes in $MASnI_3$ was around 322 cm^2/V s at a carrier concentration of 10^{15} cm^{-3}, which is however much smaller than the predicted value of 1400–3100 cm^2/V s at a carrier concentration between 10^{19} cm^{-3} and 10^{16} cm^{-3} [63]; the reason for this much smaller hole mobility than prediction is unknown yet. Although it has been reported that the mobility in perovskite crystal can be influenced by its synthetic approach [28], the hole mobility of $MASnI_3$ single crystal measured by another group was also around 200 cm^2/V s [65]. High hole

Table 1
Mobility of OTP materials obtained by different measurement.

Materials	Theoretical μ (cm^2/V s)		TPD μ (cm^2/V s)		Hall μ (cm^2/V s)		TFT μ (cm^2/V s)		SCLC μ (cm^2/V s)		TOF μ (cm^2/V s)	
	p	*n*	*p*	*n*	*p*	*n*	*p*	*n*	*p*	*n*	*p*	*n*
$CsSnI_3$					585 [61] (SC)	536 [28] (SC) 103 [28] (SC)						
$FASnI_3$												
$MASnI_3$	1400–3100 [63]	1300–2700 [63]	1.6/2 [64] ($\phi\mu$)	1.6/2 [64] ($\phi\mu$)	200 [65] (SC); 322 [28] (SC); 2000 [65] (50 K)	2320 [28] (SC)						
$MASn_{0.5}Pb_{0.5}I_3$						270 [28] (SC)						
$MAPbI_3$	800–1500 [63]; 1500–5500 [66]	1500–3100 [63]; 7000–30,000 [66]	8/2 [62] ($\phi\mu$)	8/2 [62] ($\phi\mu$)	105 [30] (SC); 114 [22]	66 [28] (SC)	~1 [67] (RT); 0.01 [68] (78 K)	~1 [67] (RT); 0.07 [68] (78 K)	164 [30] (SC); 2.5 [60] (SC)	24.8 [30] (SC)		24 [30] SC
$MAPbI_{3-x}Cl_x$			11.6/2 [62] ($\phi\mu$)	11.6/2 [62] ($\phi\mu$)								
$MAPbBr_3$					20–60 [60] (SC)				38 [60] (SC)		22–115 [60] (SC)	22–115 [60] (SC)
$(PEA)_2SnI_4$							0.62 [17]; 1.7 [69]					

TPD = transient photoconductivity; SC = single crystal; SCLC = spacing charge limited current; $\phi\mu$ is effective mobility, where ϕ is generated free charge/incident photons;

mobility of ~2000 cm^2/V s in $MASnI_3$ single crystal was only observed at a very low temperature of 50 K [65]. Nevertheless, much lower hole mobility is widely observed in some other inorganic semiconductors, such as Si (μ_e = 1350 cm^2/V s; μ_h = 600 cm^2/V s), GaAs (μ_e = 8000 cm^2/V s; μ_h = 400 cm^2/V s), GaP (μ_e = 1100 cm^2/V s; μ_h = 60 cm^2/V s), Gallium nitride (GaN) (μ_e = 1000 cm^2/V s; μ_h = 350 cm^2/V s), SiC (μ_e = 1100 cm^2/V s; μ_h = 50 cm^2/V s), InAs (μ_e = 40,000 cm^2/V s; μ_h = 500 cm^2/V s), InP (μ_e = 5400 cm^2/V s; μ_h = 200 cm^2/V s), InSb (μ_e = 77,000 cm^2/V s; μ_h = 850 cm^2/V s). The much lower hole mobility than electron mobility in $MASnI_3$ is not unusual if not compared with theoretical predictions.

When the Sn atoms in the perovskite were replaced by Pb atoms, based on the same theoretical work, the electron and hole mobilities were predicted to be on the same level, i.e., 1500–3100 cm^2/V s and 800–1500 cm^2/V s, respectively [63]. In another theoretical work, according to Wang's first principle calculation, the electron and hole mobilities in $MAPbI_3$ crystal were proposed to be even higher than 7000–30,000 cm^2/V s and 1500–5500 cm^2/V s, respectively [66]. The experiment results so far, showed the opposite trend. The electron and hole mobilities in $MAPbI_3$ single crystal were measured to be only 66 cm^2/V s and ~105 cm^2/V s, respectively [28,30]. This hole mobility measured by Hall effect is close to the value obtained from the fitting results of space charge limited current (164 cm^2/V s) [30].

In $MAPbBr_3$ single crystal, the Hall hole mobility was measured to be 20–60 cm^2/V s at a carrier concentration of ~10^{10} cm^{-3}. This value is comparable to the mobility obtained by time of flight method (22–115 cm^2/V s) [60]. When the MA^+ ions in $MASnI_3$ were replaced with Cs^+ ions, it formed all inorganic *p*-type perovskites ($CsSnI_3$) with a bandgap of 1.3 eV. Chung et al. measured the black phase of $CsSnI_3$ polycrystalline film by Hall effect, and found a high hole mobility of 585 cm^2/V s at a high carrier concentration of 10^{17} cm^{-3}, which cause the materials to have metallic behavior [61].

2.3.2. Time of flight measurement

Another routine method for characterizing carrier mobilities in semiconductors is TOF. TOF is a transient photocurrent technique which is more appropriate for low carrier mobility material characterization than Hall effect measurement. In a typical TOF configuration, the semiconducting material to be measured is sandwiched between two electrodes, one of which is transparent or semi-transparent so that incident excitation light can reach the semiconductor. This method requires thick semiconductor films for unambiguous measurement, because the charge transporting distance (film thickness) should be at least over one order of magnitude larger than the materials absorption depth (e.g., ~30 nm for $MAPbI_3$ at a wavelength of 337 nm). In addition, a low intensity optical excitation should be used to ensure that photogenerated charge carriers do not change the spatially uniformity of the built-in or applied electric field. Recently, the electron TOF mobility in $MAPbI_3$ single crystal with a thickness of 3 mm was reported to be around 24 cm^2/V s [30]. This TOF mobility is close to the mobility value obtained by Hall effect measurement and SCLC fitting [30]. The mobility in $MAPbBr_3$ with a thickness of 1.6 mm has been measured to be 22–115 cm^2/V s, which was assigned to both electron and hole mobilities but the geometry for this device structure only allows hole mobility measurement [60].

2.3.3. Transient photoconductivity measurement

Time-resolved terahertz spectroscopy (TRTS) measurement is a non-contact transient photocurrent technique. By using TRTS, Wehrenfenning et al. derived a mobility low limit of 8 cm^2/V s and 11.6 cm^2/V s for $MAPbI_3$ and $MAPbI_{3-x}Cl_x$ polycrystalline films,

respectively [62]. In this method, the photogenerated free charges cause a conductivity change (ΔS) in the perovskite films, which cause changes in THz transmission of the materials:

$$\Delta S = -\epsilon_0 c(n_A + n_B)(T_{Illuminated} - T_{Dark})/T_D \quad (2.1)$$

where, n_A and n_B are the refractive index of the media in each side of the perovskite film, T_D and $T_{Illuminated}$ are the transmitted terahertz electric fields in the dark and illuminating conditions, respectively. In order to get the charge carrier mobility from the obtained photoconductivity, the number of the photo generated charge carriers N was estimated by:

$$N = \phi \frac{E}{h\nu} Abs \quad (2.2)$$

where, E is the total energy of the pumping light in each excitation pulse, $h\nu$ is photon energy, Abs is the absorption of the pumping light and ϕ is the quantum yield of the free charge generation process caused by incident photons. Since the ϕ value is unknown, Wehrenfenning et al. used effective charge carrier mobility μ_{eff} in their study for discussion, which was derived to be:

$$\mu_{eff} = \phi\mu = \phi\Delta S A_{eff}/Ne \quad (2.3)$$

where, A_{eff} is the overlapping area between the spots of optical pumping light and THz probe light.

It should be noticed that TRTS do not distinguish conductivity contributions from holes or electrons. Hence, the obtained conductivity change is contributed by conduction of both holes and electrons, i.e., $\mu = \mu_h + \mu_e$. The mobility μ in materials is determined by the average scattering time τ_s and effective mass m^* of charge carriers, which can be expressed as: $\mu = q\tau_s/m^*$.

In some transient photoconductivity measurements, the μ_h and μ_e in $MAPbI_3$ was assumed to be half of the obtained μ since the effective mass of the photogenerated holes ($\sim 0.29m_0$) was considered to be similar with that of electrons ($0.22–0.23m_0$) [32]. On the other hand, Ponseca et al. provided an experimental approach to estimate the hole or/and electron mobility, respectively [70]. In this study, the electron conduction was minimized by grown perovskite film on mesoporous TiO_2 which extracted most of the photon generated electrons out of the perovskite films. Compared to the total mobility in a neat perovskite film (~ 20 cm^2/V s), the obtained mobility from the perovskite films on mesoporous TiO_2 (~ 7.5 cm^2/V s) was assigned to be hole mobility.

2.3.4. Field effect mobility

Field effect transistor (FET) is another widely used method to characterize the carrier mobility in semiconductor materials [71]. In FET, the charge carrier concentration is accurately controlled by applied gate bias; hence, the mobility can be extracted from the relationship between the channel conductivity and the applied bias. Transistors with layered perovskite materials based on SnI_2 framework, such as $(C_6H_5C_2H_4NH_3)_2SnI_4$, was reported 15 years ago by Mitzi et al. [17,69]. The layered perovskite film can be also fabricated by solution method such as spin coating or thermal evaporation [72]. The obtained hole mobility was around ~ 0.6 cm^2/V s, although the expected value could be over 50 cm^2/V s [17]. Later this FET mobility was improved to be 1.7 cm^2/V s by using melt processed deposition technique [69,73,74]. However, there are rarely reports on transistors based on bulk perovskite materials, such as $MAPbI_3$ and $MASnI_3$. A major problem is that the observed channel current in those transistors is usually in a very low level of 0.1 nA. Recently, Mei et al. fabricated $MAPbI_{3-x}Cl_x$ perovskite film on a 2,3,5,6-tetrafluoro-4-(trifluoromethyl) benzenethiol (TTFB) treated substrate with a cross-linkable fluoropolymer as dielectric layer. It is reported that the obtained perovskite has balanced hole and electron mobilities of ~ 1 cm^2/V s at RT [67]. Chin et al. measured the $MAPbI_3$ transistor at temperatures lower than 200 K and found a significant channel current [68]. At a low temperature of 78 K, the $MAPbI_3$ transistor showed a FET mobility of ~ 0.01 cm^2/V s for holes and ~ 0.07 cm^2/V s for electrons. In their study, the failure of observing FET mobility at room temperature was suggested to be related to a screening effect caused by mobile ions in $MAPbI_3$. This explanation is reasonable, because it has been shown by us that the ions in $MAPbI_3$ are readily to move at a weak electrical field of 0.3 V/μm, which are 2 orders of magnitude smaller than the field caused by gate bias [37,75]. One possible concern could be the grain boundary which might cause the carrier scattering, and thus resulting in low mobility of the small grain polycrystalline films. The grain sizes of perovskite polycrystals in these studies were reported to be around hundreds of nanometers to few micrometers, therefore a considerable number of grain boundaries are present in a transistor with channel length of 20–100 μm. However, recent study of single crystal perovskite mobility using thin-film transistor structure gave a slightly higher but similar level of mobility. This supports the low transistor mobility is intrinsically limited by the ion conduction of the hybrid halide materials, although the grain boundaries do have impact on the carrier transport mobility.

2.3.5. Factors influencing charge carrier mobility

The theoretical limit of carrier mobility is determined by the effective mass of the electrons and holes which is controlled by the energy band structure. Theoretical calculation by density function theory predicted very small while comparable effective mass of the electron and holes, which explained the large and balanced carrier mobility measured in experiments. Nevertheless, like any semiconductor materials, the carrier mobility of OTPs is also influenced by material's morphology and defects, although the impact of defects to carrier transport properties is much weaker in OTP materials than in many other traditional semiconductors. Here we summarized the process in understanding of material morphology on carrier mobility. Since it was reported point defects basically do not form deep traps in OTP bulk by Yan's computation [36], here we focus on the discussion of the influence of grain boundaries, phase impurity, carrier concentration, etc., on the carrier mobilities in OTPs.

In polycrystalline films, grain boundaries usually slow down charge transport because of its possible charge trapping and scattering effects caused by grain orientation, dislocations, dangling bonds or composition change at grain boundaries. According to Yan's first principle calculation, the structural disorders at the $MAPbI_3$ grain boundaries do not introduce deep trap states inside the forbidden band [76]. Our computation confirmed Yan's result that the stoichiometric surface or grain boundary does not induce mid-gap states; however, non-stoichiometric surface or grain boundaries did cause deep traps [77]. Since the OTP materials easily decompose at low annealing temperature while most perovskite films need to be annealed for grain growth, there is large chance to form non-stoichiometric perovskite at film surface and grain boundaries by losing the organic cations. A recent local optical study by Ginger et al. showed that the grain boundaries actually show weaker photoluminescence emission as well as shorter charge recombination lifetime as shown in Fig. 7, which directly confirmed that grain boundaries do have negative impact to the photogenerated charges [78].

In our initial study of carrier transport along lateral direction in polycrystalline film, we observed that grain boundary reduced carrier mobilities, while a grain boundary passivation can effectively recover the excellent charge transport properties even in polycrystalline films [22]. Lateral carrier transport was studied because the grain size in our perovskite films were generally

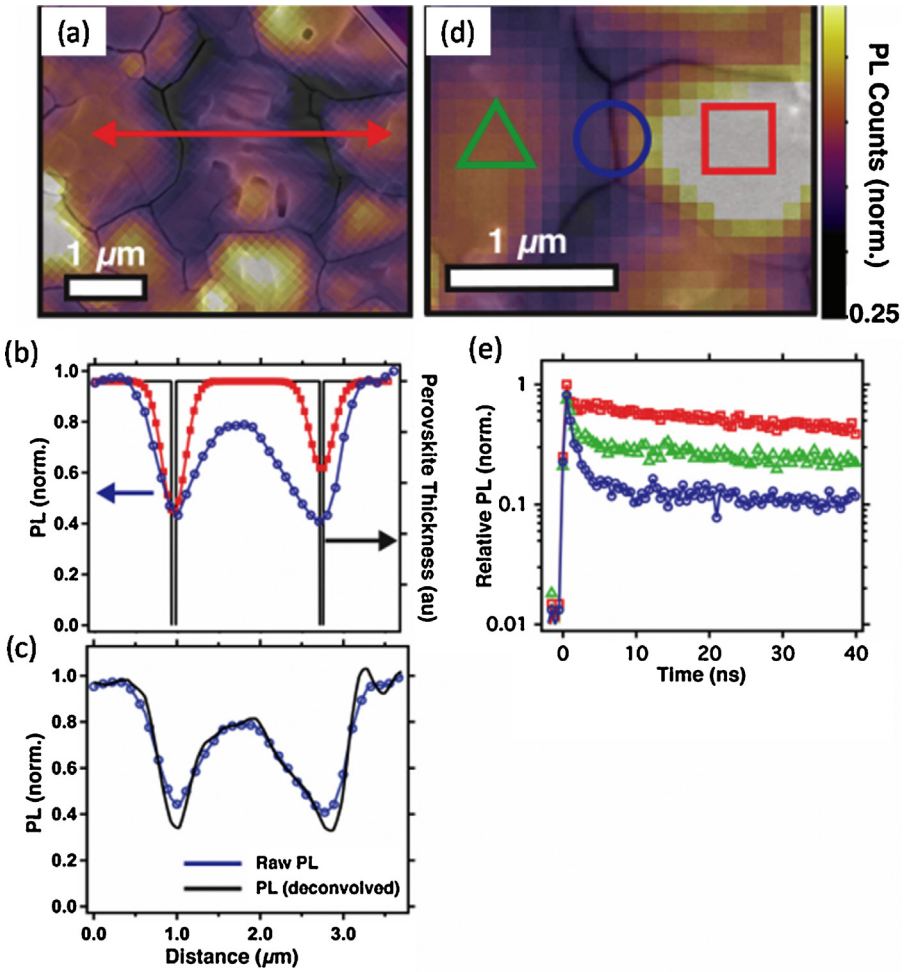

Fig. 7. (a) Fluorescence image with semi-transparent SEM overlay showing a line scan (red arrow) across two distinct grain boundaries. (b) Convolution data analysis showing at grain boundaries the half width at half max (HWHM) of the measured PL quenching trace (blue circles) is larger than the HWHM of the point spread function (PSF, red squares) convolved with the grain boundary width (black line). (c) Deconvolved the PSF from the raw PL quenching at the GB to determine the spatial extent (~210 nm) and absolute magnitude (~65%) of PL quenching. (d) Fluorescence image of $CH_3NH_3PbI_3(Cl)$ film on glass showing PL intensity variations at a bright grain (red square), grain boundary (blue circle), and dark grain (green triangle). (e) Time resolved photoluminescence traces showing grain boundaries (blue circle) quench PL significantly more than dark (green triangle) and bright regions (red square) [78] (For interpretation of the references to color in this figure legend, the reader is referred to the web version of this article.).

comparable or much larger than the film thickness, so that the carrier transport in vertical direction actually does not need to across a grain boundary [31]. Bi et al. experimentally shown that, in the polycrystalline $MAPbI_3$ film, the Hall mobility of holes was increased from 2.5 $cm^2/V\,s$ to around 30 $cm^2/V\,s$ after thermal annealing of perovskite films for 1.5 h. The increased mobility is mainly due to the increased crystallinity and average grain size of the perovskite films which reduced the grain boundary area. The grain size was increased from less than 190 nm to over 300 nm during heating process [21]. Later, Shao et al. showed that if the defects at the $MAPbI_3$ grain boundaries were passivated by PCBM, the hole mobility can be further increased to 114 $cm^2/V\,s$, which is the highest Hall mobility observed in polycrystalline $MAPbI_3$ films [22]. This mobility is comparable to the hole mobility obtained in $MAPbI_3$ single crystal (105 $cm^2/V\,s$), demonstrating the significance of grain boundary passivation [30]. Since all of the perovskite films formed by the two-step interdiffusion method are *p*-type, only hole mobility was studied by Hall effect measurement. Letjetns et al. compared the carrier transport behavior of the $MAPbI_{3-x}Cl_x$ perovskite films formed by infiltration into the mesoporous network and on flat solid films using the steady-state and transient photoconductivity [79]. It was found that the mobility of photo-generated carriers within the perovskite infiltrated into the mesoporous network is at least 1 order of magnitude lower than the mobility in the flat solid films (20 $cm^2/V\,s$), most likely due to the larger crystal grain size in flat solid films. It was noted that a high mobility of 10 $cm^2/V\,s$ was measured for meso-superstructured perovskite films using time-resolved terahertz spectroscopy. The large discrepancy of mobility measured was explained by that terahertz mobilities are local mobilities. We expect the terahertz mobilities is more related to band transport because the large frequency used in terahertz measurement does not allow the free carriers to across the grain boundaries. The nice part of the steady-state photoconductivity measurement is that it also gave the excitation light intensity dependent carrier mobility which is closely related the operation of solar cells. A reduction of carrier mobility at higher injection level was reported.

Similarly, the doping or background carrier concentration is also expected to have an impact to the carrier mobility in perovskite materials, which can vary by several orders of magnitude caused by the different fabrication processes. In $MAPbI_3$ polycrystalline films formed with pre-mixed perovskite precursors at different ratio, Qi et al. shown that the obtained Hall mobility has an inversely relationship with the carrier concentration. The mobility of the non-passivated perovskite films decreased from ~13 to ~2 $cm^2/V\,s$ when the carrier concentration increased

from $\sim 10^{15}$ to 4×10^{18} cm^{-3}. However, the contribution from morphology defects and composition defects is tangled with carrier concentration change in this study, and more study is needed to find out carrier concentration dependent carrier mobility in the future, once the doping of single crystal perovskite can be well-controlled.

The hybrid perovskite materials are known to have different phases, such as cubic, tetragonal and orthorhombic phase, which give clear absorption edge shifts in those materials [80]. However, the carrier mobility change around phase transition is relatively small. As for $MASnI_3$ single crystal, Takahashi et al. measured the charge transport properties at varied temperatures of from RT to 50 K, in which range the $MASnI_3$ single crystal show phase change from cubic to tetragonal and orthorhombic [65]. However, it turned out that the phase transition has no negligible effect on the hole mobility. In $MAPbI_3$ crystal, a first principle calculation shows that the hole/electron effective mass in tetragonal phase ($\sim 0.29m_0$/$\sim 0.20m_0$) is a little lower than that in orthorhombic phase ($0.39m_0$/$0.23m_0$), suggesting a slightly higher mobility in tetragonal phase [81]. Nevertheless, no obvious mobility change caused by phase transition has been found in $MAPbI_3$ experimentally. Similarly, in $CsSnI_3$ single crystal, the phase transition between orthorhombic and tetragonal does not give any noticeable conductivity changes [61].

3. Defects, traps and passivation in hybrid perovskites

The defects of semiconductor, ranging from point defect to grain boundary, are one of the most critical factors influencing optoelectronic properties and the efficiency of solar cells. Defects with shallow energy levels may donate carriers to conduction or valance bands to increase the semiconductor conductivity. In contrast, defects with deep energy levels usually serve as Shockley–Read–Hall recombination centers which are unfavorable for charge extraction in solar cells. The achievement of high efficient compound semiconductors solar cells using polycrystalline thin films, such as copper indium gallium diselenide (CIGS), is often attributed to benign defect property where deep defect formation is energetically unfavorable [82]. On the contrary, many III–V semiconductors, such as GaAs and GaN, are notorious for their intolerance to imperfections, and thus high purity and crystallinity are always required to obtain high device performance [82]. In the past five years, OTPs have drawn great research interests because of their superior carrier diffusion length [12,14,30,60], low charge recombination rate [62,83] and high device V_{OC}/E_g ratio [11]. All these characteristics indicate $CH_3NH_3PbI_3$ perovskite may have unique defect physics. Understanding of the defect nature of OTP materials is not only academic interest in recent years, but also bears great promise to rational design of more efficient and stable new perovskite photovoltaic materials. In this section, we review the recent understanding of zero to 2D defects in OTP materials from both theoretical and experiment points of views.

3.1. Point defects

First-principles calculation, which predicts material inherent properties based on atomic structure and the interaction of periodic potentials, is a powerful and widely used tool to reveal the point defect characteristics of semiconductors [32,36,40,82,84,85]. As for OTPs, many fundamental properties and parameters, such as absorption coefficient [40], carrier effective mass [32,86] and density of states and bandgap [36,85] have been investigated by first-principles calculation. In addition, the properties of defects in OTPs, such as formation energy and energy level, have been calculated [36,85]. Pioneering work by Yan et al. predicted that the dominant defects with low formation energy, e.g., the lead vacancy (V_{Pb}) and methylammonium interstitial (MA_i), only form shallow traps with a depth of less than 0.05 eV, as shown in Fig. 8 [36]. In contrast, defects with deep transition levels have high formation energies and thus unlikely exist in OTP crystals, which provided a theoretical explanation for low density of deep traps in OTP materials. They ascribed the unique defect properties of halide perovskite to the strong *sp* orbit antibonding coupling between lead *s* orbital and iodide *p* orbital and the high ionicity of the hybrid perovskites. The benign defects of perovskites were also reported by Hong et al., where PbI_2 and CH_3NH_3I Schottky defects were found to create only shallow traps [85]. The ionic bonding nature of $CH_3NH_3PbI_3$ perovskite was believed to be responsible for the absence of gap states.

An interesting prediction from Yan's theoretical calculations is that $MAPbI_3$ material can be self-doped by point defects to be either *n*- or *p*-type [36,85]. The formation energy of defects in the perovskite was believed to be intimately related to material growth condition. The defects with lowest formation energy for I-rich/Pb-poor condition and I-poor/Pb-rich condition were calculated to be lead vacancy and MA interstitial, respectively. These two defects were found to form either electron acceptor or electron donor, respectively, as shown in Fig. 8. In this case, a self-doping behavior, where electronic conductivity of perovskite can be tuned between *p*-type and *n*-type by film process conditions, was predicted. We independently observed the *p*- and *n*- type self-doping behavior before the publications of Yan's results [87]. In our efforts to optimize the morphology of perovskite films formed by one-step spin coating method, we found the doping concentration and type of the formed films were sensitive to the ratio of the precursors in the pre-mixed solution [22]. In this study, the molar

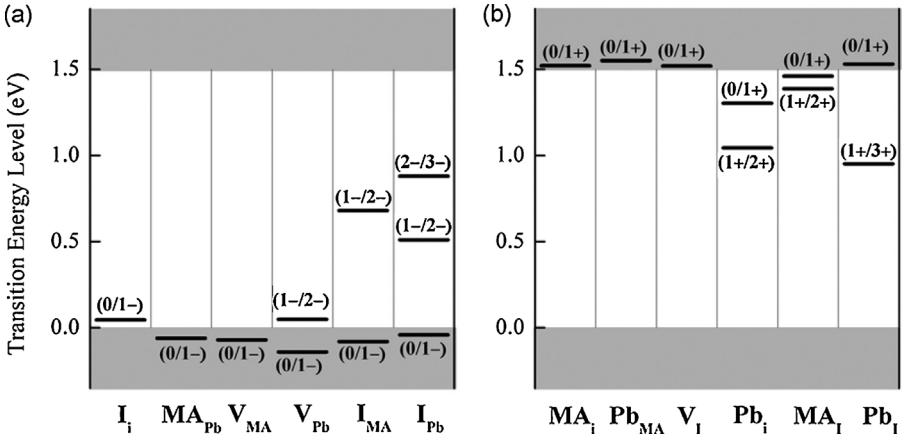

Fig. 8. Transition level of point defects in $MAPbI_3$ from DFT calculation: the intrinsic acceptors (a) and intrinsic donors (b) [36].

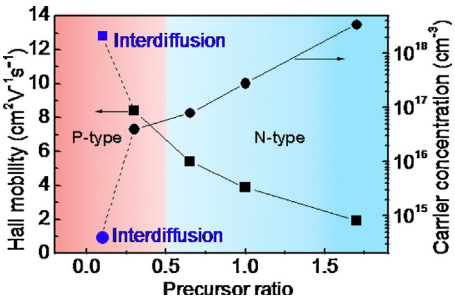

Fig. 9. Composition dependent carrier concentration (circle) and carrier mobility (square) in perovskite films formed by one-step pre-mixed precursor deposition (black) and two-steps interdiffusion method (blue) [87] (For interpretation of the references to color in this figure legend, the reader is referred to the web version of this article.).

ratio of PbI_2/MAI in the precursor solution was varied from 0.3 to 1.7. As shown in Fig. 9, the carrier concentration measured by Hall effect was tuned by 5–6 orders of magnitude. The films formed with PbI_2:MAI ratios larger than 0.5 in the precursor mixture were predominately *n*-type, and *p*-type behavior only occurs when PbI_2:MAI ratio was less than 0.35. This can be understood by the fact that MAI can be easily evaporated away during thermal annealing, leaving *n*-type MA interstitial which causes *n*-type of the films. Another piece of evidence is that thermal annealing of *p*-type perovskite at high temperature converted the films into *n*-type by evaporating MA. The films fabricated from one-step method with precursor ratio of 1.0 were heavily *n*-doped with a high electron concentration of $2.8 \times 10^{17}\ cm^{-3}$, agreeing with other studies [88,89]. The perovskite films made by interdiffusion method showed a weak *p*-doped behavior [21,22]. This can be understood by the facts that MAI is always in excess in the interdiffusion method. It is noted all the *p*-type films or single crystals reported have a low hole concentration less than $10^{16}\ cm^{-3}$.

Although the long carrier diffusion length in OTP materials may be benefited from its unique defect physics, how to calculate the perovskite defects accurately using first principle method is still under debate. It was reported that neglecting the spin orbit coupling could result in incorrect calculation of energy levels of conduction and valance band, as well as defect energy levels [42,90]. Some deep traps, such as iodide vacancy [91], iodide interstitial [86] and lead substitution by iodide [92] were predicted to have low formation energies. Strong covalent bonds were believed to exist and facilitate the formation of Pb dimer and I trimer which gave rise to deep transition levels within the bandgap of $CH_3NH_3PbI_3$ perovskite [36]. A consequence of the strong covalency is that some point defects with deep charge-state transition levels are very stable [91]. The controversies between these conclusions call for further studies with more insights about defect properties in perovskite materials. But from experimental perspective, the perovskite films made by low-cost solution process showed a low recombination rate and high mobility, which implies the large formation energy of the deep traps.

3.2. Surface defect, grain boundary and defect passivation

We demonstrated that there are a large density of trap states close to the surface of perovskite thin film or at the grain boundaries by photoluminescence (PL) and thermal admittance spectroscopy (TAS) measurements [21]. The large trap density may origin from the weak thermal stability of the perovskites [21,87]. Recent study also revealed that the grain boundary of $CH_3NH_3PbI_xCl_{3-x}$ perovskite films were dimmer with PL signals and exhibited faster non-radiative recombination [78]. In addition, perovskite single crystals with no grain boundary have a much longer carrier diffusion length than that of polycrystalline films [30,60]. All these experimental results imply the grain boundary of perovskite is not as benign as what has been predicted by calculation [40]. Therefore, like polycrystalline silicon, GaAs and Cadmium telluride (CdTe) solar cells, sophisticated passivation strategies are essential for increasing the efficiency of perovskite solar cells.

Our group reported a unique double fullerene structure (PCBM/C_{60}) to passivate traps in perovskite films and the device fill factor (FF) was significantly boosted to 80% for the first time in perovskite photovoltaic research, which is still among the highest reported FF values [21,22]. To examine the function of fullerene layers, TAS was conducted to estimate the trap density of perovskite devices with or without fullerene passivation [22]. As shown in Fig. 10a, a relatively large density of defect states on an order of $10^{18}\ m^{-3}\ eV^{-1}$ was found in the devices without fullerene passivation. After C_{60} or PCBM passivation, the trap density reduced dramatically, especially for traps with deep transition levels. It was found that C_{60} and PCBM have complementary passivation ability to the traps with different transition levels, which explains the role of the double fullerene layer in defects passivation and device performance improvement. However, it is still not clear yet why the subtle chemical structure difference of C_{60} and PCBM caused the large difference in passivation behavior, and more theoretical calculation is needed to this end. The fullerene passivation could also significantly suppress the notorious photocurrent hysteresis in perovskite solar cells, which will be discussed in Section 6.1. The capability of fullerenes in passivating

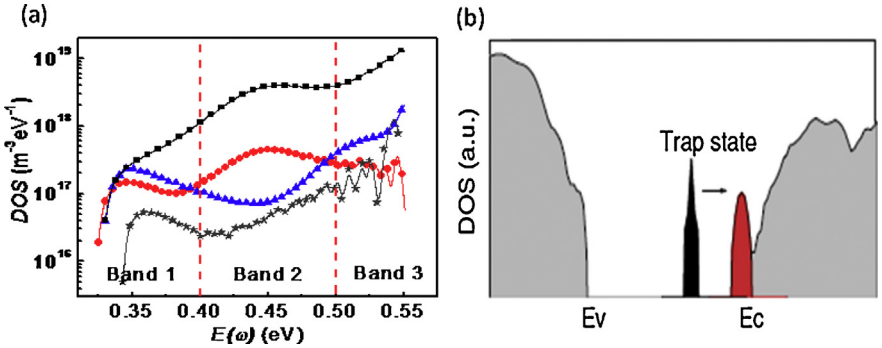

Fig. 10. (a) Trap density of states for OTP devices passivated by different fullerenes: single PCBM layer (blue triangles), single C_{60} layer (red dots), PCBM/C_{60} double fullerene layers (gray stars); black squares is for the devices without fullerene passivation [22]. (b) DFT calculation of density of states of Pb-I antistite defect (black); the trap becomes shallower (red) after reacting with PCBM. Ec, the minimum of conduction band; Ev, maximum of valence band [93] (For interpretation of the references to color in this figure legend, the reader is referred to the web version of this article.).

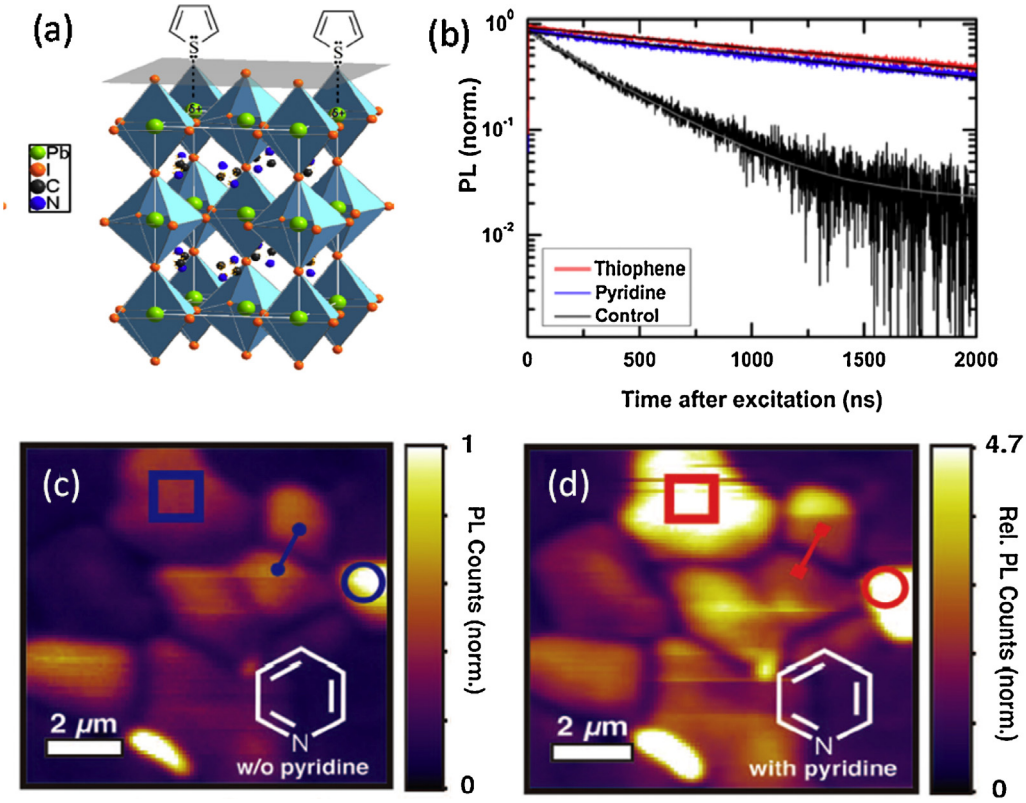

Fig. 11. (a) Possible mechanism of Lewis base passivation. Sulfur atom in Lewis base donate electron density to the Pb and form a coordinate or dative covalent [96]. (b) Time-resolved photoluminescence of perovskite films with thiophene (red), pyridine (blue) passivattion as compared to as-prepared films (black). Fluorescence images of perovskite film without (c) and with (d) pyridine vapor treatment [78] (For interpretation of the references to color in this figure legend, the reader is referred to the web version of this article.).

defects and suppressing hysteresis was later confirmed by several other groups [93–95]. Further study of fullerene passivation done by Sargent et al. suggested PCBM could passivate the PbI_3^- antisite defects at grain boundaries [93]. Density functional theory (DFT) calculation, shown in Fig. 10b, indicates that the deep trap states induced by Pb–I antisite defect become much shallower upon the adsorption of PCBM on defects, demonstrating the PCBM passivation effect in perovskites by reacting with excess-halide-associated defects.

Lewis base passivation was reported by Snaith et al. as another effective way to passivate traps in perovskite film surface and grain boundary [96]. They proposed the sulfur atoms in thiophene, or nitrogen atoms in pyridine, could passivate the un-coordinated Pb ions in the perovskite film via forming bond between sulfur (nitrogen) atoms in Lewis base with Pb ions, as shown in Fig. 11a. PL study showed that the perovskite films after Lewis bases passivation exhibited a decreased non-radiative recombination rate and a ~10 times increased PL lifetime, as shown in Fig. 11b. Recent fluorescence study of local grain and grain boundary further confirmed the effect of Lewis base passivation in suppressing non-radiative decay [78]. Fig. 11c–d shows the fluorescent images of the perovskite film before and after pyridine treatment, where darker regions in the image have greater non-radiative loss [78]. It clearly showed that Lewis bases could passivate perovskite film to reduce the non-radiative recombination.

Previous studies revealed that PbI_2 was a commonly observed by-product in perovskite films due to either incomplete reaction or thermal induced decomposition. Therefore, understanding the function of PbI_2 is greatly desired for enhancing OTP device performance. Supasai et al. reported the existence of PbI_2 in 140 °C annealed perovskite films. Surface photovoltage spectroscopy (SPV) study was carried on the decomposed perovskite films, which revealed that the presence of PbI_2 could reduce the SPV signals that are related to defect states [97]. Yang et al. studied the perovskite solar cells with PbI_2 passivation layer. It was found that the suitable amount of PbI_2 presenting in perovskite grain boundaries was closely correlated to device efficiency increase [98]. It was believed PbI_2 with a larger bandgap than perovskite enables a favored energy band alignment which prevents carriers from being trapped by the perovskite surface defects. Zhao et al. provided another new evidence for the PbI_2 passivation by conducting transient absorption spectroscopy study [99]. The perovskite films with PbI_2 layer showed much slower charge trapping rates which also indicate the passivation effect of PbI_2 in perovskite [99].

4. Film fabrication and film morphology

The efficiency of perovskite solar cell is highly dependent on the film morphology. The remarkable increase of the performance of perovskite solar cells during the last few years benefited from the morphology control of the perovskite films. In this section, both the fabrication process and post-treatment dependent morphology of OTP films are reviewed.

4.1. Film fabrication process dependent morphology

The OTP materials are soluble in polar solvent such as DMF, DMSO, and GBL. Besides, PbI_2 and MAI can also be thermally evaporated in vacuum, and MAI can vaporize in atmosphere pressure when heated at over 150 °C. Therefore, perovskite films can be fabricated by either solution or vapor deposition techniques, or a combination of them, enabling versatile film formation techniques and convenient control of film qualities such

as thickness, composition, grain size, etc. In addition, the perovskite films can be deposited on different substrates and scaled up for industrial scale production. The fabrication methods of perovskite film reported up to now generally include one/two-steps solution spin coating [21,100–102,4,103,22,25,104,105,1], vapor phase assisted deposition [106–108,2], doctor-blade/slot die coating [109–112], spraying coating [113,114], etc.

4.1.1. One-step approach

One-step spin coating is commonly used for perovskite film preparation during the initial development of perovskite solar cells, especially for mesoporous structured perovskite solar cells. Typically, PbI_2 and MAI with 1:1 molar ratio were pre-mixed in the precursor solution and then spin coated onto the substrate, which was then annealed for minutes to hours to obtain the perovskite polycrystalline films. We noticed that, in fabricating planar structure devices, PbI_2 and MAI have different affinity to substrate, therefore though the molar ratio of PbI_2 to MAI is 1:1 in the precursor solution, the molar ratio on the spun film might not be 1:1, resulting in highly *n*-doped perovskite films [22]. We also found that more MAI in the precursor solution could induce the formation of more continuous films. This can be explained that more MAI in the precursor also helps slow down the perovskite crystallization process, similar to the function of HI and DMSO. The best molar ratio in the precursor solution was found to be 0.6 (PbI_2:MAI) when spin coating $MAPbI_3$ on PEDOT:PSS [22]. Although more MAI in the precursor solution could further make the film even smoother, the unreacted MAI could degrade the electronic properties of the $MAPbI_3$ films.

One-step spin coating generally has two disadvantages in terms of film morphology: small grain size and limited coverage [2,7,16,115,116]. The small grain size results from the quick crystallization between the two precursors during the film drying process. Besides, it has been frequently reported that perovskite films formed by one-step spin coating have incomplete film coverage, which imposed a big challenge especially in fabricating of planar heterojunction devices. The planar heterojunction devices has advantages over mesoporous structure device in that they can be processed from low temperature and fabricated on flexible substrate, but they can be easily shorted in the presence of pin-holes, despite that the presence of charge transport layer can partially fill the pin-holes and alleviate the leakage problem. The initial study failed to produce continuous pin-hole free film by changing the perovskite layer thickness and/or annealing temperature, either on PEDOT:PSS or compact TiO_2 substrate, as shown in Fig. 12, because the very quick crystallization of the hybrid perovskite right after spin coating generally causes very rough and non-continuous film by extracting solid content from neighboring area [100,101]. Nevertheless, there were encouraging progresses that continuous films could be formed by controlling of film drying

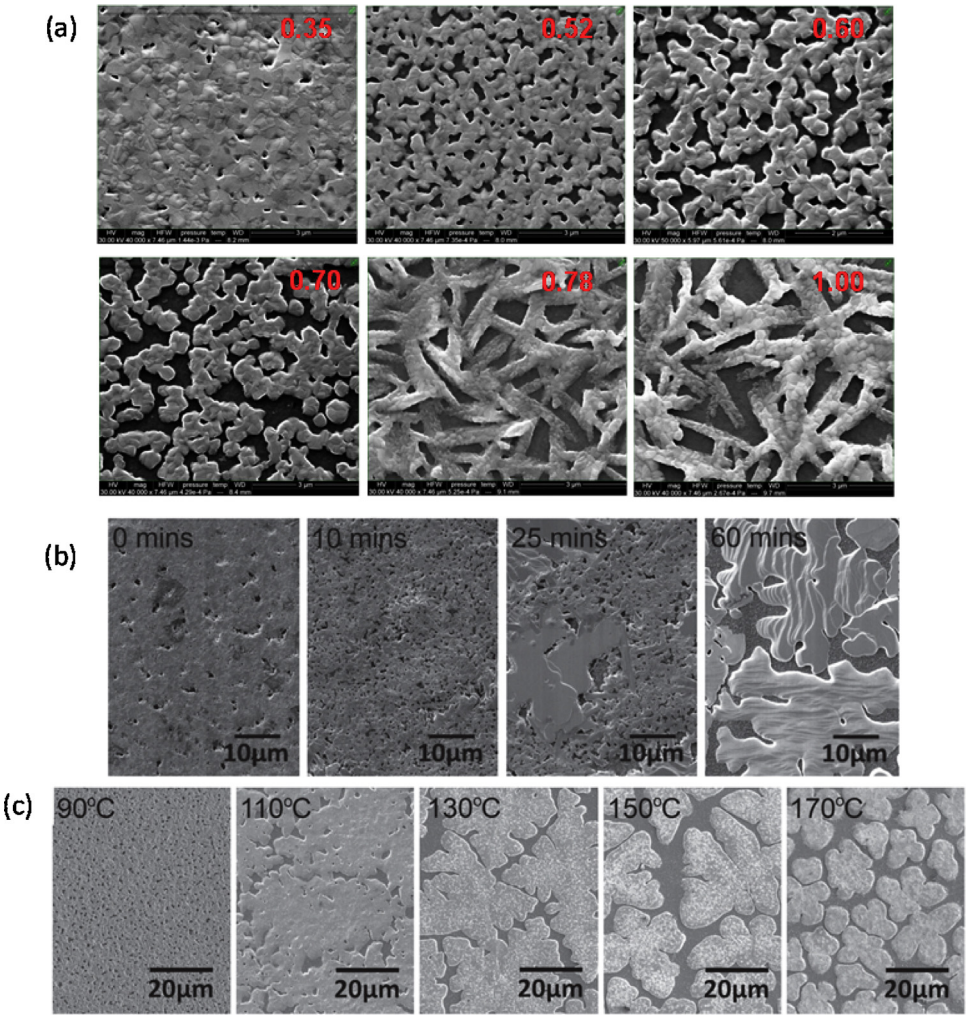

Fig. 12. (a) Top view SEM images with various PbI_2 to MAI molar ratio on top of PEDOT:PSS substrate. (b) SEM images for perovskite film prepared by one-step spin coating on TiO_2 substrate at different annealing duration at 100 °C (b) and different annealing temperature (c).

and/or crystal growth dynamics. Those methods, including solvent engineering, blending additives, changing precursor material and substrates, will be described as below.

4.1.2. Methods to control the morphology of one-step spin coating

4.1.2.1. Solvent engineering. As mentioned above, the one-step deposition method, although simple, is found to be very difficult to deposit a continuous, leakage-free perovskite film with thickness comparable to the charge diffusion length [2,7,16,115,116]. Solvent engineering is one of the most effective methods to form continuous and compact perovskite films using one-step method [117,118]. Xiao et al. developed a fast deposition crystallization (FDC) method using chlorobenzene (CB) to induce crystallization during the spin coating process [117]. As shown in Fig. 13a, the FDC approach involves the spin coating of a DMF solution of $CH_3NH_3PbI_3$ on a substrate, followed by dropping another bad solvent, such as CB and toluene, to induce crystallization. The bad solvent rapidly reduce the solubility of $CH_3NH_3PbI_3$ in the mixed solvent and thus promote fast nucleation and crystallization [117]. The time interval between dropping of the process solution (DMF) and the second bad solvent is critical to get the optimized film morphology. The spinning of processing solvent DMF can be divided into three stages: fast precursor removing, evaporation of the residue solvent, and film drying/heterogeneous crystallization. The time duration of each stage might be different for different processing solvent due to their different volatilities. The best dropping time for the bad solvent was reported to be at the second stage. Too early or too late dropping of CB cannot result in uniform and compact perovskite films [117]. As shown in Fig. 13b–c, the perovskite films prepared from the FDC approach were very uniform and continuous. One requirement for the second solvent is that it must be a bad solvent for both PbI_2 and MAI so that it cannot wash away any precursors. Methanol and ethanol which can dissolve the MAI can result in yellow PbI_2 film since the MAI can be washed off. Other solvents like THF, acetonitrile, and benzonitrile which can dissolve the $CH_3NH_3PbI_3$ will wash away both PbI_2 and MAI.

Later, Jeon et al. used mixed solvents of GBL and DMSO as processing solvent followed by toluene drop-casting [118]. The difference between using GBL and GBL:DMSO as processing solvent is that a dark brown perovskite film was formed immediately after the dropping of toluene solvent, while a transparent CH_3NH_3I–PbI_2–DMSO intermediate phase was formed first after the dropping of toluene using the GBL:DMSO blend solution. The intermediate phase was confirmed by both X-ray diffraction (XRD) and Fourier transform infrared spectroscopy (FTIR) measurement. An extremely uniform and compact perovskite layers can be formed after thermal annealing the intermediate phase film at 100 °C for 10 min, as illustrated in Fig. 13. A certified power-conversion efficiency of 16.2% was reached by using this method [118].

4.1.2.2. Additives. Solution additives are first used in organic solar cells to improve the efficiency [119–121]. They have been found to play an important role to control the morphology of organic thin films such as forming fine polymer:fullerene domains to facilitate the exciton dissociation, vertical phase separation, and crystallization of the organic film [119–121].

Liang et al. first used the 1,8-diiodooctane (DIO) as solution additive to fabricate perovskite films using one-step deposition method and demonstrated that the crystallization rate of perovskite can be controlled [109,110]. The alkyl halide additives might play multiple roles in controlling the perovskite nucleation and grain growth [122,123]. First, the bidentate halogenated additive is expected to chelate with Pb^{+2} during the crystal growth, as shown in the schematics of Fig. 14a. The halide atoms in the additives might participate in the formation process of the perovskite via the extra X ions (X = I, Br, Cl) from the dissociated C–X bond, which is evidenced by the improved solubility of $PbCl_2$

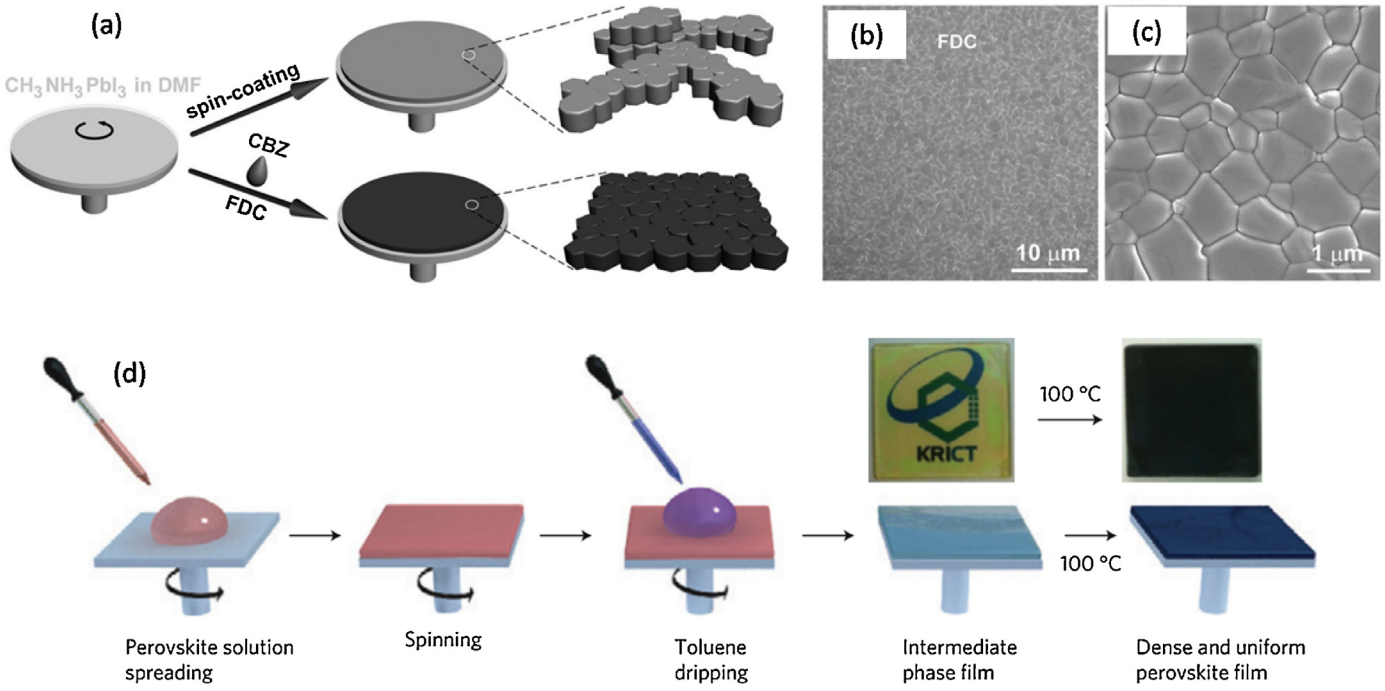

Fig. 13. (a) Schematic illustrations of the FDC process and conventional spin coating process for fabricating perovskite films. Conventional spin coating (top) results in a shiny gray film composed of non-uniform large crystals as a result of slow crystallization. In the FDC process (bottom), a second solvent (e.g., chlorobenzene) introduced on top of the wet film during the spin coating process induces fast crystallization of uniformly sized perovskite grains. (b–c) Low- and high-magnification SEM images of the surface of a $CH_3NH_3PbI_3$ film prepared by FDC with the addition of chlorobenzene [117]. (d) Schematics of the solvent engineering process and photo-images of the intermediate phase film and dense perovskite film [118].

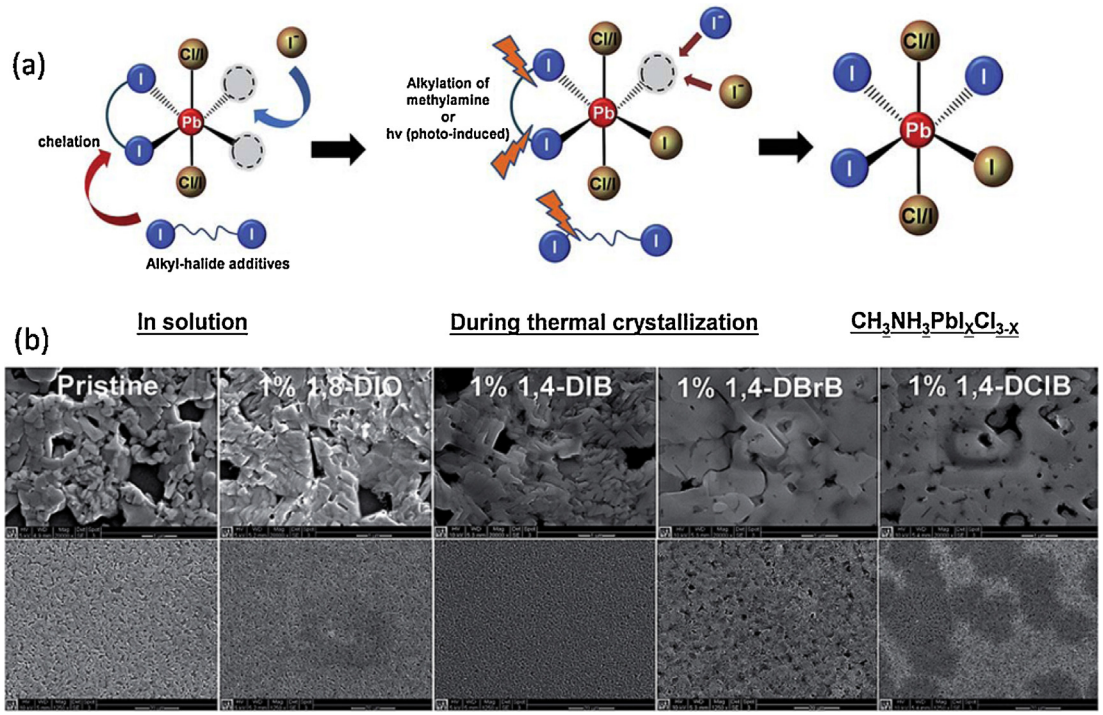

Fig. 14. (a) Illustration of the roles of alkyl-halide additives during perovskite crystallization as revealed by this work. (b) SEM images of the solution-processed perovskite thin films with studied alkyl-halide additives. The scale bar for upper and lower SEM images is 1 and 20 μm, respectively [109].

in the presence of DIO. Second, the additive might be able to modify the interfacial energy between PEDOT:PSS and $CH_3NH_3PbI_{3-x}Cl_x$ and make it more favorable for the crystal growth. Therefore, the perovskite grains preferred to grow at the interface. The perovskite films processed with 1 wt% DIO additive is smoother and more continuous than the controlled film without additive. The SEM images of the perovskite film with different kinds of alkyl halide additives are shown in Fig. 14b.

The HI acid was also found to be a good additive for the perovskite film formation [39,124,125]. Eperon et al. first added small amount of HI (6% v/v) in the DMF solution of stoichiometric FAI:PbI_2 1:1 precursors to fabricate the $FAPbI_3$ perovskite films [39]. The controlled $FAPbI_3$ perovskite films without HI additive are not continuous with many pin-holes, while the films prepared with HI additive is extremely compact and uniform. It was proposed that the addition of HI acid can increase the solubility of PbI_2 in the DMF solution, thus can slow down the crystallization of the film during the spin coating process in one-step deposition method. Therefore a smoother and continuous film can be formed.

Kim et al. used a mixed solvent of GBL:DMF(97:3 volume ratio) for the 1:1 molar ratio of PbI_2 and MAI using one-step spin coating method, where the DMF served as additive [126]. It was found that the mixed solvent can result in much smoother and more continuous films than either GBL or DMF themselves. However, the reason has not been well understood yet [126]. Later, Jeon et al. used N-cyclohexyl-2-pyrrolidone (CHP) as additive (5% volume ratio) in the processing solvent DMF. Highly smooth and continuous films can be obtained by using one-step spin coating method with 1:1 molar ratio of PbI_2 and MAI precursor solution [127]. A guideline was proposed for the solvent additive [127]: (a) Low vapor pressure than the processing solvent like DMF to slow down the solvent evaporation. (b) Good solubility for both PbI_2 and MAI to ensure the formation of stoichiometric $CH_3NH_3PbI_3$ films. (c) High miscibility with the processing solvent.

In addition to the solvent additives, some polymers are also reported to work as additives in the precursor solution to modify the perovskite film morphology [128]. Chang et al. reported that by adding small amount of poly(ethylene glycol), the crystallization of perovskite can be retarded [128]. The perovskite film with 1 wt% of poly(ethylene glycol) can result in much smoother perovskite film with less pin-holes by using the one-step spin coating process. However, it should be noted that, different from solvent additives, the insulating polymer additives remains in the film after the thermal annealing process, too much additives dramatically increase the resistance of the device [128].

4.1.2.3. Precursor materials. The precursor materials also play an important role in the formation of the perovskite films in the one-step spin coating method as they will affect the crystallization rate of the perovskite materials. Up to now the PbI_2 is the most widely used lead source to fabricate the perovskite for both one-step and two-step deposition method. Recently, Zhang et al. and Wang et al. found some other lead sources such as $PbCl_2$ or $PbAc_2$ and $HPbI_3$ can result in different film morphology and crystallinity due to the different film crystallization speed in the one-step deposition method [124,129].

Wang et al. developed a new lead source $HPbI_3$ to fabricate the FA based solar cells. $HPbI_3$ shows even higher solubility in DMF than PbI_2. High crystalline $FAPbI_3$ film can be formed with strong (1 1 0) preferred orientation and better thermal stability by using one-step spin coating of $HPbI_3$ and FAI blend precursor solution (1:1 molar ratio). The $HPbI_3$ precursor can be formed by reacting PbI_2 with HI, the thermal gravimetric analyzer (TGA) results indicated the molar ratio of PbI_2 to HI in the $HPbI_3$ is around 1:1.1. It should be noted that the $HPbI_3$ has similar XRD pattern with PbI_2, but the peak corresponding to the (0 0 1) plane shifted to a lower angle, which indicates that the intercalation of H^+ ions into the PbI_2 lattice, as shown in Fig. 15a. Compared with the PbI_2 lead source, the $HPbI_3$ enable a slow crystallization process due to the exchange of H^+ and FA^+ ions in the PbI_6 octahedral framework which might be hindered by the hydrogen bonds between the H^+ ions and the Pb–I octahedrons. The slow crystallization process was claimed to result in better perovskite film morphology. However, there is another work by Zhang et al. reported that a fast crystallization

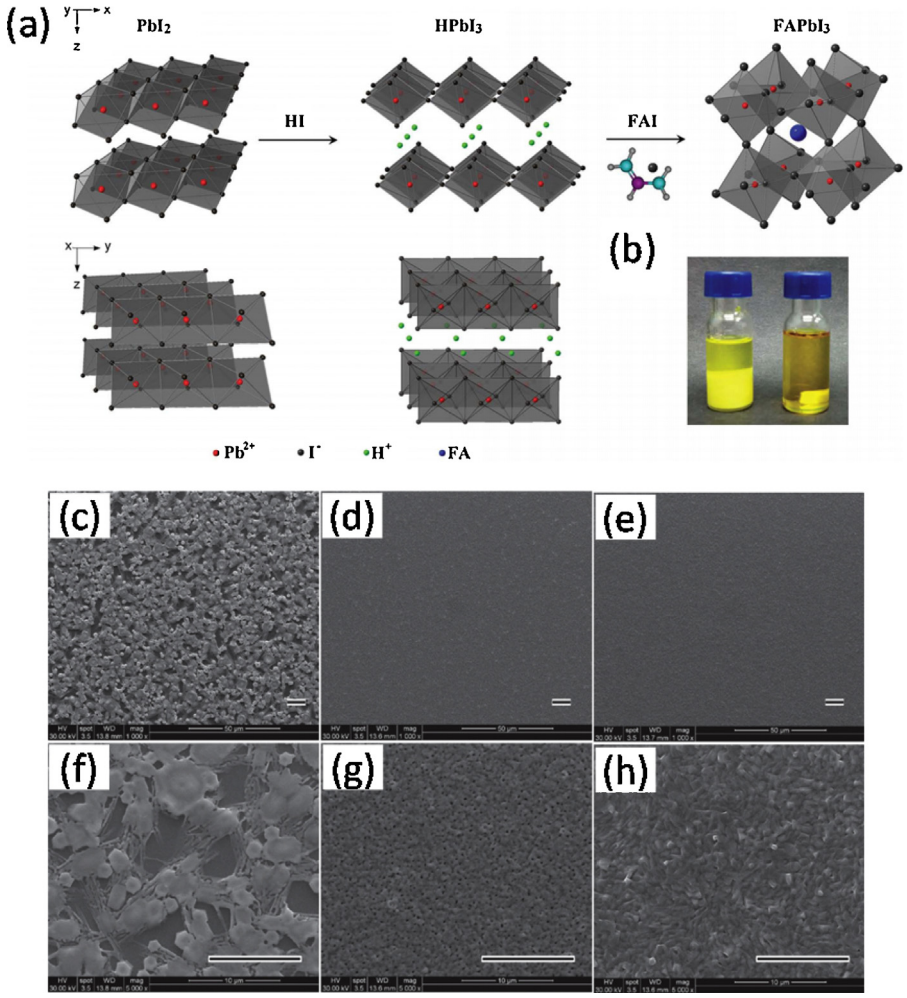

Fig. 15. (a) Schematic illustration of the configurations of PbI_2, $HPbI_3$, and $FAPbI_3$. (b) Solubility comparison of PbI_2 (left) and $HPbI_3$ (right) in DMF. Both solutions have a concentration of 2.0 M and have been stirred for 24 h. (c–h) SEM images of $FAPbI_3$ fabricated from (c,f) FAI/PbI_2, (d,g) FAI/PbI_2 with 5% HI, (e,h) FAI/$HPbI_3$ on compacted TiO_2 substrates. The scale bars are 10 μm [100].

process is preferred for the one-step deposition to get a uniform and continuous perovskite film [129]. Therefore, there might be some other factors that affecting the formation process of the perovskite film and its morphology. The $FAPbI_3$ perovskite films prepared using $HPbI_3$ and FAI precursor solution are more continuous than the films prepared by the PbI_2:MAI precursor solution and PbI_2:MAI precursor solution with HI additive as shown in Fig. 15. Compared with the PbI_2 and FAI precursor solution with HI additive, it eliminates the water in the precursor solution.

Zhang et al. reported that the anion in the lead source (PbI_2, $PbCl_2$ and $PbAc_2$) plays an important role in the perovskite crystal growth kinetics and film morphology [129]. A continuous and compact film, which is even smoother than the vapor deposited films, can be obtained by simple one-step solution process using the $PbAc_2$ lead source, as shown in Fig. 16. It should be noted that a precursor ratio of MAI to lead source of 3:1 was used to fabricate the film which can result in better film morphology. The precursor ratio effect on the film morphology will be discussed later. The in-situ wide-angle X-ray scattering (WAXS) was used to detect the evolution of the perovskite film formation process using different lead source. It was found that different lead source has different perovskite crystal formation speed. The formation speed is fastest from the $PbAc_2$ lead source, and then followed by $PbCl_2$ lead source and PbI_2 source. The underlying reason was well explained by analyzing the perovskite film formation processes. The reaction of the precursors to form perovskite material can be described by the following equation:

$$PbX_2 + 3CH_3NH_3I = CH_3NH_3PbI_3 + 2CH_3NH_3X(X = Cl; I; Ac)$$

where, CH_3NH_3X is the by-product of the reaction. Since excess MAI was used in the blend precursor solution, the volatility of the by-product is critical to the crystallization speed of the perovskite. The volatility of MAAc is much higher than the MAI and MACl, which is confirmed by the TGA. Therefore, the crystallization speed of using $PbAc_2$ lead source is much faster and the formed perovskite film is much smoother. It should be noted that, due to the fast crystallization process caused by using $PbAc_2$ lead source, the grain size of perovskite film (135 ± 45 nm) is much smaller than those prepared from the PbI_2 lead source (305 ± 65 nm) and $PbCl_2$ lead source (>500 nm). Nevertheless, in their study, the device performance from $PbAc_2$ lead source reached $14.0 \pm 0.7\%$ which is much higher than that of devices from $PbCl_2$ lead source ($12.0 \pm 1.0\%$) and PbI_2 lead source ($9.3 \pm 0.8\%$). Moore et al. used the $Pb(NO_3)_2$ as lead source, and the by-product of $MANO_3$ is also even more volatile, therefore, the perovskite film can be formed at 45 °C for 20 min [130]. However, due to the too low temperature annealing, some NO_3 ion residues was detected by FTIR, which could be removed by dipping the perovskite films into IPA solvent or thermal annealing.

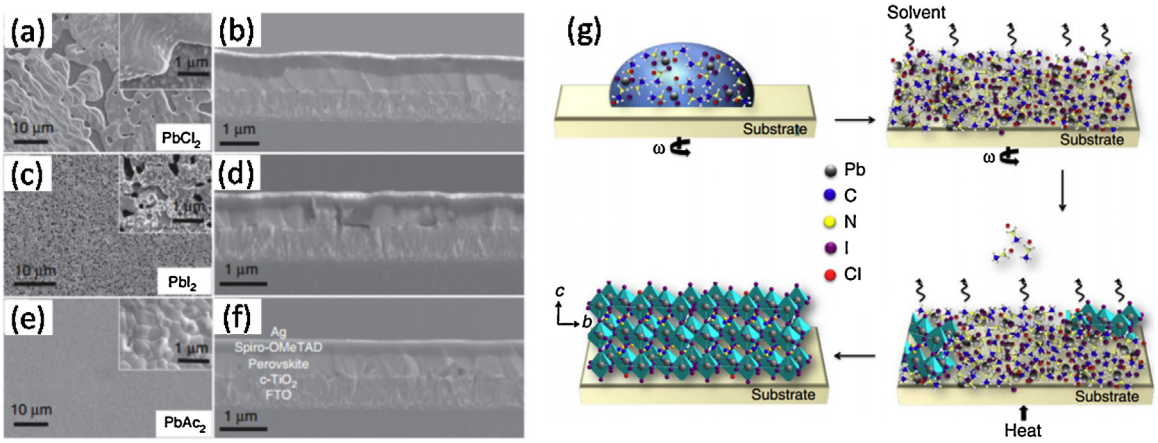

Fig. 16. SEM images of perovskite films. The films were deposited on FTO/c-TiO_2 substrates from the three different lead sources $PbCl_2$ (a), PbI_2 (c) and $PbAc_2$ (e); insets show images with higher resolution; cross-sections of full devices with the perovskite derived from $PbCl_2$ (b), PbI_2 (d) and $PbAc_2$ (f) routes. (g) Illustration of the stages in the fabrication of $CH_3NH_3PbI_{3-x}Cl_x$ thin films. During the solution coating process, solvent evaporation occurs but the excess organic component remains within the film, the removal of which by following thermal annealing leads to the fully crystallized perovskite thin film [129].

The organic component also affects the perovskite film morphology and crystallinity. The most popular approach is blending MACl in the precursor solution [4,12], which should has similar effect of using $PbCl_2$ as lead source for the one-step spin coating method.

Another issue needed to be pay attention to in using different lead source is the Cl, Ac or other spectator content left in the formed perovskite films. The Cl content in the $MAbI_xCl_{3-x}$ mixed halide perovskite film and its effect on the device performance are still under debate [131]. The ion radius of Ac (0.162 nm) is smaller than Cl (0.184 nm), so it is less likely than Cl to be incorporated into the lattice of $CH_3NH_3PbI_3$ [129]. In addition, the XRD also shown almost the same pattern for the perovskite film fabricate from $PbAc_2$ and PbI_2 precursors, which indicates that the Ac ions was not incorporated into the lattice of $CH_3NH_3PbI_3$.

4.1.2.4. Substrate effect. The substrate also plays an important role in controlling the morphology, crystallinity, grain size and orientation of the perovskite films using one-step deposition approach. In this part, the effect of wettability, roughness of the substrate on the perovskite film formation and morphology will be discussed.

Generally, good wettability of the substrate is preferred to obtain uniform crystalline perovskite films [132]. Wetting surfaces have smaller Gibbs free energy for nucleation (ΔG_{het}), which is determined by the contacting angle: $\Delta G_{het} = \Delta G_{hom}(2 + \cos\theta)(1 - \cos\theta)^2/4$, where ΔG_{hom} is homogeneous nucleation energy. Therefore, the smaller the contact angle, the smaller nucleation energy for the heterogeneous nucleation. For instance, a small θ of 10° reduces ΔG_{het} to be $1.7 \times 10^{-4} \cdot \Delta G_{hom}$, which dramatically promotes the nucleation and forms very dense nuclei of perovskite on the wetting surface.

Zuo et al. used a self-assembled monolayer of 3-aminopropanioc acid (C3-SAM) to increase the wettability of the sol–gel prepared zinc oxide (ZnO) [132]. The authors used the one-step spin coating method with equal molar ratio of PbI_2 and MAI to fabricate the perovskite films. For the control device without C3-SAM, the perovskite film showed nanorod-like grains with 200–300 nm diameter and 4 μm length. While after the C3-SAM modification, the perovskite films showed more plate-like grains with the lateral dimension increased up to several micrometers. In addition, the C3-SAM can also increase the work function of the ZnO layer due to its aligned dipoles. As a result, the average efficiency was increased from around 9.81% to 14.25% [132]. Ogomi et al. deposited a monolayer of $HOCO\text{-}R\text{-}NH_3^+I^-$ on top of mesoporous TiO_2 and Al_2O_3 substrate to modify the morphology of the perovskite [133]. The wettability of the TiO_2 substrates was claimed to be increased after the $HOCO\text{-}R\text{-}NH_3^+I^-$ modification, and the modified TiO_2 or Al_2O_3 substrate can be fully covered by perovskite film.

The roughness of the substrate can also impact the morphology of the perovskite films. For the perovskite films deposited on FTO/PEDOT:PSS and ITO/PEDOT:PSS substrate using one-step spin coating method, the coverage of perovskite on the former one is more homogeneous with better coverage than the films deposited on the later one, which might be benefited from the rougher surface of FTO (100 nm) compared with the ITO surface (around 5 nm) [16]. It should be noted that in the Eperon's work [101], where the perovskite film was deposited on the mesoporous alumina covered compact TiO_2/FTO substrate, the surface coverage of the perovskite film was found to depend on the thickness of the alumina layer. This result might be consistent with the roughness dependent coverage, because the thicker the mesoporous layer is, the rougher the substrate is. The thickness of the substrate might also affect the perovskite film morphology. For the perovskite films deposited on compact TiO_2, the coverage of the perovskite film is found to depend on the thickness of TiO_2, with the TiO_2 thickness increase, the coverage of the perovskite film increases [101]. However, the underlying reason is not clear yet.

The temperature of the substrate is critical in controlling the film morphology. Mohite et al. recently reported a hot casting method by pre-heating the substrate to 130–190 °C right before spin coating combining hot precursor solution to obtain pin-hole free perovskite films, whose morphology are shown in Fig. 17

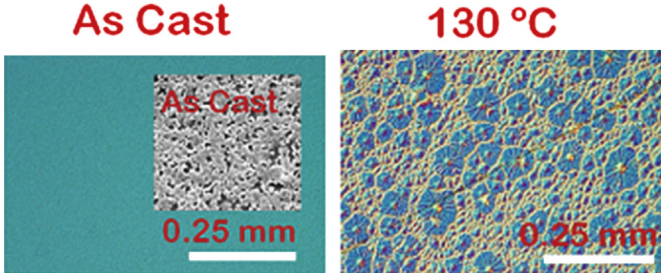

Fig. 17. Optical micrographs illustrating pervoskite formation prepared from standard one-step spin coating (left) and "hot casting" (right) methods, respectively.

[103]. The authors claim that such polygonal domains in sub-millimeter scale were single crystal grains, however more recent work shows that each domain is not single crystalline, but composed of finer perovskite crystals on the micrometer scale as observed by higher magnification SEM. In fact, quick drying of the solution at very high temperature forced the solid to stay where they were deposited, thus smaller crystals should be anticipated rather than bigger ones, similar to the FDC mechanism, which also relies on quick removal of solvent. Nevertheless, it is still a very good method to obtain pin-hole free perovskite film in one-step spin coating. It should be noted that these polygon domains resemble the typical Rayleigh–Bénard convection pattern, which occurs when a thin film of solution is heated from bottom. The improved perovskite film coverage is achieved through the long range material transporting by such strong convection.

4.1.3. Two-step approach

In order to solve the problems of one-step spin coating method, two-step spin coating was reported in the early 2014, which yields continuous pin-hole free perovskite films with high device yield and solar cell performance. Two-step deposition method was first reported by Graztel in formation of $MAPbI_3$ in mesoporous structure solar cells, named as "sequential solution deposition", where the spun PbI_2 film is immersed into MAI isopropanol (IPA) solution to complete the conversion to perovskite, as shown in Fig. 18a. The conversion was reported to be very quick, and no thermal annealing was required in this process. Certified efficiency of 15% was reported in 2013 for the mesoporous structure devices [1].

When we tried to apply this method to planar heterojunction perovskite solar cells, we found this method could not form uniform perovskite film on flat PEDOT:PSS covered ITO substrates. Again, although the non-continuous film is not big issue in mesoporous structure device because of the thick charge transport layer used, it can completely ruin the planar structure devices by shorting the cathode and anode. To address this issue, we modified the two-step deposition method by spin coating both PbI_2 and MAI layers successively on top of PEDOT:PSS substrate at very high spin-rate followed by a thermal annealing process (Fig. 18b) [21].

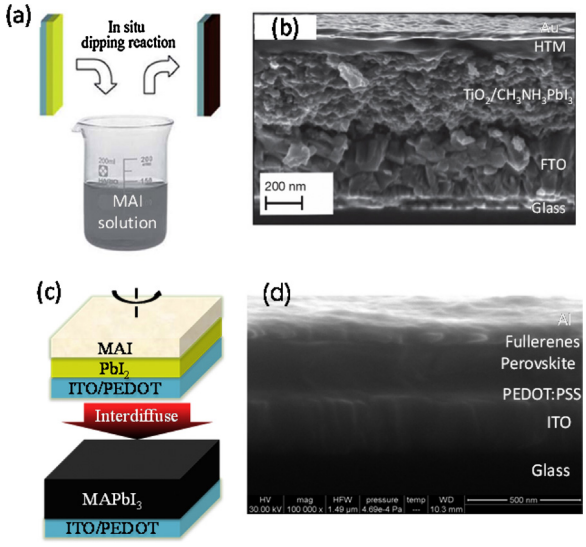

Fig. 18. Schematic illustration of sequential deposition (a) and cross-section SEM image (b) [1] The PbI_2 was first spin coated on top of mesoporous TiO_2 film, followed by dipping into MAI solution. (c–d) Schematic illustration of two-step spin coating (interdiffusion) deposition (c) and cross-section SEM image (d). The PbI_2 was first spin coated on top of a flat substrate (ITO/PEDOT:PSS), then, the MAI are spin coated on top of the compact PbI_2 layer, followed by thermal annealing to drive the interdiffusion and reaction between PbI_2 and MAI layer [21].

PbI_2 was dissolved in DMF and heated to ~90 °C before spin coating due to its limited solubility in DMF. The MAI layer was spin-coated on the top of PbI_2 layer using IPA solution. Since IPA is bad solvent for PbI_2, PbI_2 cannot be washed away by the second layer coating process. The stacked two layers were then subjected to a thermal annealing process, during which the two components interdiffuse into each other to form perovskite after reaction [21]. The concentration of PbI_2 and MAI solutions need to be finely tuned to obtain appropriate stoichiometric ratio in the final perovskite film. The interdiffusion process is generally slow, allowing retarded chemical reaction of MAI and PbI_2 and then slow perovskite nucleation and crystal growth, comparing to one-step spin coating method where chemical reaction happens right after the solvent is spun off the substrate. The perovskite crystallization rate can be conveniently controlled by the annealing temperature, enabling better control of final film property. In addition, controlling the annealing atmosphere can also modify the film quality. We have found that introducing DMF vapor during interdiffusion thermal annealing (solvent annealing) can increase the crystal size. Highly reproducible, pin-hole free, smooth films were obtained on flat substrate, based on which a steady-state efficiency of 15.4% was reported in the early 2014 [21].

4.1.4. Methods to control the morphology of two-step spin coating

4.1.4.1. Substrate effect. As discussed above, a wetting surface is preferred to form uniform and continuous perovskite film. However, the grain sizes of the perovskite films are usually compromised. Generally, the surface tension from the wetting substrates could reduce the grain boundary mobility, which impedes the grain growth. In order to grow larger perovskite grains, a smooth and nonwetting substrate is preferred to prevent the formation of too dense nuclei from heterogeneous nucleation. Bi et al. studied the film morphology of $MAPbI_3$ on wide range of wetting and nonwetting polymer substrates, including polyvinyl alcohol (PVA), PEDOT:PSS, cross-linked N4,N4′-Bis(4-(6-((3-ethyloxetan-3-yl)methoxy)hexyl)phenyl)-N4,N4′-diphenylbiphenyl-4,4′-diamine (c-OTPD), Poly[bis(4-phenyl) (2,4,6-trimethylphenyl)amine] (PTAA), and Poly[N-9′-heptadecanyl-2,7-carbazole-alt-5,5-(4′,7′-di-2-thienyl-2′,1′,3′-benzothiadiazole)] (PCDTBT) [23]. The contacting angles of water on these polymers are 10°, 12°, 79°, 105° and 108° for PVA, PEDOT:PSS, c-OTPD, PTAA and PCDTBT, respectively. Fig. 19b–c show the cross-section and top surface images of the perovskite films deposited on different polymer layers. It is clear that as the wettability of the substrate decreases, the grain size of the perovskite increases. Most of the grains in $MAPbI_3$ films on nonwetting polymers are much larger than the film thickness, with the average grain size/film thickness aspect ratio reaching 2.3, 3.2 and 7.9 for c-OTPD, PTAA and PCDTBT, respectively [23]. In addition, the grain boundaries tend to be in the out of plane direction to minimize the total grain boundary area.

The large average grain size/thickness aspect ratio of the perovskite film grown on nonwetting HTLs dramatically reduces the trap density and boosts the PCE of OTP planar heterojunction solar cells. The device's J_{SC} increased from 18.6 to 21.2 mA/cm^2 and V_{OC} increased significantly from 0.92 to 1.09 V, when the device's HTL was changed from PEDOT:PSS to c-OTPD. Over 35% of the devices have PCE higher than 16.0%, and >80% devices have PCE larger than 15.0% with the highest efficiency reached 18.3% [23].

4.1.4.2. Precursor materials. As expected from the conversion of CH_3NH_3I–PbI_2–DMSO intermediate phase into $MAPbI_3$ phase in the one-step deposition method, most recently, Yang et al. reported an intramolecular exchange process (IEP) to fabricate high-efficiency $FAPbI_3$ based solar cells using two-step spin coating approach. In the IEP method, the PbI_2–(DMSO) phase

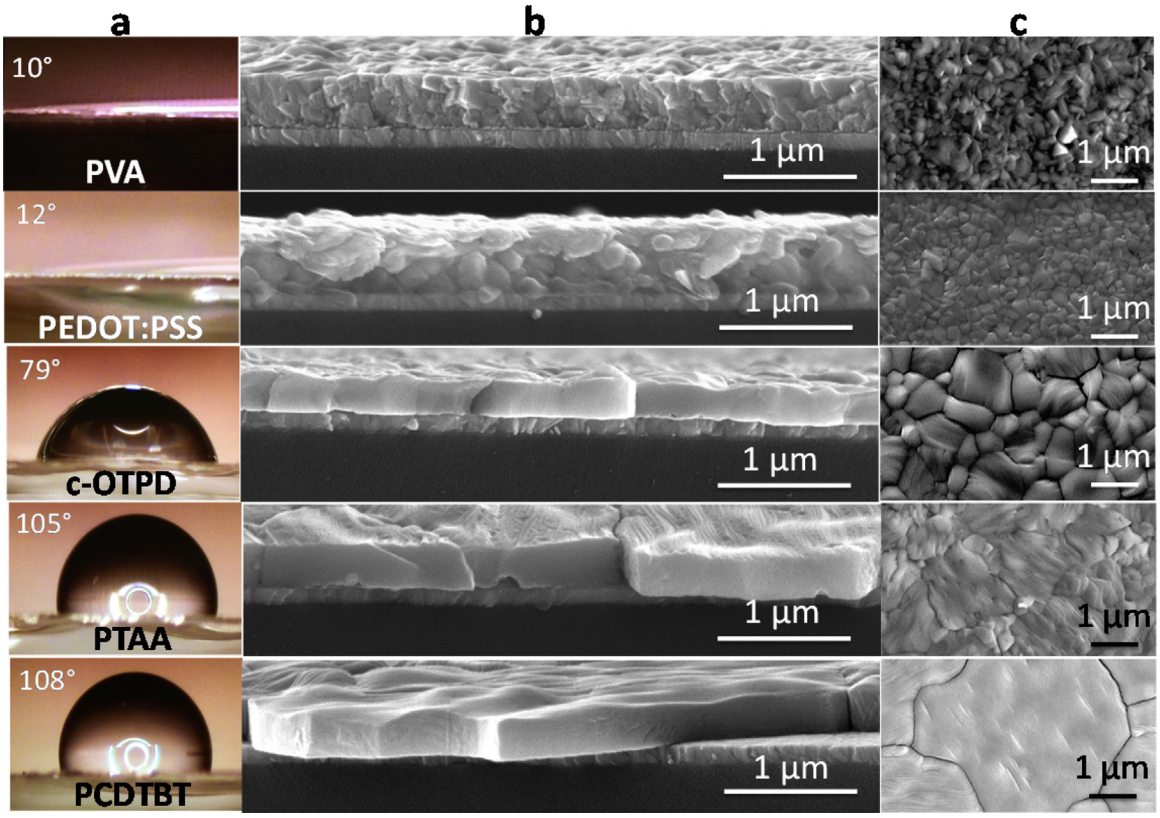

Fig. 19. The contact angle (a), cross-section SEM (b), top-view SEM (c), and (g) XRD diffraction patterns of the 360 nm $MAPbI_3$ grown on PVA, PEDOT:PSS, c-OTPD, PTAA and PCDTBT covered ITO substrates [23].

was first formed by vacuum annealing of PbI_2–$(DMSO)_2$ complex at 60 °C, where the PbI_2–$(DMSO)_2$ complex was prepared by pouring bad solvent toluene into PbI_2 solution dissolved in DMSO. The PbI_2–(DMSO) phase is relatively stable and can be dissolved in DMF solution for the spin coating of high quality PbI_2–(DMSO) film. After spin coating of FAI on top of the PbI_2–(DMSO) film, the DMSO molecules can be easily replaced by FAI molecules because they have similar molecule size and FAI has higher affinity toward PbI_2 than DMSO. The schematics of the IEP are shown in Fig. 20b. The IEP can form high crystalline, uniform and compact $FAPbI_3$ films

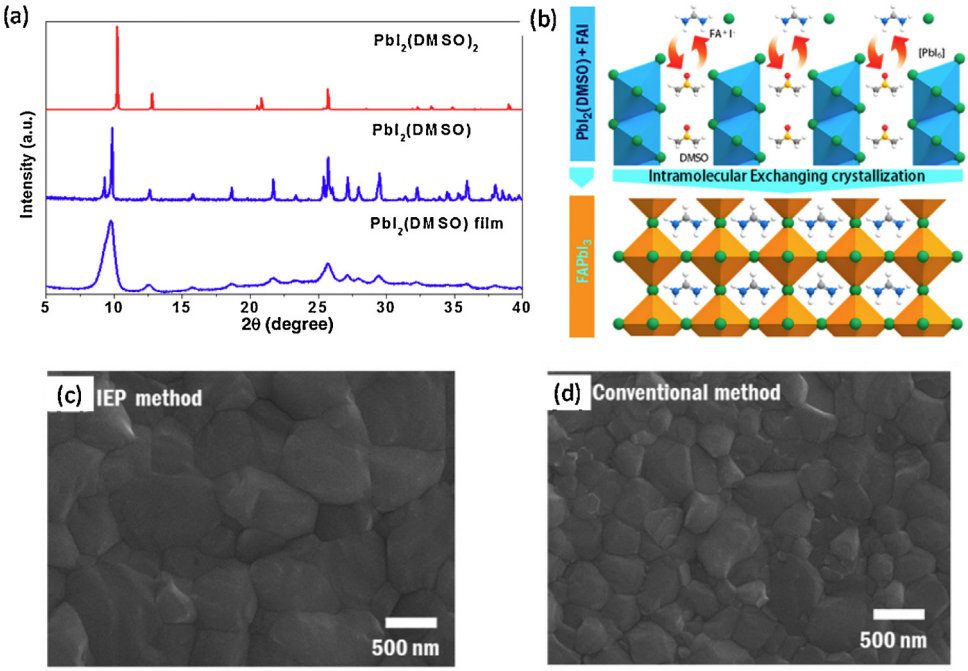

Fig. 20. (a) XRD patterns of as-prepared $PbI_2(DMSO)_2$ powders, vacuum-annealed PbI_2(DMSO) powders, and as-deposited film on fused quartz substrate using PbI_2(DMSO) complex solution. (b) Schematics of $FAPbI_3$ perovskite crystallization. (c–d) The comparison of SEM surface images of $FAPbI_3$-based layer formed on mp-TiO_2 by IEP (c) and conventional method (d) [24].

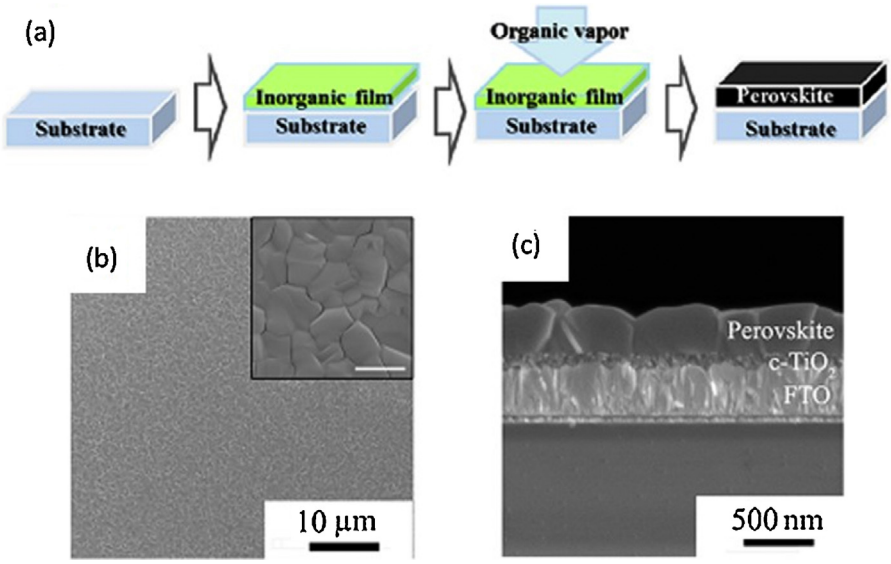

Fig. 21. (a) Schematic illustration and (b, c) SEM images for vapor-assisted solution process (VASP) deposition of perovskite film.

with preferred orientation along the [103] axis compared with the conventional two-step sequential depositing method, as shown in Fig. 20c–d. The highest certified efficiency reached 20.1% using a structure of (FTO)–glass/compact TiO_2/mesoporous–TiO_2/perovskite/PTAA/Au.

4.1.5. Vapor-assisted film deposition approach

Vapor-assisted film deposition is another commonly used method for perovskite film formation. Snaith et al. pioneered this method and obtained compact, flat perovskite film by co-evaporation of $PbCl_2$ and MAI and achieved 15% device efficiency in 2013 [2]. The advantage of thermal evaporation method is that the perovskite film can deposit on various substrate with varied wettability and morphology. However, high vacuum thermal evaporation suffers from higher costs and much lower throughput rate than solution deposition method. In this regard, Yang et al. developed vapor-assisted solution process (VASP) deposition method in 2013, where the solution-processed PbI_2 layer was subjected to MAI vapor treatment, as shown in Fig. 21. The MAI vapor was generated by heating MAI powder in atmospheric pressure at ~150 °C in a closed container [106,107]. Pin-hole free perovskite layer with large grain size up to 1 μm was obtained, based on which a device PCE of 12% was realized [106]. It should be noted that the film morphology is very much like that obtained by two-step interdiffusion method. In fact, the two methods is similar in that MAI molecule, either from spun film or from atmosphere, interdiffuse into PbI_2 film to complete the reaction to perovskite. The large grain size obtained in the vapor-assisted solution deposition method can be explained by the relatively slow interdiffusion and reaction between MAI vapor and PbI_2 film comparing to one-step solution spin coating method. More recently, it was reported that by reducing the MAI vaporization pressure to ~0.3 Torr the device efficiency was improved to 16.8% [108]. The author suggested that it is because lowered pressure reduces MAI vaporization temperature to 120 °C, comparing to 150 °C used at atmosphere pressure. Therefore, with a broader annealing temperature range, one can better optimize the perovskite film and obtain improved device efficiency.

4.1.6. Scalable film coating approach

For mass production of perovskite solar cells, scalable film formation process is desired, in addition to spin coating and vapor deposition methods. We and several other groups independently developed the doctor-blade coating of perovskite films from pre-mixed PbI_2/$PbCl_2$ and MAI precursor solution on substrates. Jen et al. reported room temperature doctor-blade coating, by which they demonstrated a PCE of 12.21% [111,112]. Similar results were obtained by Vak et al. who used slot die coating method (a method very close to doctor-blade coating but with continuous supply of precursor solution) to realize fully printable fabrication of perovskite except the electrode, yielding a PCE of 11.96% [110]. However, the films doctor-bladed at ambient temperature always contain a lot of pin-holes which might form during the slow drying of the wet film. We found that by elevating the ITO substrate temperature to ~135 °C during doctor-blading can substantially improve the perovskite film quality, yielding pin-hole free layer with micrometer scale grain size, based on which a high efficiency of 15% is achieved [109], as shown in Fig. 22a–b. Noteworthy, the perovskite film is composed of polygon-like domains in the sub-millimeter scale, which resemble the morphology reported by Mohite et al. where they similarly heated the substrate at 130–190 °C for one-step spin coating [103]. Therefore, it is clear that the substrate temperature plays a critical role in the formation of perovskite film with such polygon domain, irrespective of spin coating or blade coating method. As discussed above, these domains might be due to the strong convection during solution coating process induced by temperature difference between the substrate and top surface of precursor solution, i.e., Rayleigh–Bernard convection.

Another scalable method reported recently is ultrasonic spray coating of perovskite layer from pre-mixed $PbCl_2$/PbI_2 and MAI precursor solution on to substrates. Similar to one-step spin coating and doctor-blade coating, both of which use the same precursor solution component, it is found that heating the substrate can increase the coverage of the spray coated perovskite film on substrate, and then improved device efficiency. Xiao et al. proposed that the better coverage resulted from reduced substrate's surface tension at elevated temperature (Fig. 22d) [134]. However, the coverage in the optimized film is still limited, comparing to one-step spin coating and doctor-blade coating method, suggesting that not only reduced surface tension, but also enhanced convection of solution film, which is absent in the spray coating process, contributes to pin-hole free perovskite film when then substrate is heated from below [23,113,114,135].

It should be noted that, in the one-step doctor-blade coating method, the stabilizer in the HI solution plays a critical role in the

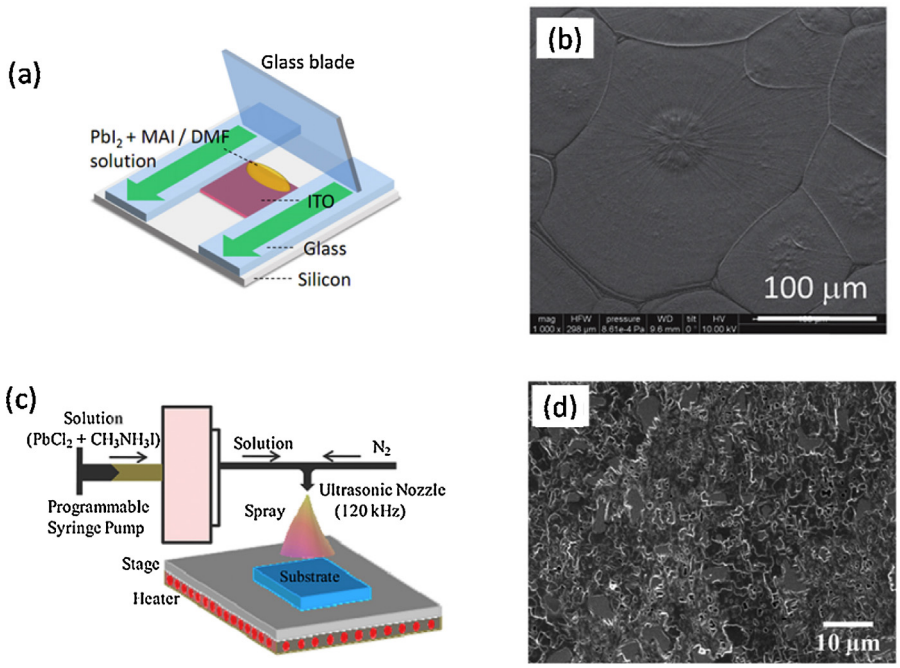

Fig. 22. Schematic illustration (a) and SEM images (b) for doctor-blade coating of perovskite film with a homemade setup [109]. Schematic illustration (c) and SEM images (d) for spray-coating prepared perovskite film [134].

film morphology. Generally, HI and CH_3NH_2 (MA) solutions are the starting materials for MAI synthesis, while HI solution contains ~1.5% H_3PO_2 (Sigma-Aldrich) as a stabilizer to prevent the decomposition of HI [109]. H_3PO_2 can also react with MA to form MAH_2PO_2 which is hard to be completely removed by regular MAI washing process using diethyl ether [109]. It needs recrystallization process to get pure MAI. The stabilizer is found to be detrimental for the doctor-blade coating of the smooth OTP films because it can also react with PbI_2 to form insoluble precipitate $Pb(H_2PO_2)_2$. The insoluble impurity $Pb(H_2PO_2)_2$ might impede the merging of adjacent domains. Fig. 23 show the surface images of the doctor blades perovskite films using unpurified MAI and recrystallized MAI. It is obvious that the domains, containing many grains, of the film using unpurified MAI is smaller than the film using recrystallized MAI, and the gap between domains is larger.

4.2. Morphology control by post treatment

As discussed in Section 4.1.6, the film morphology control during the film fabrication process have shown to be very effective either using one-step or two-step approach. Another way to modify the film morphology and crystallinity is the post treatment. In the past couple of years, there has been several post treatment techniques reported including thermal annealing, solvent annealing, and methylamine-gas treatment etc., which are reviewed in this section.

4.2.1. Thermal annealing

Thermal annealing is the most broadly applied technique to increase the crystallinity of materials, especially thin films, because of its simplicity. It has been utilized to modify the morphology of the perovskite film prepared by both one-step [101] and two-step method [1,21].

Generally, extra amount of organic precursors are used for the one-step approach to optimize the morphology of perovskite films. Thermal annealing are expected to serve for many function, such as (1) assisting the formation of perovskite and enhancing its crystallinity and grain growth, (2) assisting the evaporation of the excess amount of MAI and by-products [129]. Both annealing temperature and duration are critical to get the optimized film

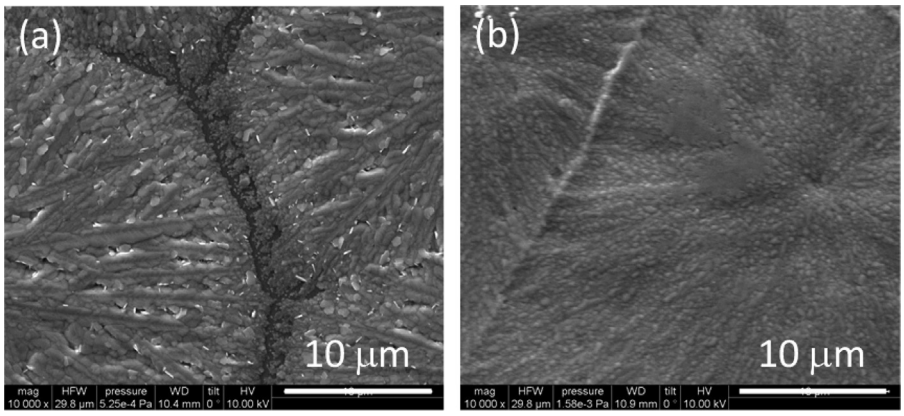

Fig. 23. SEM images $MAPbI_3$ films formed at low temperature of 125 °C using unpurified MAI (a), and purified MAI (b) [109].

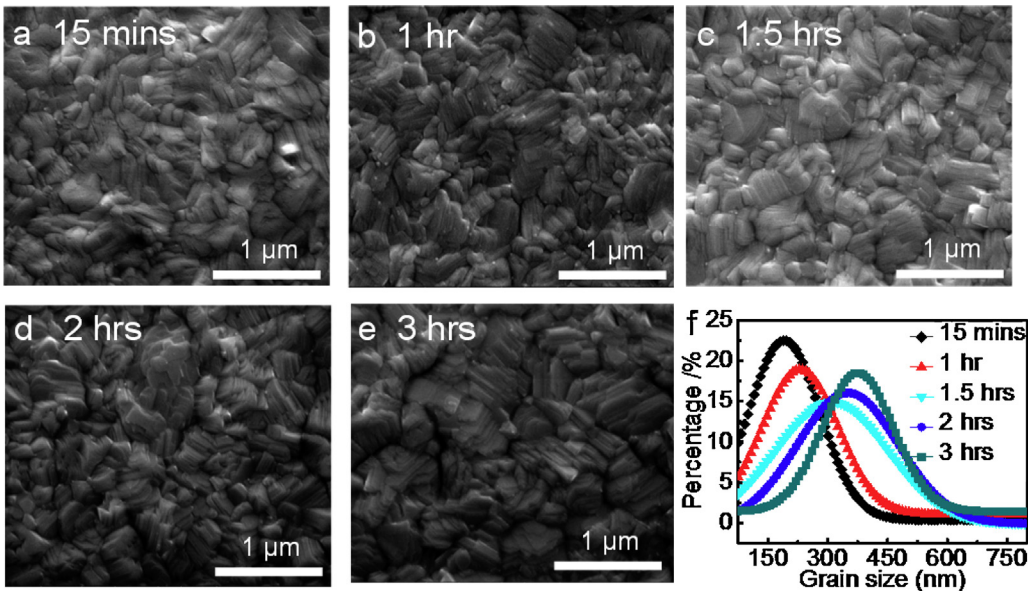

Fig. 24. SEM images of $MAPbI_3$ films with different annealing times: (a) 15 min, (b) 1 h, (c) 1.5 h, (d) 2 h, and (e) 3 h; (f) grain size distribution of the films with varied annealing durations [21].

morphology. For the perovskite films prepared from different lead source, the optimized annealing temperature and duration is different depending on the volatility of the by-product of the reaction between lead source and organic precursor [124,129,130]. For example, the perovskite films can be formed at 100 °C using the lead chloride ($PbCl_2$) and lead acetate ($PbAc_2$) as lead source and MAI as the organic precursor, and it takes around 2.5 min and 43.8 min, respectively, for all the by-product evaporated from the film since MAAc has higher volatility than MACl. However, the perovskite did not form at 100 °C using PbI_2 as the lead source, even after 12 h of annealing. It needs much higher temperature of 150 °C and takes 17.8 min for all the by-products (MAI) evaporated [129]. For the $Pb(NO_3)_2$ lead source, the perovskite film can form even at lower temperature of 45 °C due to the high volatility of the $MANO_3$ by-product [130].

For the one-step deposited perovskite film on compact TiO_2 using 3:1 molar ratio of MAI to $PbCl_2$, Eperon et al. observed that, as annealing temperature or duration increased, the surface coverage reduced, as seen in Fig. 12 [101]. This experiment suggests low temperature annealing is preferred to attain maximum coverage whilst still enable crystallization of the perovskite film [101]. The short circuit current (J_{SC}) of the perovskite solar cell devices showed a linear relationship with the perovskite film coverage from 11 mA/cm^2 with coverage of 56% to 18 mA/cm^2 with coverage of 94%.

In the two-step deposition method, where the perovskite film was formed by interdiffusion of staked layers of PbI_2 and MAI, the thermal annealing is expected to have three functions [21]: (1) driving the interdiffusion of PbI_2 and MAI stacking layers to form the perovskite, (2) increasing the grain size and crystallinity of the formed perovskite films and (3) assisting the evaporation of extra organic precursors. Bi et al. did a comprehensive study of the thermal annealing effect on the morphology and optoelectronic property of the perovskite films [21]. As shown in Fig. 24, the average grain size of perovskite film with thickness of 300 nm increases with thermal annealing duration at 105 °C. The grain size increased gradually from 190 nm with 15 min of annealing to 350 nm with 2 h of annealing. It should be noted that the average grain size of the film after one or two hours of annealing is larger than the film thickness so that the photo generated carriers can be transported in a single grain before collected by the electrode. The two-step spin coating approach has been widely used and a high efficiency of >15% has been obtained by many groups [21,104].

It should be noted that high temperature annealing and/or annealing for long time will lead to the decomposition of the perovskite materials [21,98]. Nevertheless, appropriate releasing of organic species during annealing is good for the device performance, because the PbI_2 phase at the perovskite grain boundaries and relevant interfaces can passivate the perovskite films [98].

4.2.2. Solvent annealing

Complementary to thermal annealing, solvent annealing, where solvent vapor was introduced during the film formation process, was also found to be an effective method to modify the morphology and crystallinity of the perovskite film. Solvent annealing is originally used in solution-processed organic solar cells to improve the crystallinity of the organic thin films [136,137]. We first reported that the solvent annealing could also be used to increase the crystallinity and grain size of OTP materials [31]. Since both PbI_2 and MAI have high solubility in DMF or DMSO, the DMF and DMSO vapor could provide a wet environment so that the precursor ions and molecules could diffuse a longer distance than in all solid-state thermal annealing, which promotes the grain growth and yields a larger grain size. The average grain size of the solvent annealed perovskite films was always comparable or larger than the film thickness, while the grain size of the thermal annealed samples kept at around 250 nm. Therefore, the solvent annealing is superior to the thermal annealing for thick perovskite films. Fig. 25 shows the SEM cross-section images of the perovskite device with thickness of 1 μm after thermal annealing and solvent annealing for 1 h. Due to the increased grain size and crystallinity, the recombination lifetime was prolonged by about four times due to the less defects and grain boundary. The hole mobility of the film measured by Hall effect was increased from 30 to 45 cm^2/V s. The carrier diffusion length of the perovskite film was estimated to be increased from around 250 nm to longer than 1 μm [31]. As a result, the efficiency kept above 14.5% for the devices with thickness changing from 250 nm to 1 μm after solvent annealing. The high tolerance of the efficiency on the film thickness after

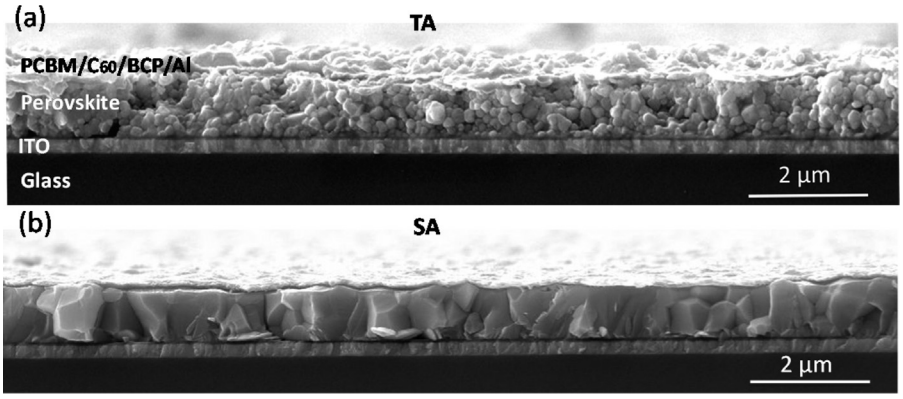

Fig. 25. Cross-sectional SEM images of the thermally annealed (a) and solvent-annealed (b) perovskite films with thickness 1015 nm [31].

solvent annealing is highly preferred for the larger scale manufacturing techniques where the thickness cannot be precisely controlled.

It should also be noted that You et al. found the thermal annealing of perovskite films in a humid environment can also greatly improve the grain size and crystallinity [138]. This report is consistent with the effect of solvent annealing since the water is also a good solvent for the perovskite materials and the water vapor in the humidity air can also help the grain growth and crystallization of perovskite films.

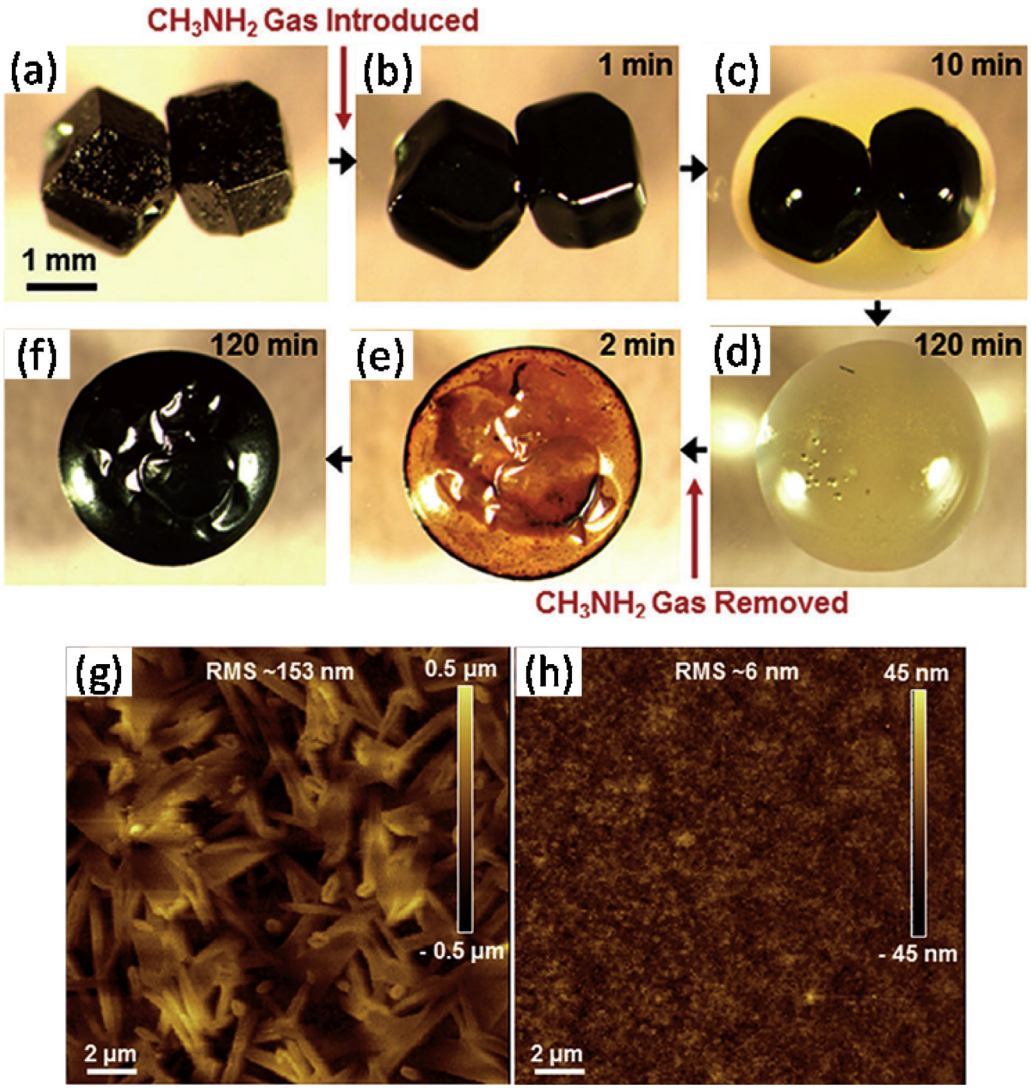

Fig. 26. In situ optical microscopy of the morphology evolution of two touching $MAPbI_3$ perovskite crystals (same magnification) upon exposure to CH_3NH_2 gas and CH_3NH_2 degassing: (a) before CH_3NH_2 gas exposure, (b) CH_3NH_2 gas introduced, (c) partial collapse of perovskite structure and conversion to liquid, (d) full conversion to liquid, (e) CH_3NH_2 degassing, and (f) perovskite back-conversion completed. AFM images of top surfaces of $MAPbI_3$ perovskite thin films: (g) raw film and (h) healed film [139].

4.2.3. Amine-gas treatment

Amine-gas treatment is a recently developed novel post treatment for perovskite films, where the perovskite film was exposed to amine-gas environment [139]. Upon exposure to the MA gas, an intermediate $MAPbI_3$·xMA liquid phase will form due to the unusual perovskite-gas interaction. After the removal of the MA gas, the liquid $MAPbI_3$·xMA phase will be recrystallized to the $MAPbI_3$. Among all types of amine gas, the methylamine (CH_3NH_2, MA) was the best for the $MAPbI_3$ film treatment [139]. When a smaller molecule amine gas (NH_3) was used for the treatment, a photo-bleaching effect was observed instead of the formation of liquid phase. For the larger molecule amine gas such as $C_2H_5NH_2$ and $(CH_3(CH_2)_3NH_2$, although a liquid phase can be formed, it cannot be fully recovered to $MAPbI_3$ phase after the degassing. Fig. 26 shows the in-situ optical microscopy of the morphology evolution of two touching $MAPbI_3$ perovskite crystals upon exposure to MA gas and MA degassing. As shown in the figure, the surface of the perovskite crystal became shiny after 1 min of MA gas treatment, and the two adjacent crystals were fully converted to liquid phase after 120 min treatment. The liquid phase is fully recovered to solid phase after removal the MA gas for 120 min. The treatment time could be shortened to 2–3 s for the $MAPbI_3$ films. Fig. 26g–h show the AFM images of the one-step deposited $MAPbI_3$ films before and after the MA gas treatment. The surface roughness of the perovskite film was reduced dramatically from 153 to 6 nm.

In addition to the smoother surface, the $MAPbI_3$ film's grain orientation and its infiltration to the mesoporous TiO_2 substrate was also improved. After the MA gas treatment, the $MAPbI_3$ film with different orientation became a phase pure, (1 1 0) direction oriented perovskite films. The mesoporous TiO_2 film can also be fully infiltrated with $MAPbI_3$ after the MA gas treatment, which should be good for the charge extraction.

5. The role of chloride in perovskite solar cells

The introduction of chloride (Cl) into $CH_3NH_3PbI_3$ system to form a compound of $CH_3NH_3PbI_{3-x}Cl_x$ for solar cells was first reported by Snaith, et al. where they achieved a PCE of 15% in 2013 by a simple planar structure [2]. It was then revealed by multiple groups that the diffusion lengths of holes and electrons in $CH_3NH_3PbI_{3-x}Cl_x$ are balanced and exceed over 1 μm [12,140,141], comparing to $CH_3NH_3PbI_3$ with unbalanced [141] or one order of magnitude shorter diffusion lengths [12,14]. It is evidenced by the time-resolved PL measurements, shown in Fig. 27, that $CH_3NH_3PbI_{3-x}Cl_x$ films have much longer carrier lifetime than $CH_3NH_3PbI_3$ films [12,14]. From device perspective, it is reported that introducing 5 wt% Cl in the precursor solution can decrease the final device series resistance from 14 ± 1 to $7 \pm 1\ \Omega\ cm^2$ [142]. In the meantime, the J_{SC} increases from 19 to 22.9 mA/cm^2, which is thought to be resulted from increased carrier diffusion length due to Cl inclusion [142].

However, why Cl improves perovskite solar cell performance remains an open question. It is generally observed that the final content of Cl in annealed perovskite film is below most instruments' detection limit, including energy dispersive X-ray (EDX) analysis, XRD, X-ray photo-electron spectroscopy (XPS), and electron energy loss spectroscopy (EELS), even if the precursor solution contains high content of Cl (e.g., CH_3NH_3I:$PbCl_2$ = 3:1) [83,142–149]. It is believed that MACl would evaporate during annealing due to the volatile nature of MACl and the large ion radius mismatch between Cl^- and I^- in perovskite crystal lattice [143,144]. Zhu et al. spin coated a precursor solution with PbI_2, MAI and MACl at a 1:1:3 molar ratio onto mesoporous or planar TiO_2. High content of Cl (Pb:I:Cl = 1:2.7:1.6) was observed by EDX and XRD initially after 1 min of annealing at 100 °C [8]. With longer time of annealing, the content of Cl decreases and disappears totally in 45 min. McGehee et al. observed directly the evaporation of MACl by analyzing the white powder collected above the perovskite layer during annealing [145]. The XRD pattern of the white powder matches that of MACl.

The trace amount of Cl in annealed perovskite film is measured more recently with alternative methods. Zhao et al. prepared the perovskite film by spin coating a precursor solution of MAI and

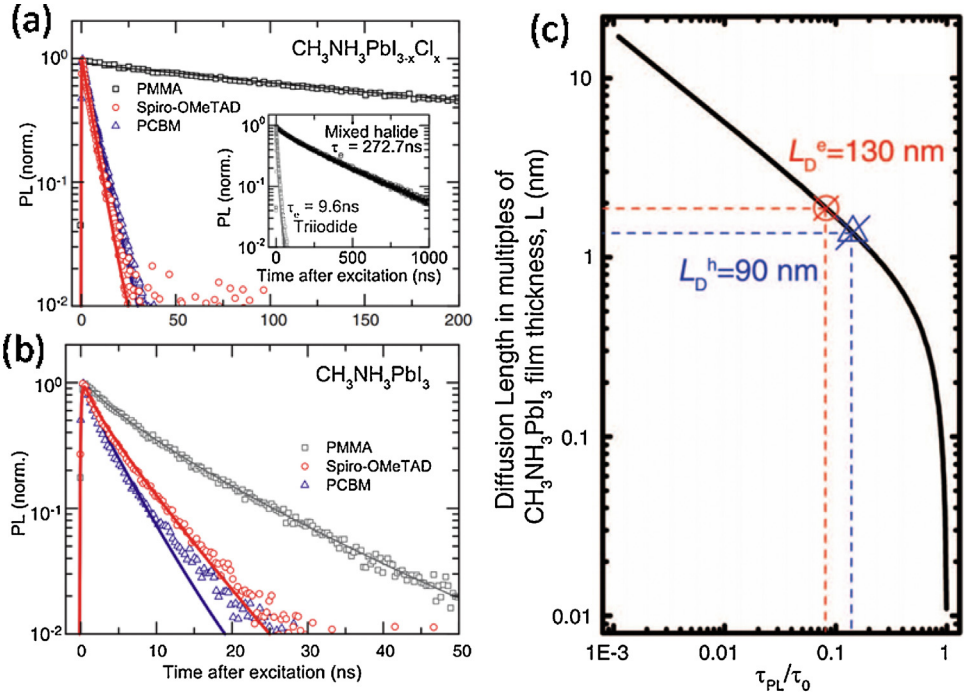

Fig. 27. a–b, Time-resolved PL measurements taken at the peak emission wavelength of the (a) $CH_3NH_3PbI_{3-x}Cl_x$ and (b) $CH_3NH_3PbI_3$ films with an electron (PCBM; blue) or hole (Spiro-OMeTAD) quencher layer [12]. (c) A plot of exciton diffusion length versus PL lifetime quenching ratios. Diffusion length is scaled in multiples of $CH_3NH_3PbI_3$ layer thickness (L = 65 nm) [14] (For interpretation of the references to color in this figure legend, the reader is referred to the web version of this article.).

$PbCl_2$ in DMF at a 3:1 molar ratio onto FTO substrate, followed by thermal annealing at 100 °C for 50 min [146]. In XPS depth profile measurement, 1% Cl were observed for the top 20 nm of the perovskite film, while no trace of Cl is found at the top surface or 310 nm deep inside. McGehee et al. demonstrated the presence of chloride in $CH_3NH_3I_{3-x}Cl_x$ layer after prolonged annealing by X-ray fluorescence (XRF) measurement [145]. The measured chloride concentration is in the range of $0 < x < 0.3$, which value is an upper limit, however more accurate value cannot be obtained by this method. Colella et al. demonstrated by angel-resolved X-ray photoelectron spectroscopy (AR-XPS) measurement on extremely thin perovskite layer (5 ± 4 nm, annealed at 100 °C for 1 h) that Cl atoms are distributed inhomogeneously in perovskite film, with most of them stay deep near the surface of TiO_2 substrate (where the Cl:I atomic ratio is 0.02:1) [143].

With such small amount of chloride distributed inhomogeneously in annealed perovskite film, its influence on perovskite solar cells performance becomes elusive. Colella et al. calculated by density functional theory (DFT) that chloride prefer to stay close to TiO_2 because of the increased chloride-TiO_2 affinity, and the interfacial chloride would induce band-bending that enhances the carrier collection [143]. McGehee et al. proposed that the residual chloride in perovskite film may stay at the grain boundaries or the interface with the substrate, acting as a kind of dopant or passivant [145].

More works, however, suggest another way that chloride improves the perovskite film quality for solar cells: it optimizes the nucleation and crystal growth of perovskite. As shown in Fig. 28a–d, as the perovskite film becomes more continuous after adding MACl in the precursor solution [144]. Dong et al. recently observed that the addition of Cl enable abnormal grain growth to form large perovskite grains with preferred (2 2 0) orientation when a multi-cycle spin coating was applied (Fig. 28) [150]. Some other studies have shown that precursor solution with excessive $CH_3NH_3^+$ (in form of either CH_3NH_3I or CH_3NH_3Cl) will form intermediate phase first, which retards the crystallization of $CH_3NH_3PbI_3$ [144,146, 148]. Then, a larger grain size of perovskite or better coverage on the substrate is obtained, leading to enhanced power conversion efficiency [144]. The role of Cl^- is suggested to facilitate the evaporation of excessive $CH_3NH_3^+$ during annealing, as MACl is more volatile than MABr and MAI [146]. In addition, it is found that chloride promotes the oriented growth of perovskite crystal, resulting in elongated perovskite crystal structures [149].

If no or short time annealing (~5 min, 100 °C) is applied after spin coating precursor solution containing either a mixture of $CH_3NH_3PbCl_3$ and $CH_3NH_3PbI_3$ or 3:1 molar ratio of CH_3NH_3I:$PbCl_2$ onto quartz or TiO_2 substrates, respectively, a high content of Cl^- would remain in perovskite as $CH_3NH_3PbI_{3-x}Cl_x$ [29,151]. The exact content of chloride is not determined. Generally, increasing the content of Cl in a precursor solution results in an increase of bandgap, leading to continuous blueshift of emission wavelength [29]. Such a mixed halide perovskite layer has been applied for light-emitting and lasing [15,10].

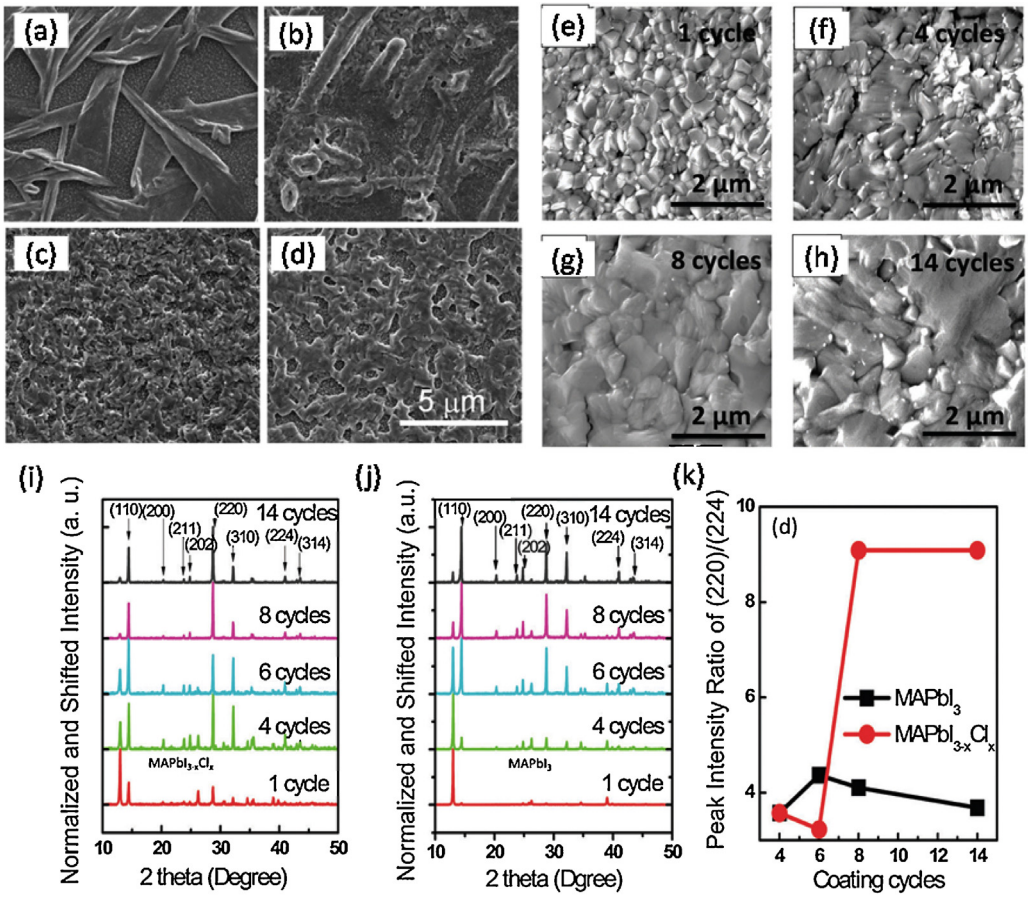

Fig. 28. (a–d) SEM images of the $CH_3NH_3PbI_3$ films grown on planar TiO_2 substrate with different MACl weight ratio in the blend solution: PbI_2, MAI and MACl molar ratio of 1:1:*x*; *x* = 0 (a), *x* = 0.5 (b), *x* = 1 (c), *x* = 2 (d) [144]. (e–h) SEM images of the perovskite films with varied layers of MAI:MACl (molar ratio, 4:1). The PbI_2 was first spin coated on PEDOT:PSS substrate, the MAI:MACl was spin coated on top of the PbI_2 film with different circles [150] (i–j) The XRD patterns of the $MAPbI_{3-x}Cl_x$ and $MAPbI_3$ films annealed at 110 °C for 90 min with different coating-cycles of MAI:MACl or MAI. (k) Intensity ratio of (2 2 0)/(2 2 4) peaks in the annealed $MAPbI_3$ and $MAPbI_{3-x}Cl_x$ films with different coating-cycles of MAI or MAI:MACl [150].

6. Influence of charge transporting layers on device performance

Like any other types of solar cell, interface and charge transport layers play a critical role in achieving high performance devices. Although working perovskite devices without an electron transporting layer (ETL) or a hole transporting layer (HTL) have been reported [152–154], almost all the highly efficient perovskite photovoltaic devices reported so far have both ETL and HTL sandwiching the perovskite active layer. This section summarizes the reported ETL and HTL materials used in highly efficient OTP solar cells.

6.1. Electron transporting layer

TiO_2 is the most widely used ETL material in perovskite solar cells because the initial OTP devices inherit the structure of DSSCs. The OTPs ($MAPbI_3$, $MAPbBr_3$) were designed to work as 'dye' in DSSCs at the very beginning, and the mesoporous TiO_2 layer worked as ETL [1,3,4,20]. Mesoporous TiO_2 provides large surface area, loading space for perovskite "dyes" to attach on, and path for electrons transporting to the cathode electrode. There are increasing efforts using 2D TiO_2 nanowire, nanotube array, 3D inter-connected TiO_2 structures to enhance electron collection. For example, Mahmood et al. employed hyperbranch 3D TiO_2 to replace mesoporous structure with an aim to enhance the electron collection efficiency, and received a decent device efficiency of 15.5% [155]. Nevertheless, the high internal quantum efficiency close to 100% and large V_{OC} of the regular mesoporous structure device indicates the TiO_2 layer does not limit the electron collection, which can be explained by the fact that OTPs are good electron conductor as well. This is evidenced by the fact that replacing TiO_2 by mesoporous Al_2O_3 still resulted in efficient devices with an efficiency of over 12% [4].

There are many issues associated with the TiO_2 for perovskite solar cell application. One issue is the possible energy misalignment of perovskite with TiO_2. Snaith and the co-workers employed a fullerene self-assembled monolayer (C_{60}SAM) to functionalize the mesoporous TiO_2 structure with the regular device configuration. The monolayer of fullerene was used to cap the surface of mesoporous TiO_2, and was reported to block the energy transfer from perovskite to mesoporous TiO_2 due to energy level misalignment and poor electronic coupling between C_{60}SAM and TiO_2 [5]. The C_{60}SAM acted as both 'electron' acceptor and 'electron reservoir' that the electrons from C_{60}SAM transferred back to perovskite and transported to the compact blocking TiO_2 layer for the collection. In this case, the mesoporous structure worked as an absorber loader rather than ETL, and thus the charge transfer route is similar as that in the PHJ perovskite photovoltaic. This strategy allowed a reduction of energy loss happened in charge transfer from perovskite layer to the mesoporous TiO_2, which improved both devices V_{OC} and J_{SC}. Nevertheless, the main function of fullerene might not be related to the increased charge transfer from perovskite to TiO_2 since it is already very fast. Other study by Shao et al. showed that fullerene can passivate the charge traps in the interface of perovskite and charge transport layer [115]. Another issue with mesoporous TiO_2 was found to deteriorate the stability of the perovskite probably due to desorption of surface-adsorbed oxygen under ultraviolet (UV) light [156]. Applying Al_2O_3 instead of TiO_2 was reported to solve the UV instability issue caused by TiO_2 [156]. We believe that Al_2O_3 does not stabilize OTP materials because its bandgap is too large to absorb UV light, and completely removing Al_2O_3 is expected to have the same function of increasing device UV stability.

In addition to the mesoporous TiO_2, a compact TiO_2 layer was broadly applied in the most efficient perovskite solar cells as ETL [157]. Accordingly, the solar cell configuration is evolved from mesoporous structure to planar heterojunction structure. The planar structure device employing only compact TiO_2 showed comparable high efficiencies with the devices using mesoporous structure when high quality large grain perovskite film was achieved [2]. The modification on compact TiO_2 layer can further improve the efficiency. For example, Zhou et al. reached an average 16.6% efficiency through low temperature fabrication procedure (<150 °C) using Yttrium-doped compact TiO_2 layer and polyethyleneimine ethoxylated (PEIE)-modified TiO_2 substrate. Yttrium-doping increased conductivity of TiO_2 by around three times (2×10^{-5} for Yttrium-doped TiO_2 versus 6×10^{-6} for undoped TiO_2), and PEIE reduced the work function of ITO from the original value of −4.6 to −4.0 eV to form a better energy alignment with Yttrium-doped TiO_2, which improved the electron transfer from ETL to the cathode [25]. As the charge transfer between ETL and cathode affects device efficiency, some researchers used graphene quantum dots (GQDs) or nanoflake to improve electron transfer among perovskite, TiO_2 ETL and cathode. In Zhu's work, GQDs was employed to facilitate the charge transfer between mesoporous TiO_2 and perovskite, and it was confirmed by transient absorption measurement. A much faster electron extraction was observed in the perovskite-coated mesoporous TiO_2 film with the GQDs (90–106 ps) compared with the control sample without GQDs (260–307 ps) [158,159]. Wang et al. used nanocomposite of graphene nanoflake and TiO_2 nanoparticles as ETL by spin coating mixing solution of graphene and TiO_2 nanoparticle. The work function of graphene (−4.4 eV) well aligns between that of FTO (−4.6 eV) and CB of TiO_2 (−4.2 eV), resulting in the improved charge collection in the nanocomposites ETL [158].

In addition to TiO_2, many other oxides developed in organic photovoltaic research have been applied in OTP solar cells. For example, *n*-type metal oxides like ZnO have also employed as ETL in planar structure devices to replace TiO_2 due to their high mobility and much lower annealing temperature. In Liu's work, a thin layer of ZnO nanoparticle was fabricated by spin coating at room temperature. A decent efficiency of over 15.0% was reached [160]. This can be an important progress to removing TiO_2 considering the instability associated and high temperature it needs. Unfortunately, it is very challenging to reproduce these results by many other groups, and it is frequently observed that ZnO can react with $MAPbI_3$ quickly, if ZnO is not capped by ligands. More study is thus needed to find out why $MAPbI_3$ is stable on TiO_2 rather than ZnO. Tin oxide (SnO) is another *n*-type electron conductor which has been shown to be compatible with OTPs. Yan et al. used a spin-coated 60 nm thick nanocrystalline SnO layer as ETL and reached a high efficiency of 16.02% and V_{OC} of 1.1 V, compared with the efficiency of 15.17% for the controlled device with TiO_2 ETL [161]. The suitable band edge and high electron mobility of SnO provide good electron extraction ability, which enables SnO to be an alternative ETL to TiO_2 to avoid the high temperature sintering process. Most recently, Seok and the co-workers modified the conventional synthesis route (high temperature reaction >150 °C) of Zn_2SnO_4 by adding $N_2H_4{\cdot}H_2O$ into $ZnCl_2$ and $SnCl_2$ water precursor solution instead of NaOH and amines. Such modification introduces the formation of Zn–N–H–OH complex in the precursor, which enables the synthesis of highly dispersed *n*-type electron conductor Zn_2SnO_4 nanocrystals at low temperature (~90 °C). The Zn_2SnO_4 was spin coated onto flexible polyethylene naphthalate (PEN) flexible substrate to form a very flat ETL with high electron Hall mobility of Zn_2SnO_4 of up to 30 $cm^2\ V\ s^{-1}$ [162]. An efficiency of 15.3% was reached based on $MAPbI_3$ perovskite [162]. The results suggest Zn_2SnO_4 is promising ETL candidate for flexible photovoltaic device. Nevertheless, certain photocurrent hysteresis was observed even in the best-performing device with SnO_2 or Zn_2SnO_4 ETL, which suggests the

current metal oxides ETL including TiO_2 need additional passivation treatment to eliminate photocurrent hysteresis.

Fullerene and its derivatives are another important family of ETL materials used in perovskite photovoltaics due to their right LUMO energy level (−3.9 eV and −3.8 eV for C_{60} and PCBM) aligning to conduction band (CB) of $MAPbI_3$ (−3.9 eV). Fullerenes were frequently observed in the inverted PHJ structure that has HTL closed the substrate and ETL on the top of perovskite. Wen et al. were the first to employ fullerenes as ETL in the PHJ structure with PEDOT:PSS as HTL on the ITO substrate side [8,163]. This device structure resembles that of the organic solar cell with both polymer donor and fullerene acceptor. However, although various fullerenes including C_{60}, PCBM and ICBA were tested, relatively low device efficiency of 3.9% was achieved due to the small V_{OC} of 0.5–0.7 V and J_{SC} of 10 mA/cm^2. This is because the perovskite film itself was not continuous, leading to the direct contact of fullerene ETL and PEDOT:PSS, which formed Schottky contact and caused leaking. To solve this problem, Xiao et al. used interdiffusion method to fabricate continuous perovskite film fully covering the PEDOT:PSS HTL, and significantly increase the device performance and reproducibility, demonstrating 15.4% efficiency with 85% devices over 14.5% based on the similar structure using double fullerene layer as ETL [21]. In addition to working as ETL, PCBM and C_{60} was found to passivate the perovskite grain boundary and surface, which can eliminate the photocurrent hysteresis. Wang et al. and Xiao et al. employed double fullerene layer (PCBM and C_{60}) to passivate the defects of the perovskite film and no photocurrent hysteresis was observed in the planner structure device [21,26,164]. The passivation effect of fullerenes is discussed in Section 3.1.

In addition to the energy levels, the electron mobility of fullerenes also affects the device efficiency because of the varied electron collection capability. Jen et al. employed varied fullerenes including ICBA (LUMO energy level at −3.6 eV), PCBM and C_{60} in the PHJ perovskite device to study the effect of fullerene-based ETL on device performance, as shown in Fig. 29a. They attributed the largest electron mobility of C_{60} (1.6 cm^2 V s^{-1}) to the highest efficiency achieved from the C_{60} ETL-based device, while the lowest mobility in ICBA (6.9×10^{-3} cm^2 V s^{-1}) yielded the lowest performance, as shown in Fig. 29b [94]. This work tried to build the correlation between the charge transport property of fullerenes and photovoltaic performance, but the effect of energy level mismatch could not be excluded especially for ICBA.

6.2. Hole transporting layer

HTLs are also essential components for most efficient perovskite solar cell. Generally, HTL materials can be divided into three categories: small molecules, polymers and inorganics. For the small molecule HTLs, Spiro-OMeTAD is one of the most widely-used one in both mesoporous and planar perovskite solar cell because of the history in perovskite solar cell development as well as its aligned highest occupied molecular orbital (HOMO) level (5.22 eV) to $MAPbI_3$'s (5.46 eV) [1,4,20]. Due to the relatively low mobility, dopants including lithium bis(trifluoromethanesulfonyl)imide salt (LiTFSI), 4-tert-butylpyridine (TBP) and cobalt complex are usually

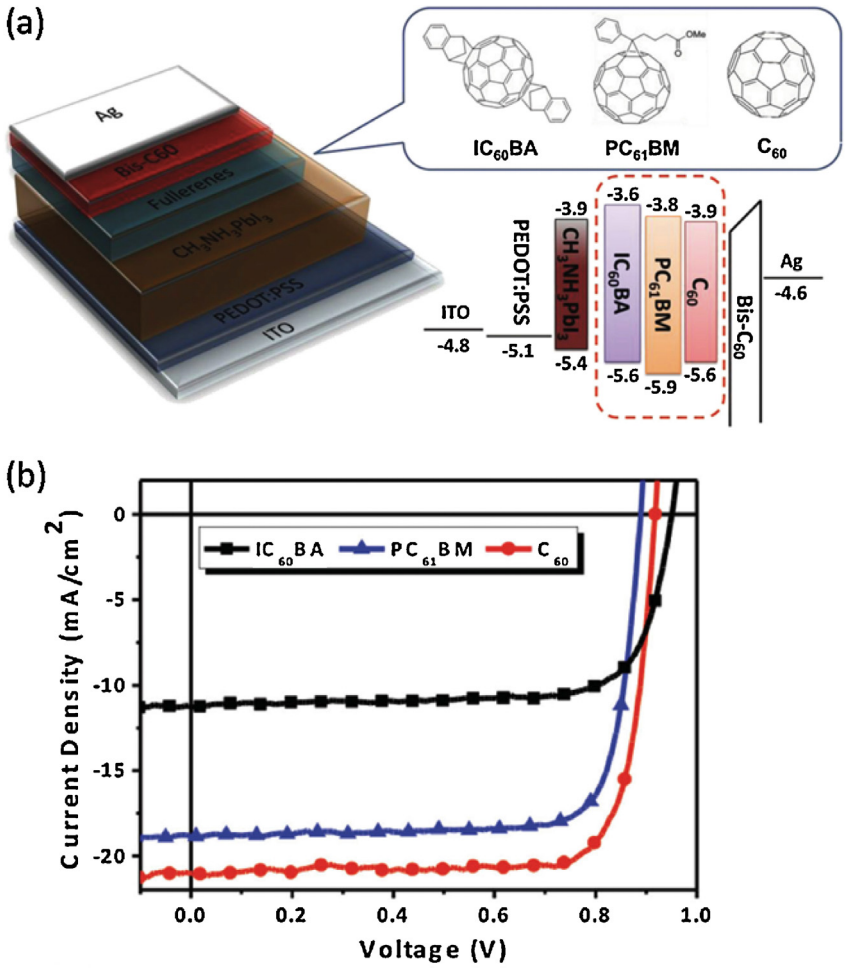

Fig. 29. Structure and energy level diagram (a) and *I–V* curve (b) of the devices using varied fullerenes as ETL [94].

used to dope Spiro-OMeTAD for improved conductivity by adding them in the Spiro-OMeTAD solution before spin coating, which however might cause the low stability of these HTLs [1]. Some research works have been done for dopant-free small molecular HTL material. Kazim et al. employed dopant-free and cost-effective HTL material, 6,13-bis(triisopropylsilylethynyl) pentacene (TIPS-pentacene), which has relative high hole mobility (>1 $cm^2 V^{-1} s^{-1}$) due to the cofacial of π–π stacking [165]. Although they obtained 11.82% device efficiency in regular device configuration with TiO_2 mesoporous structure, it was still less competitive to Spiro-OMeTAD which had already demonstrated over 19.0% efficiency [166].

PEDOT:PSS is another widely used HTLs in planner structure devices with a work function of around 5.0 eV, and can be deposited by the low-temperature spin coating process. However, the energy-level misalignment between PEDOT:PSS's work function (5.0 eV) and VB of $MAPbI_3$ (5.46 eV) may be responsible for the lower device V_{OC} (typically ranging from 0.80 to 1.02 V). Kim et al. modified the PEDOT:PSS's work function by using additives to increase the value up to 5.4 eV. As a result, the V_{OC} of the perovskite device was increased to 0.98 V after the additive treatment, compared with the V_{OC} of 0.83 V for the controlled device without additive treatment [167]. It should be noted that the high work function of HTL did not guarantee the large device V_{OC} as the small perovskite grains grown on the wetting HTL lower the V_{OC} through the stronger charge recombination at the grain boundary. This is because the energy level of HTL might not limit the Fermi energy splitting of the device. In Bi's work, nonwetting HTLs including c-OTPD and PTAA was used to grow large aspect ratio (over 3 for PTAA) perovskite grains. Although neither c-OTPD or PTAA showed work function larger than 5.4 eV, A V_{OC} of 1.1 V and 18.3% stabilized power output was achieved [23]. Similarly, in Zhao's work, poly-TPD HTL was used to replace the PEDOT:PSS, which yielded an enhanced V_{OC} up to 1.1 V due to both the better energy level alignment and larger perovskite grains grown on poly-TPD [168]. Nevertheless, if the bandgap of the perovskite material so large that the energy level of the HTL limits the quasi-energy level splitting, the HTL's energy level can significantly affect the device V_{OC}. Im et al. fabricated highly efficient $MAPbBr_3$ solar cell by using various HTLs with different HOMO level: P3HT, PTAA and PIF8-TAA. They found the device V_{OC} increased significantly from 1.09 to 1.51 V with neglected change on J_{SC} and FF when P3HT was replaced by PIF8-TAA, as shown in Fig. 30 [169]. The significant improvement in device V_{OC} resulted from the lower HOMO level of PIF8-TAA (5.5 eV) which is comparable to valence band of $MAPbBr_3$ (5.7 eV), while P3HT (−5.0 eV) and PTAA (−5.1 eV) had higher HOMO level, causing energy loss during the charge transfer [169].

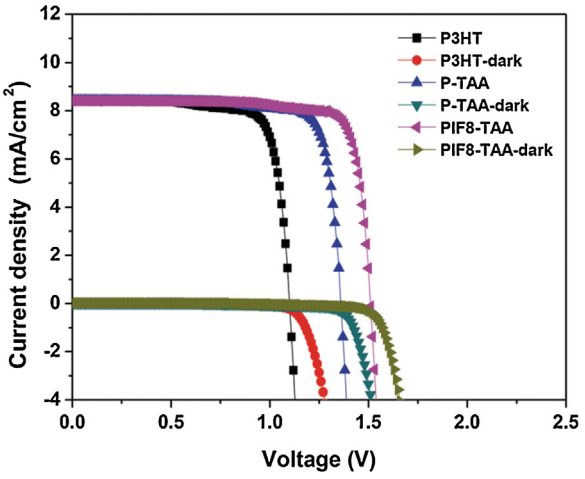

Fig. 30. *I–V* curve of the $MAPbBr_3$ devices employing varied HTLs: P3HT, PTAA and PIF8-TAA [169].

Currently, the PTAA HTL is frequently used in many highly efficient $MAPbI_3$ perovskite solar cells due to its proper HOMO energy level and high hole mobility in the scale of 10^{-2}~10^{-3} $cm^2 s^{-1} V^{-1}$ [15]. It should be noted that the dopants including LI-TFSI and TBP were still used to improve the PTAA conductivity, probably because the PTAA layer was still too thick (around 50 nm) in that work [157]. Besides Li-TFSI and TBP dopants, Wang et al. found 2,3,5,6-Tetrafluoro-7,7,8,8-Tetracyanoquinodimethane (F4-TCNQ) can also doped with PTAA for the increased conductivity and the device performance. A small amount of F4-TCNQ (1%, wt) in PTAA increased the V_{OC} (1.05 V–1.09 V) and FF (65.7–74.0%) without sacrificing the J_{SC} [170]. This work pointed out the limitation on the current polymer HTLs and indicated the way to further improve the device efficiency that is reducing the charge transport layer's resistivity.

Besides organic HTL materials, some *p*-type metal oxides are found to be good hole-transport materials [171–173]. Jen and the co-workers spin coated Cu-doped nickel oxide (NiO_x) film and found its PL quenching effect to $MAPbI_3$ was as good as PEDOT:PSS's. The devices based on NiO_x HTL showed significant improvement in V_{OC} of 1.1 V, compared with 0.90 V of the controlled device using PEDOT:PSS. Better device stability was observed due to its non-acidic properties and the ability to blocking electrons [174]. The device with NiO_x HTL remained above 90% original efficiency after exposed in air for 240 h. However, there is no data to show the device long term stability under illumination. In addition to NiO_x, another metal oxide, MoO_x, can work as hole extraction interfacial layer that combined with cheap metal electrode such as Al to replace noble/precious metal. 10 nm-thick MoO_x layer/Al on the top of HTL can provide similar device efficiency to the Ag electrode [175], which gives a way to lower fabrication cost. However, we found MoO_x is detrimental to the device performance due to its reaction with $MAPbI_3$. Copper iodide (CuI) and copper thiocyanate (CuSCN) are copper-based *p*-type inorganic hole conductors. The features including potential low-cost, solution process, large bandgap, right energy level and high conductivity, made them an alternative HTL material to expensive ones such as Spiro-OMeTAD. CuI was reported as a good HTL for perovskite, and the device efficiency using CuI as HTL was comparable to the controlled devices with Spiro-OMeTAD [176]. However, both the devices with CuI and Spiro-OMeTAD HTLs showed weak performance with only 6–8% efficiency. Grätzel and the co-workers achieved 12.4% efficiency of $MAPbI_3$ solar cell using another low-cost inorganic HTL material, CuSCN, by doctor-blading, which integrated inexpensive material and low-cost process for photovoltaic application [177]. Nevertheless, the demonstrated efficiency still gave less competition to the current widely-used HTL and no data to show the device long-term stability and photocurrent hysteresis. Most recently, Chen et al. used highly doped heavily *p*-doped (p^+) $Ni_xMg_{1-x}O$ as hole transporting layer and *n*-doped (n^+) TiO_x as electron transporting layers. High FF of >80% was achieved due to the increased conductivity of the charge transporting layers by doping. High and stable efficiency of >15% was reached for the $MAPbI_3$ solar cell with large device area of 1 cm^2 [178]. It is also exciting that the PCE only decreased by ~5% after 1 week of storing in air without sealing.

7. Photocurrent hysteresis mechanism and perovskite solar cell measurement

7.1. Mechanism for the photocurrent hysteresis

One unusual and unique characteristics of OTP solar cells is the presence of photocurrent hysteresis in the current (*I*)–voltage (*V*) measurement under light illumination. The photocurrent hysteresis is defined as that the shape and magnitude of the measured *I–V* curves are varied with different measurement parameters, such as

the scanning direction, the scanning rate, and the illumination conditions prior to the measurement. Photocurrent hysteresis has been observed in both mesostructured [25] and planar heterojunction [101] perovskite solar cells. The mechanism of the photocurrent hysteresis is still under debate. So far, several hypotheses about the origins of the photocurrent hysteresis have been proposed and are reviewed here.

7.1.1. Ferroelectricity

Many perovskite structure materials, such as Barium titanate ($BaTiO_3$) and lead zirconate ($PbZrO_3$), are ferroelectric materials. Thus it is natural to speculate a correlation between the hysteresis behavior and the ferroelectricity of OTPs. A ferroelectric material has spontaneous electric polarization which can be aligned by the application of external electric field. The flip of the dipoles induces the polarization current which would add on the photogenerated current of OTP devices and contribute to the photocurrents hysteresis. It is also suspected that the ferroelectric polarization can affect the device charge separation and collection efficiency resulting in photocurrent hysteresis [179,180]. However, the existence of the ferroelectricity in OTPs is still controversial from both theoretical and experiment studies. From theoretical calculation, Frost et al. [180] predicted a large electronic polarization of 38 $\mu C/cm^2$ for $MAPbI_3$ which is comparable to ferroelectric oxide perovskites (e.g., 38 $\mu C/cm^2$ for potassium niobate ($KNbO_3$) [181]). However, the calculation results of Fan et al. [55] showed only a small polarization of 8 $\mu C/cm^2$ for $MAPbI_3$ which origins from a weaker off-center motion of Pb atom. The results from Zheng et al. [182] even denied the existence of polarization in macroscopic scale since an anti-ferroelectric tetragonal structure is more stable than the ferroelectric counterpart according to their calculation. Wei et al. [28,183] claimed an experimental evidence of ferroelectricity with their measured polarization (P)–electric (E) field loops of $MAPbI_3$. However, either back-to-back diodes which result from Schottky-like electrodes on many non-ferroelectric materials [184] or the leakage current [185] can give very misleading 'hysteresis' P–E loops which makes these previous P–E loops suspicious. To prove the existence of ferroelectricity convincingly, the remnant polarization has to be measured. In Xiao et al.'s work [37], no appreciable stable remnant polarization in $MAPbI_3$ was detected at room temperature or low temperature of 77 K. There is increasing study using by piezoresponse force microscopy (PFM) to study ferroelectricity because it is a mechanical based measurement. Kutes et al. reported the first observation of ferroelectric domains in $MAPbI_3$ [38]. However, these ferroelectric signals may come from the injected charges from the too large applied electric field during the poling process. In sharp contrast, no ferroelectric signals were detected in PFM measurement from both Wei and Xiao's study [37,183]. It should be noted that PFM can also give artifacts in identification of ferroelectricity of materials. There are an increasing number of reports on observation of the ferroelectric-like behavior in non-ferroelectric materials by PFM [186,187]. The electret effect, ion migration, surface charging, and other effects can cause the PFM contrast almost in any non-ferroelectric material. Therefore, there is a growing consensus that PFM by itself cannot be used for unambiguous confirmation of the ferroelectric nature of a material. In addition to PFM, temperature-dependent polarization, dielectric and structural measurements are required to confirm ferroelectricity. More evidences are needed to clarify the ferroelectricity of OTPs, and even if they are ferroelectric, the correlation between the ferroelectricity and photocurrent hysteresis.

7.1.2. Surface charge traps

The photocurrent hysteresis can also be explained by the dynamic electric field/charge injection modulated charge trapping and detrapping processes which has been observed in many defect-rich, organic-based electronic devices [188]. The possible mechanisms are illustrated in the Fig. 31a–b [22], at the initial status of the reverse scanning (from open circuit to short circuit), the surface trap states have already been filled by the injected charges due to the applied positive bias voltage, so the photogenerated charges can be collected with higher efficiency, resulting in a larger photocurrent. Conversely, at the initial status of the forward scanning (from short circuit to open circuit), the trap states on the interface are depleted by the reverse bias. Therefore part of the photogenerated charges need to fill these trap states, and the trapping effect reduce the charge collection efficiency and cause a low photocurrents. The trapping–detrapping induced variation of charge collection efficiency results in the photocurrent hysteresis. Recently, Reenen et al. used the drift-diffusion model to simulate the photocurrent hysteresis in perovskite solar cells, and found that both ion migration and electronic charge traps are responsible for the hysteresis [189].

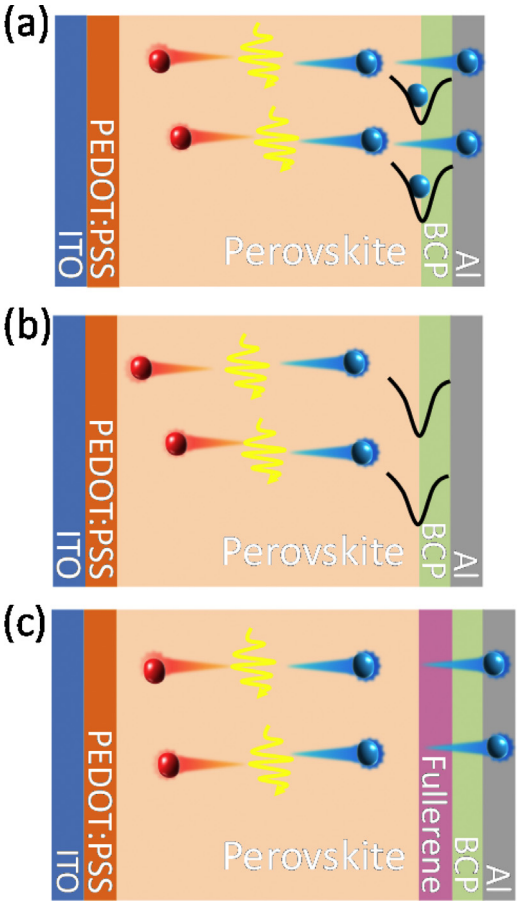

Fig. 31. Mechanisms of surface trap induced photocurrent hysteresis (a) with reverse scanning and (b) forward scanning. (c) Schematics of the surface recombination reduction by passivating the trap states.

The presence of large density of traps close to the surface of perovskites can be explained by the low thermal stability of these materials. Compared with the traditional inorganic semiconductors, OTPs are hybrid materials with much lower thermal stability. A study by M. Grätzel's group [100] showed that $MAPbI_3$ decomposed after thermal annealing for a short time at 150 °C. Bi et al. found that perovskites decomposed to PbI_2 at a lower thermal annealing temperature of 105 °C if the thermal annealing duration was as long as 3 h [21]. The decomposition at surfaces or grain boundaries may occur at a much lower temperature which yields non-stoichiometry composition and dangling bonds and can

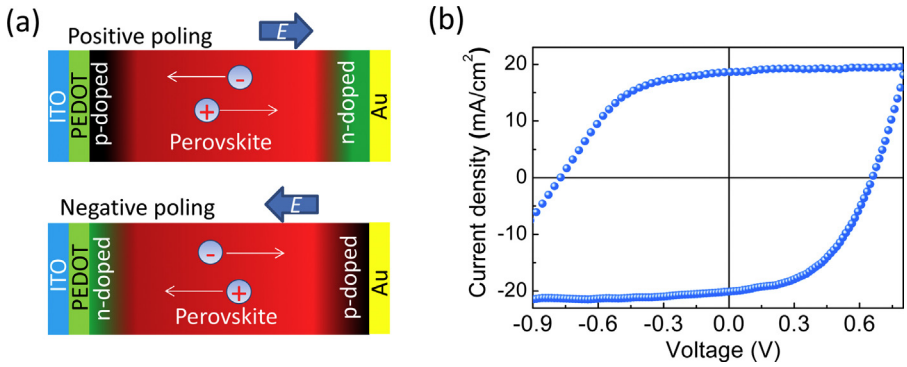

Fig. 32. (a) Schematics of ion drift in perovskite during poling, and the accumulated ions in the perovskite near the electrodes induced *p*- and *n*-doping. (b) the J_{SC} of the OTP devices was switched between 18.6 and −20.1 mA/cm^2 under one sun illumination.

cause midgap states and charge traps. Shao et al. demonstrated fullerenes deposited on the top of the perovskites can eliminate the photocurrent hysteresis by reducing the trap density more than two orders of magnitude [22]. As illustrated in the Fig. 31c, after deactivating these surface traps, the charge collection efficiency remains high regardless of the scanning directions. Thus the photocurrents hysteresis becomes negligible after spin coating and thermal annealing the fullerene layer with optimized fabrication parameters.

7.1.3. Ion migration

Xiao et al. first demonstrated that the ionic migration could be another reason for the photocurrent hysteresis [37], although it was also speculated in several other publications. As shown in the Fig. 32a, the device structure is ITO/PEDOT:PSS/Perovskite/Au. At a positive bias (electric field points from PEDOT:PSS to Au), the positively charged ions or vacancies moved to the Au side and accumulated there, which resulted *n*-type doping in perovskites close to the Au electrode. Similarly, the negative space charges can *p*-dope the perovskite near the PEDOT:PSS side. The charged ions or ion vacancies induced doping effect forms a *p-i-n* homojunction structure in the perovskite layer. A reversed electric filed can flip the *p-i-n* structure to *n-i-p* by driving the ions to the opposite direction. Thus the direction of the photocurrents in the OTPs device could be switched repeatedly as shown in the Fig. 32b. Xiao et al. also proved that a small electric field is sufficient ($< \sim$1 V/μm) to drive these mobile ions. Therefore, the *I–V* curve measurement with different scanning directions changes the doping states in the area close to the two electrodes and thus the charge collection efficiency in the perovskite solar cells, explaining the widely observed photocurrent hysteresis. A high density of mobile ions was also observed by Zhao et al. later [190].

Recently, Yuan et al. directly observed the drift of methylammonium ions (MA^+) in perovskite thin films by photothermal induced resonance (PTIR) imaging and Kelvin probe force microscopy (KPFM) imaging and confirmed that the redistribution of MA^+ ions is responsible for the formation of the *p-i-n* structure [75]. The iodide ions migration was also directly observed at elevated temperature of 60 °C [191]. Macroscopic studies showed that at room temperature, the ions start to drift at an electric field as small as ~0.3 V/μm with mobility of 10^{-9} cm^2/V s and activation energy of 0.36 eV.

7.1.4. Capacitive effect

Photocurrent hysteresis has also been reported in CIGS, CdTe and amorphous silicon solar cells that with large capacitance or measured with high scanning rates [192,193]. Both of the conditions lead to high capacitive current (I_C) which is defined as [194]

$$I_C = C\frac{dV}{dt} + V\frac{dC}{dt}$$

where, C is the capacitance and V is the applied voltage. The measured photocurrent in *I–V* scanning is the sum of I_C and the steady-state photocurrent. Because d*V*/dt is determined by the scanning direction and scanning rate, I_C also depends on the measurement parameters. For example, I_C has positive value with reverse scanning and caused photocurrents being underestimated. Conversely, the negative I_C can exaggerate photocurrents when applied voltage scans from open circuit condition to short circuit condition. Therefore, the measured photocurrents hysteresis could be caused by the variation of I_C. A giant dielectric constant which indicates large capacitance has been observed in perovskite solar cells under illumination in low frequency range (~0.28 Hz), which however should be related to the charge trapping effect [49]. Consequently, the capacitive effect was hypothesized as one of the origin of the photocurrent hysteresis. Kim et al. demonstrated this effect in mesoporous titanium oxide (mp-TiO_2) based perovskite solar cells [195]. They found that the capacitance of the devices decrease as perovskite grain size and the thickness of mp-TiO_2 layer increase. And the photocurrent hysteresis was alleviated at the same time. Their simulation results also show that the hysteresis became larger as the scanning rates increases as I_C increases. This is one important feature that make capacitive effect differs from other mechanisms mentioned above.

7.1.5. Recent progress in eliminate photocurrent hysteresis

The presence of photocurrent hysteresis impairs the accurate measurement of PCE. Therefore, it is desirable to eradicate the notorious photocurrent hysteresis. Recently, many hysteresis-free perovskite photovoltaic devices were reported. However, most of them just showed the hysteresis-free photocurrent curves of the champion devices but failed to present the optimization process to eliminate the photocurrent hysteresis. Actually, those data are of significant importance which could be helpful to reveal the mechanism of photocurrent hysteresis and should be reported. For example, the study of Shao et al. showed the photocurrent can be eliminated by just optimizing the fullerene thermal annealing time. Thus the surface charge trap must be one of the reasons for the photocurrent hysteresis in this case since the thermal annealing of fullerene layer should have negligible effect on ferroelectricity, ion migration or capacitance of perovskite devices. Another study from Kim et al. show the presence of mp-TiO_2 layer can mitigate the photocurrent hysteresis which may implies the capacitive effect play an important role in the mesoporous structure perovskite solar cells but their results could exclude the effect from the surface traps.

Table 2
Step-by-step guidelines for proper characterization of perovskite solar cells.

1.	Mask cell appropriately and measure area
2.	Calibrate illumination source
3.	Determine steady-state J_{SC} and V_{OC} and monitor stability
4.	Record forward and reverse J–V curves at various scan rates
5.	Measure steady-state photocurrent at several voltages near P_{max}
6.	Calculate $J_{SC,INT}$ by integrating IPCE data
7.	Cross check results from steps 3–6 for self-consistency
8.	Perform statistical analysis across multiple sample sets

7.2. How to accurately measure the perovskite solar cells?

For photovoltaic community, the PCE is the most important figure of merit. Thus it is difficult to overstate the importance of measuring the PCE accurately. Detailed tips for proper efficiency measurements have been discussed in many articles [196–199]. Usually, an I–V scanning is applied to analyze the performance of a solar cell by sweeping the potential difference between two electrodes and monitoring the current response at the same time. Nevertheless, problems arise due to the unusual photocurrent hysteresis of perovskite solar cells. Regardless of the mechanism behind this phenomenon, the discrepancy between the photocurrents obtained from an I–V scan and those from keeping the solar cells at constant potential was observed when the scanning rates are faster than the response time of the device. Consequently, this discrepancy impairs the accurate determination of the PCE from the I–V scan measurement. It is important to keep in mind that only the steady-state values measured under continuous illumination have the practical significance and should take precedence. Xiao et al. first measured power output at steady-state states to verify the OTP solar cell efficiency. Base on the same idea, a more general guideline for proper characterization of perovskite solar cells has been proposed by Kamat et al. [201] as shown in Table 2. Besides following the general guideline during the characterization of perovskite photovoltaic devices, researchers were also suggested to clarify the detailed measurement parameters in their publications.

8. Tandem device

Traditional photovoltaic devices such as crystalline silicon (c-Si) solar cells have achieved efficiency as high as 25.6% [202,203], which is approaching the fundamental Auger-recombination-constrained Shockley–Queisser limit of 29.4% [204]. Despite this progress, photovoltaics contribute less than 1% of the world's electricity [205]. To make photovoltaics more competitive with conventional fuel energy sources, ultrahigh efficiency and cost effective solar modules are highly desired. It is believed that tandem device combining the conventional efficient bottom solar cell with a high bandgap top cell is the most straightforward way to achieve this goal. As shown in Fig. 33, the top cell with high bandgap (E_{g1}) absorbs the high energy photons ($h\upsilon > E_{g1}$), leaving the low energy photons with energy between E_{g1} and E_{g2} harnessed by the bottom cell. Tandem solar cells can either be constructed as 4-terminal tandem device (Fig. 33a) with individual cells mechanically stacked or 2-terminal monolithically integrated tandem device (Fig. 33b) with sub-cells interconnected through tunneling junction. With multiple absorbers, a tandem device is able to convert photons into electrical energy more efficiently over a broader range of the solar spectrum, and the theoretical efficiency for a double-junction tandem solar cell is up to 42% [206]. The development of practical tandem device has so far been constrained due to the lack of high-efficiency top cells that can be appropriately integrated with existing efficient photovoltaic cells at low cost. Recently the breakthrough in tandem device is very likely to be made with the emerging organic–inorganic halide perovskite solar cells [2,4,20,1,207].

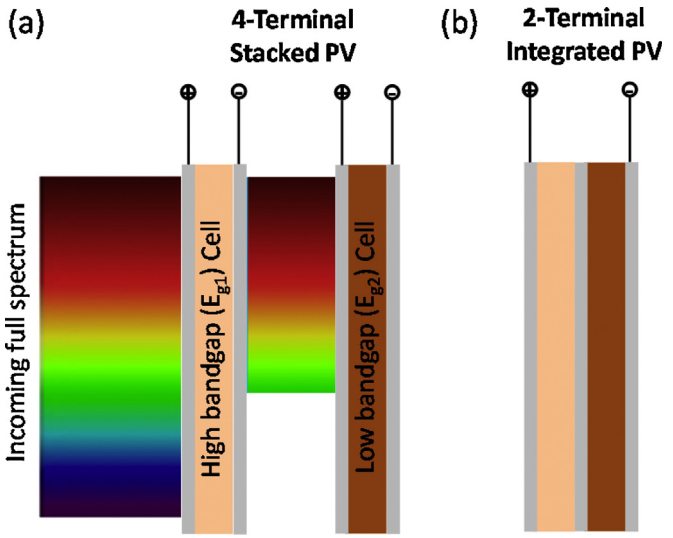

Fig. 33. Double-junction tandem solar cell: (a) 4-terminal design in which cells are electrically connected via external wiring; (b) 2-terminal design in which cells are electrically interconnected by a tunneling junction.

The most commonly used perovskite absorber $MAPbI_3$ is an intrinsic direct bandgap semiconductor with a bandgap of around 1.6 eV. By substituting Br for I to prepare $MAPb(I_{1-x}Br_x)_3$, the bandgap of the $MAPbI_3$ perovskite can be continuously tuned from 1.6 up to 2.25 eV, making perovskite solar cells superb promising candidate as top cells for tandem devices with c-Si solar cell. The ideal bandgap of 1.72 eV can be obtained with a stoichiometry of 1:4 bromine to iodine [208]. To construct double-junction tandem devices with perovskite cells, the bottom-cell absorbers such as c-Si or CIGS with a low bandgap of approximately 1.1 eV should be chosen to achieve the optimal performance.

Although a number of perovskite-based tandem cells have been reported recently, the efficiency is still far below the state of art efficiency for either single junction perovskite or c-Si solar cells. The first example of perovskite based tandems was demonstrated by Löper et al. [209], utilizing a 4-terminal configuration consisting of a perovskite top cell and c-Si bottom cell. The efficiency was improved from 11.6% for the single junction perovskite solar cell to 13.4% for the tandem cell. Soon after, McGehee and co-workers reported a certified efficiency of 17.9% for a 4-terminal perovskite/silicon tandem structure [205]. The stacked CIGS and perovskite tandem further boosted the efficiency up to 18.6% that is much higher than that (12.7%) of both semi-transparent and opaque reference single-junction perovskite solar cells. More recently, a record efficiency of 19.5% was achieved by combining a NIR-transparent perovskite top cell with a CIGS bottom cell shown in Fig. 34 [210]. Most recently, Fu et al. fabricated semitransparent perovskite solar cells using sputtered high mobility hydrogenated indium oxide as rear electrode [211]. The semitransparent solar cell devices reached a PCE of 14.2% with 72% average transmittance in the near-infrared region. The PCE of four terminal tandem solar cell devices with CIGS reached 20.5% which is much higher than each subcell (PCE of perovskite: 14.2%; CIGS: 18.3%).

The parasitic absorption in the electrodes and hole transporter (spiro-OMeTAD) layer still cause significant transmission loss, and thus there remains room for efficiency enhancement for this tandem structure. This issue can be resolved by applying an optical splitter via which multiple solar cells were optically coupled. The optical splitter (Fig. 35) is a multi-layered beam splitter with high reflection in the shorter-wave-length range and high transmission in the longer-wave-length range. By splitting the incident solar

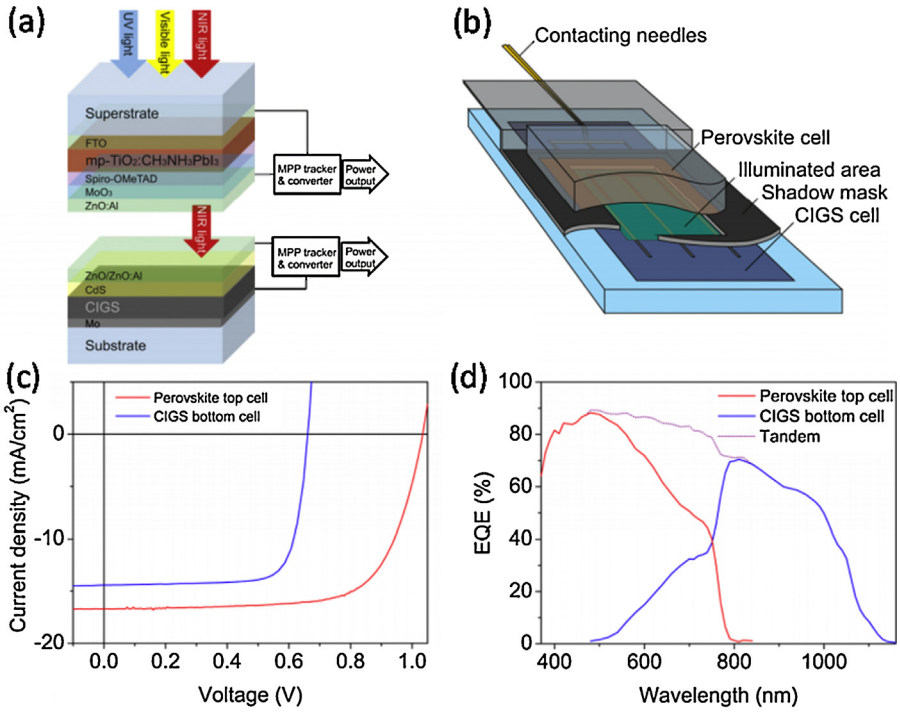

Fig. 34. (a) Schematics of a stacked 4-terminal perovskite/CIGS tandem solar cell. The top cell is a perovskite cell in superstrate configuration and the bottom cell is a CIGS cell in substrate configuration. (b) Schematics of the setup for *J–V* characterization of CIGS bottom solar cells. (c) *J–V* measurements of the sub-cells. (d) EQE characteristics of the two sub-cells and their addition (tandem) [210].

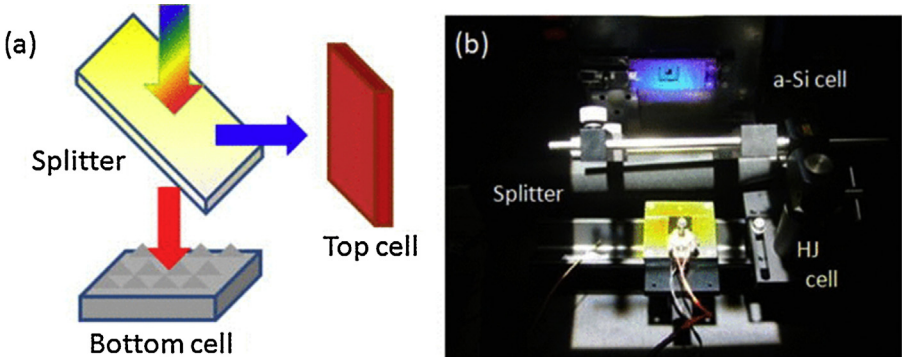

Fig. 35. (a) Schematic image of the optical splitting system and (b) measurement setup of an optical splitting system [212].

spectrum and distributing it to each solar cell, Uzu and co-workers achieved 28% using perovskite and mono c-Si heterojunction solar cells [212]. Despite the ultrahigh efficiency obtained, the complexity of the optical splitter system may raise the cost and difficulty of module installation, retarding the future large-scale application.

In addition to the transmission loss in the 4-terminal tandem configuration, the high series resistance as well as the additional external wiring of the two separate solar cells limits the practicality of this design. The preferred monolithic 2-terminal tandems which are theoretically able to deliver superior performance at lower cost have also been demonstrated recently. Guha et al. reported the fabrication of a 2-terminal tandem with perovskite and kesterite copper zinc tin sulfide (CZTS) as top and bottom cells, respectively [213]. Despite a high V_{OC} of 1350 mV, the obtained efficiency of 4.6% was much lower than the reference single-junction perovskite cell (12.3%). This lower efficiency was a result of the semi-transparency of the top aluminum electrode, causing significant transmission loss. Another 2-terminal tandem structure was realized by monolithic integration of perovskite and polymer sub-cells in Yang's group [214]. With a bottom ITO glass electrode, higher transmittance (transparency >95%) was achieved. Furthermore, a new IR-sensitive block copolymer, PBSeDTEG8, with photosensitivity up to 950 nm was used to broaden the photoresponse of the tandem device, delivering a higher efficiency of 10.2% than those of single-junction perovskite and polymer based devices [214]. More recently, a 1 cm^2 2-terminal monolithic perovskite/silicon tandem cell (Fig. 36) was successfully demonstrated with a V_{OC} as high as 1.65 V, which is expected sum of the V_{OC} of perovskite and filtered Si [215]. Since the perovskite and Si layers in this tandem prototype were not yet best-in-class, the obtained efficiency of 13.7% is still lower compared to the record efficiency for either perovskite or Si cells. Further improvements are expected to be achieved by replacing the spiro-OMeTAD layer with wider bandgap hole transport material, improving the quality of the perovskite absorber, using dedicated furnaces for the Si sub-cell fabrication, and by implementing better surface passivation schemes on the front and back side of the Si sub-cell.

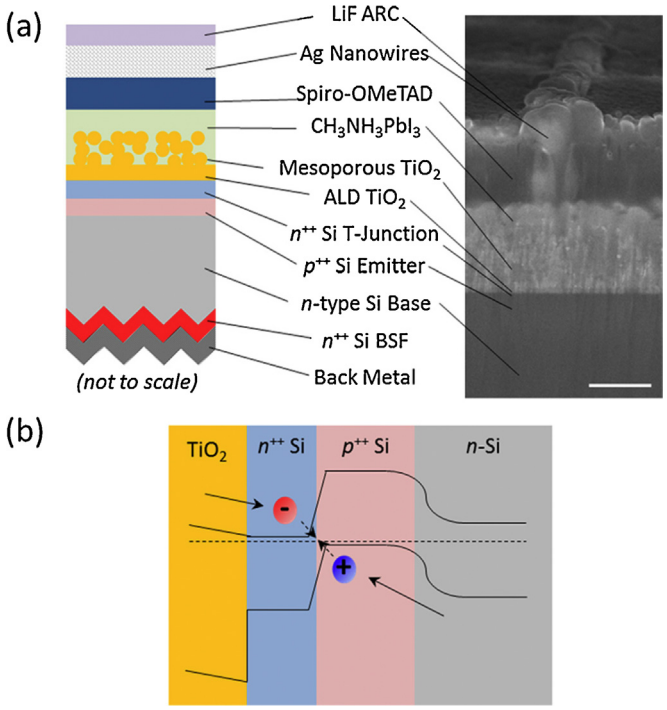

Fig. 36. (a) The device structure of a 2-terminal monolithically grown perovskite/Si multijunction solar cell with an *n*-type Si base. The polished SEM image is taken at 45° tilt to show the Ag nanowire mesh (500 nm scale bar). (b) Band diagram of the perovskite/silicon cell interface showing the charge-transport mechanism around the Si tunnel junction [215].

The future study of perovskite-based tandem configuration are likely to be focused on the 2-terminal designs as they ultimately allow for a more compact and robust structure. However, an extra tunneling junction/recombination layer (intermediate layer) between sub-cells in this prototype brings additional complexity in design. Typically highly *n*- and *p*-doped multi-layers are required to establish the interconnection to facilitate carrier tunneling and recombination. Despite the successful demonstration of several intermediate layers (e.g., PEDOT:PSS/ITO [213], TiO_2-PFN/PEDOT:PSS (PH500) [214], n^{++}/p^{++} Si tunnel junction layer [215]), the efficient perovskite tandems have not been realized yet. Judicious designs that are compatible with existing manufacturing processes are still highly desired in terms of minimizing the transmission and electrical loss.

Moreover, a durable top electrode with superior transparency as well as conductivity is crucial to construct an efficient perovskite tandem solar cell. A number of transparent electrodes such as ultrathin metal (e.g., Al, Au) [217,218], Ag nanowires (Ag NWs) [205,219,220], PEDOT:PSS [221,222], graphene [223,224], and carbon nanotubes[225,226] have been developed for different electronic devices. Nonetheless, it is quite challenging to process on top of perovskite absorbers due to its thermal instability and hygroscopicity. To date, only limited strategies have proven to be feasible for applying transparent top electrodes in perovskite solar cells. Bolink et al. demonstrated an ultra-thin transparent gold electrode (6 nm) capped with a LiF layer which was deposited on top of a very smooth thin perovskite layer by thermal evaporation, leading to an efficiency of 7.3% [227]. Compared with single thin Au layer, a multilayered molybdenum trioxide (MoO_3)–Au–MoO_3 top electrode has shown increased light transmission, thus improving the performance of semi-transparent perovskite to 13.6% [228]. Similar dielectric/metal/dielectric transparent electrode enabled a four terminal tandem solar cell stacking solution processed CIGS and perovskite cells with over 15% efficiency [229]. The most commonly used Ag NWs were also applied as transparent top electrodes in perovskite solar cells via spray-coating [230]. By introducing a thin layer of ZnO nanoparticles, the solution-processed Ag NWs would not cause damage to the underlying perovskite absorbers. Alternatively, lamination approach has been utilized to fabricate Ag NW transparent electrode for perovskite tandem devices [205]. Also, a transparent Ni-mesh embedded PET film can be laminated as top electrode in perovskite solar cell,

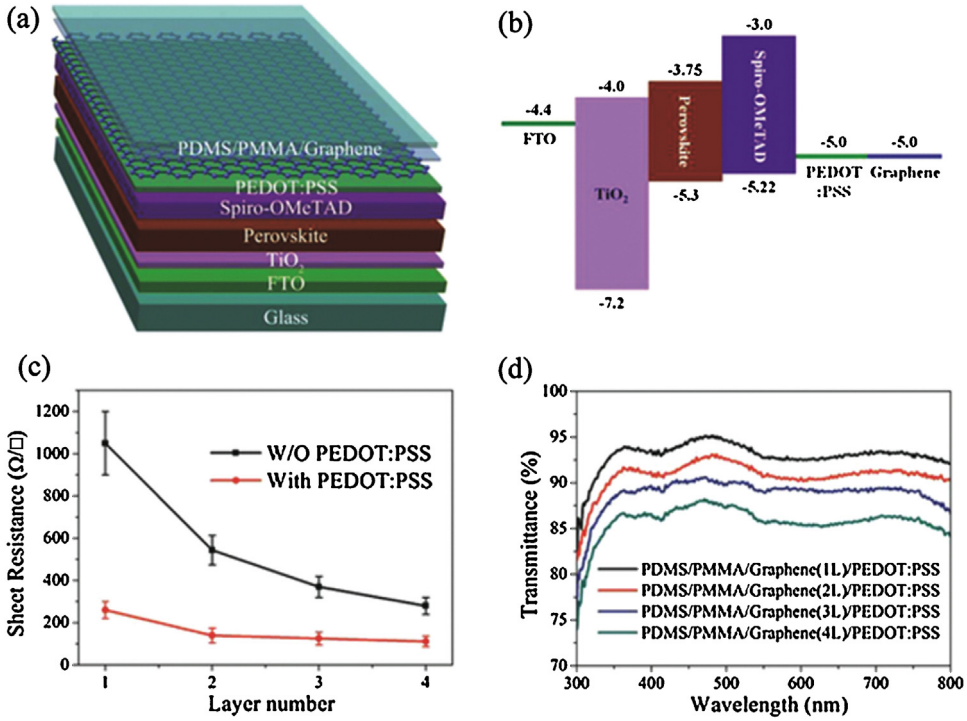

Fig. 37. (a) Schematic diagram of a semitransparent perovskite solar cell. (b) Band structure of the device. (c) Sheet resistance of one to four layers of stacked graphene films before and after PEDOT:PSS doping. (d) UV–vis transmittance spectra of PEDOT:PSS doped transparent graphene electrodes with one to four layers of stacked graphene [216].

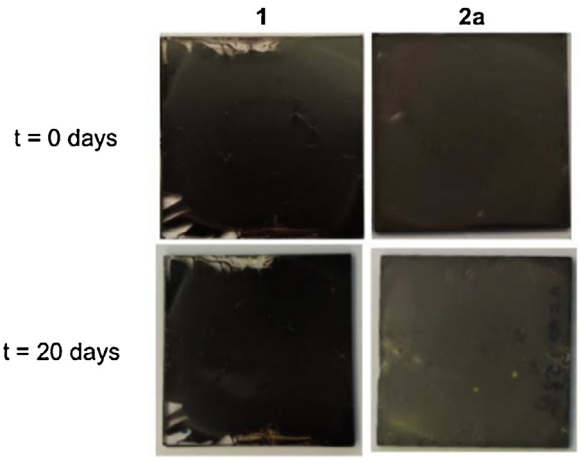

Fig. 38. Photographs of films of $(PEA)_2(CH_3NH_3)_2[Pb_3I_{10}]$ (1) and $(MA)[PbI_3]$ (2a) as deposited (top) and after 20 days (bottom) of exposure to 52% relative humidity [233].

realizing an efficiency over 15% [231]. More recently, a new transparent electrode as shown in Fig. 37 has been fabricated by laminating stacked multi-layer graphene with a thin PEDOT:PSS coating for perovskite solar cells [216]. By optimizing the processing parameters, the devices show the average efficiency up to 11.65% when illuminating from top graphene electrodes.

It is believed that the success of 2-terminal tandem structures would be able to further boost the performance of major current solar technologies (e.g., silicon, CIGS) by monolithically integrating a perovskite subcell on top of the existing device. In order to yield a 30% efficient monolithic tandem, the following tasks have to be accomplished: the realization of (1) transparent electrode that do not compromise V_{OC} and FF, (2) high quality perovskite film enabling top cell efficiency over 18%, (3) good tunnel junction layers in terms of minimizing the transmission and electrical loss and (4) superior silicon bottom cell.

9. Stability

After the hybrid perovskite solar cell exceeded 20%, the stability issue of perovskite solar cells is emerging as the major hurdle for its commercialization [28,156]. There have not been many efforts in understanding the stability of OTP materials, despite the OTP materials are more of concerns than organic semiconductors because there is a new source of instability caused by moisture, in addition to those caused by illumination and oxygen.

9.1. Material stability

Currently, most high-efficiency perovskite solar cells are based on OTP with the very hygroscopic organic cations, which are acknowledged as the main reason that OTP materials are sensitive to moisture, polar solvent and even electrolyte [3,232]. In addition to the organic cation, the halide and metal ions can also influence the stability of OTPs. A larger size organic cation was found to be helpful to increase device stability to moisture. Smith et al. recently reported that the material is more stable by adding long-chain organic cation in MA based OTP [233]. The long-chain organic cation can change the perovskite from 3-dimensional structure to 2-dimensional structure. The materials showed neglected degradation after exposure to moisture for 46 days [233]. Fig. 38 shows the photo-images of the as deposited (top) and after 20 days (bottom) of exposure to 52% relative humidity films of $(PEA)_2(CH_3NH_3)_2[Pb_3I_{10}]$ ($PEA = C_6H_5(CH_2)_2NH^{3+}$) (1) and $(MA)[PbI_3]$ (2a) [233]. The Pb-containing OTP are more stable in air than the Sn-containing counterpart, because Sn^{2+} is easy to be oxidized to Sn^{4+}. The Pb-containing OTP show only surface degradation in the dark with the bulk properties of the materials retained for a couple of weeks in air. For big $MAPbI_3$ single crystals, the metal luster can even keep for more than half year in air condition. On the contrary, the Sn-containing materials are air and moisture sensitive and partially decompose within 2 h before total decomposition after one day [28]. The halide site is also important to the materials stability, Noh et al. showed that the incorporation of certain amount of Br in mixed OTP can increase the stability of the OTP against humidly [234].

The phase transition as well as the molecule structure of organic cations will also affect the stability of OTP materials and devices. For instance, $FAPbI_3$ is another arising OTP material with good device efficiency because of the reduced bandgap. However, the black phase $FAPbI_3$ is unstable at room temperature [102]. Incorporation of more than 20% MA ions in organic cations could stabilize the crystal phase [102,235]. The $MAPbI_3$ has a phase transition temperature near the device working temperature between 300 and 400 K [28], which would also possibly cause unstable device performance [28,232]. The organic cations are found easy to escape from perovskite surface before the OTP fully decomposed at around 500–600 K [28].

9.2. Photostability

Recent works reported the structure and stability of OTP are influenced by illumination [52,236,237]. In our previous work, Deng et al. discovered the light induced self-poling effect in $MAPbI_3$ perovskite solar cells which could increase the device efficiency and stability [236]. When the perovskite solar cell is illuminated, the photovoltage induces additional electric field applied across the perovskite layer which drives the migration of ions/vacancies as shown in Fig. 39. Therefore, the doping level near the electrode was increased due to the self-doping effect, and V_{OC}, J_{SC} and FF of perovskite solar cells increased simultaneously [236]. Gottesman et al. observed $MAPbI_3$ perovskite had a reversible structural change between the dark and the light illumination in Raman and PL measurement [52]. However, in bromide mixed halide perovskite $MAPb(Br_xI_{1-x})_3$, a photo-induced halide segregation as well as photo-induced trap formation was observed under illumination which would decrease device efficiency as well as stability [237]. Hoke et al. reported halide segregation into iodide-rich minority and bromide-enriched majority domains for mixed-halide perovskite $MAPb(Br_xI_{1-x})_3$ under illumination. A new, redshifted peak in photoluminescence spectra increases under one sun illumination and the light soaking causes a splitting of XRD peaks. These photo-induced changes in PL and XRD can recover to their initial states after the materials are left in the dark. This photo-induced phase separation in $MAPb(Br_xI_{1-x})_3$ would cause photo-instability issues of its optoelectronic device. The PL change under light would limit its application in laser devices by using mixed-halide perovskite and the bandgap changes caused by photo-induced phase separation also affect its application in tandem devices [237].

9.3. Device stability enhancement

The hygroscopic nature of OTP material requires a well-designed device structure and encapsulation for the OTP films for a long-term stability [156]. The water resistance capping electrode such as hydrophobic polymer, carbon and polymer/carbon nanotube was integrated in the devices as interfacial layers as well as electrodes, which showed as effective methods to improve the stability of device to moisture and air [238,153]. Mei et al. have provided striking evidence by using carbon as electrode and the device with PCE of ~10% were stable in air for more than 1000 h

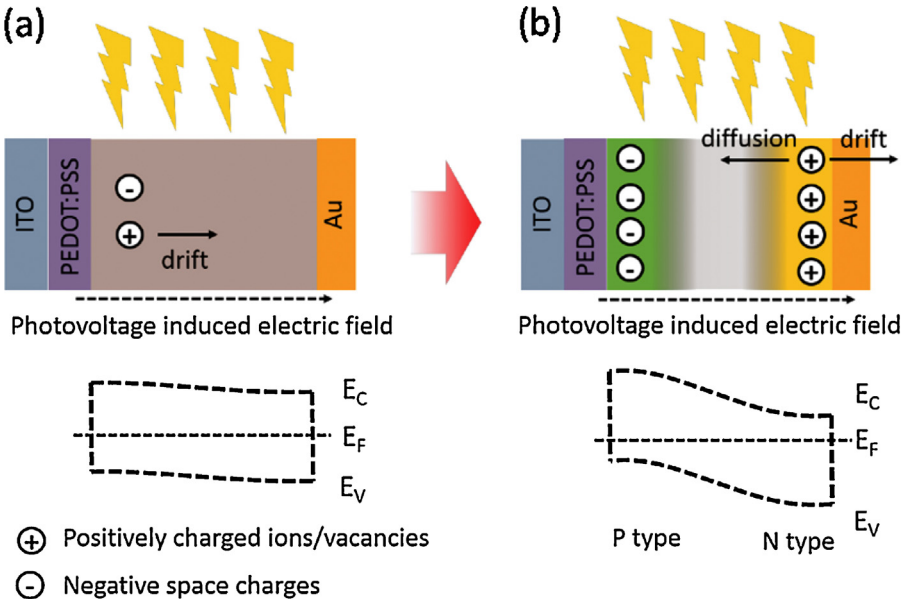

Fig. 39. Schematics showing the light induced self-poling (LISP) process in OTP solar cells and the energy diagram in OTP layer before and after LISP [236].

without further encapsulation (Fig. 40) [153]. And the incorporation of polymer-capping layer, such as P3HT/carbon nanotube hybrid layer can dramatically increase the stability of OTP devices to water, the device can work well after directly exposure to water (Fig. 41) [238].

The electron and hole-blocking layer also play important role in long term stability of both mesoporous and planar structure OTP solar cells. Mesoporous TiO_2 is the widely used electron-collecting layer, but it is UV sensitive and oxygen serves to pacify deep electronic trap sites at oxygen vacancies in the TiO_2 [156]. Leijtens et al. showed that the stability of the device can be increased by introducing UV filter and replacement of TiO_2 with Al_2O_3. The Al_2O_3-based device showed extremely stable photocurrent of over 1000 h of continuous illumination under AM1.5 solar spectrum [156]. For the coplanar structure devices, the PEDOT:PSS with acidic nature [232,239] also requires developing new hole transporting materials for long-term stability [239]. Most recently, Chen et al. and You et al. reported perovskite solar cell devices with

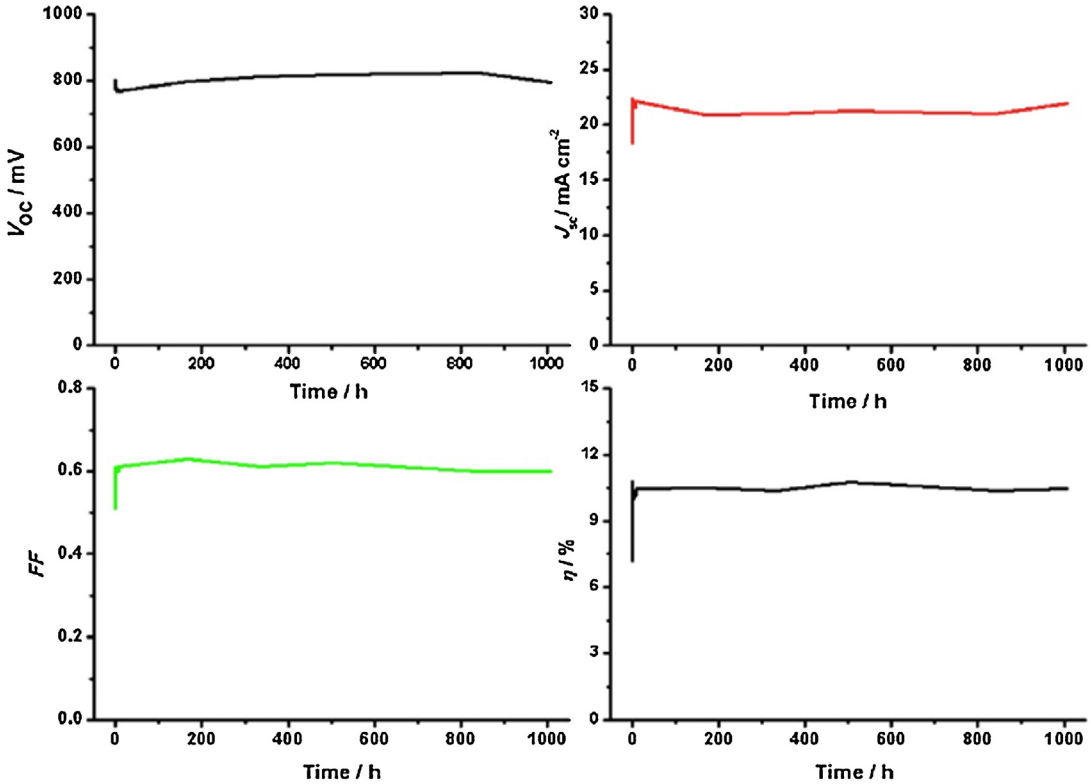

Fig. 40. Stability test of a triple layer $(5\text{-AVA})_x(MA)_{(1-x)}PbI_3$ (5-AVA = 5-ammoniumvaleric acid) perovskite sensitized mesoscopic solar cell effected in full AM1.5 simulated sunlight in ambient air over 1008 h with an unsealed device, the perovskite being protected by the carbon layer acting as back contact [153].

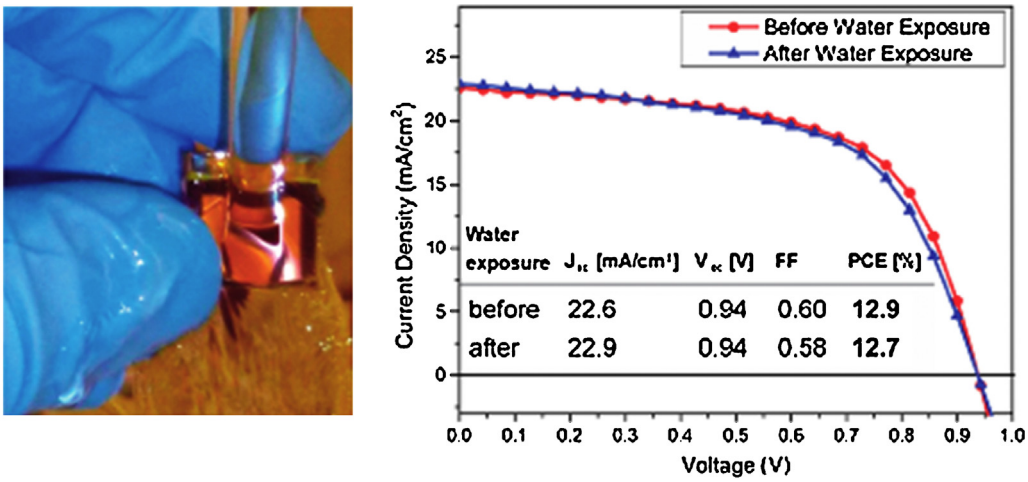

Fig. 41. A photograph of a complete perovskite solar cell employing a PC-SWNT hole-extraction layer placed under a flowing tap with the active layer on the top side of the glass directly under the water flow (left-hand side). Current density–voltage plots measured under AM1.5 simulated sunlight of 100 mW cm^{-2} irradiance of the same perovskite solar cell before and after being placed under the running water for 60 s [238].

improved air stability using solution-processed metal oxide layers [178,240]. In You's work, the solar cell devices retained 90% of their original efficiency after 60 days storage in air at room temperature using compact ZnO layer because it isolates the perovskite and Al layers and prevent the contact of perovskite with humid air.

10. Conclusion and future remarks

In the past five years, accompanying with the device structure evolution from mesoporous to planar structure, and the efficiency enhancement from 3.8% to 20.1%, most of the optoelectronic properties of OTP materials have been figured out gradually including the absorption, exciton binding energy, carrier mobility and diffusion length, etc. The morphology control, which played the most important role in efficiency enhancement in the past few years, has been shown very successful, either from one-step, two-step solution approach, or vapor deposition, to deposit high quality, pin-hole free perovskite films on both mesoporous and flat substrates. In addition, there has also been large improvement on defect passivation, interfacial layer engineering and device structure design. Benefiting from all these works, the efficiency of perovskite solar cell in the lab scale is increased dramatically to over 20% after five years since its first discovery.

Nevertheless, some fundamental understanding of the OTP materials is still lacking which need further study in the next few years. For example, the ferroelectricity of the OTP materials need to be verified and its impact the excellent photovoltaic performance needs to be understood. Many other topics to be studied include the effect of impurities in the precursors on the nucleation and grain growth etc., ion migration on the materials and device stability, and the optoelectronic property of the materials on external stimuli like pressure, light, temperature, electric field, etc. These basic understanding will also greatly assist the development of even higher efficiency devices and/or other perovskite materials with lower bandgap and enhanced material stability.

As the final goal of the perovskite solar cell is its commercialization with low cost, high efficiency, and long term stability modules. Therefore, the large scale fabrication of high-efficiency devices would be the next requisite step of research interests before commercialization. One advantage of perovskite device to this end is its high tolerance to film thickness due to the very large carrier diffusion length, which is a great advantage for mass production techniques where the thickness cannot be precisely controlled. Although both raw materials and fabrication techniques are obviously low cost, the perovskite module may require sophisticated and high cost encapsulation due to the instability of the materials and devices. The appropriate and tunable optical bandgap of OTP materials and low $E_g/q - V_{OC}$ value of OTP photovoltaic devices give the OTP an advantage over other photovoltaic materials in tandem device with crystal silicon and CIGS. However, the top transparent conducting electrode and the intermediate layers are still among the bottlenecks for achieving high-efficiency tandem devices.

Acknowledgements

We thank financial support from Energy Efficiency and Renewable Energy (EERE) SunShot Initiative at Department of Energy under Award DE-EE0006709, and from National Science Foundation Grant DMR-1505535 and Grant DMR-1420645, and from Office of Naval Research under award N00014-15-1-2713.

References

[1] J. Burschka, et al. Nature 499 (2013) 316–319.
[2] M. Liu, M.B. Johnston, H.J. Snaith, Nature 501 (2013) 395–398.
[3] A. Kojima, K. Teshima, Y. Shirai, T. Miyasaka, J. Am. Chem. Soc. 131 (2009) 6050–6051.
[4] M.M. Lee, J. Teuscher, T. Miyasaka, T.N. Murakami, H.J. Snaith, Science 338 (2012) 643–647.
[5] A. Abrusci, et al. Nano Lett. 13 (2013) 3124–3128.
[6] J.M. Ball, M.M. Lee, A. Hey, H.J. Snaith, Energy Environ. Sci. 6 (2013) 1739–1743.
[7] G. Hodes, Science 342 (2013) 317–318.
[8] J.Y. Jeng, et al. Adv. Mater. 25 (2013) 3727–3732.
[9] H.-S. Kim, et al. Nat. Commun. 4 (2013) 2242.
[10] N.-G. Park, J. Phys. Chem. Lett. 4 (2013) 2423–2429.
[11] H.J. Snaith, J. Phys. Chem. Lett. 4 (2013) 3623–3630.
[12] S.D. Stranks, et al. Science 342 (2013) 341–344.
[13] W. Zhang, et al. Nano Lett. 13 (2013) 4505–4510.
[14] G. Xing, et al. Science 342 (2013) 344–347.
[15] J.H. Heo, et al. Nat. Photon. 7 (2013) 486–491.
[16] P. Docampo, J.M. Ball, M. Darwich, G.E. Eperon, H.J. Snaith, Nat. Commun. 4 (2013) 2761.
[17] C. Kagan, D. Mitzi, C. Dimitrakopoulos, Science 286 (1999) 945–947.
[18] D. Mitzi, S. Wang, C. Feild, C. Chess, A. Guloy, Science 267 (1995) 1473–1476.
[19] J.-H. Im, C.-R. Lee, J.-W. Lee, S.-W. Park, N.-G. Park, Nanoscale 3 (2011) 4088–4093.
[20] H.-S. Kim, et al. Sci. Rep. 2 (2012) 591.
[21] Z. Xiao, et al. Energy Environ. Sci. 7 (2014) 2619–2623.
[22] Q. Wang, et al. Energy Environ. Sci. 7 (2014) 2359–2365.
[23] C. Bi, et al. Nat. Commun. 6 (2015) 7747.
[24] W.S. Yang, et al. Science 9272 (2015).
[25] H. Zhou, et al. Science 345 (2014) 542–546.
[26] J. You, et al. ACS Nano (2014) 1674–1680.
[27] K. Leo, Nat. Nanotechnol. 10 (2015) 574–575.

[28] C.C. Stoumpos, C.D. Malliakas, M.G. Kanatzidis, Inorg. Chem. 52 (2013) 9019–9038.
[29] G. Xing, et al. Nat. Mater. 13 (2014) 476–480.
[30] Q. Dong, et al. Science 347 (2015) 967–970.
[31] Z. Xiao, et al. Adv. Mater. 26 (2014) 6503–6509.
[32] G. Giorgi, J.-I. Fujisawa, H. Segawa, K. Yamashita, J. Phys. Chem. Lett. 4 (2013) 4213–4216.
[33] M.A. Green, A. Ho-Baillie, H.J. Snaith, Nat. Photon. 8 (2014) 506–514.
[34] O.-Y. Noriko, M. Takasuke, S. Hiroshi, J. Phys. Chem. Solids 53 (1992) 935–939.
[35] Miyata, A. et al. Direct Measurement of the Exciton Binding Energy and Effective Masses for Charge carriers in an Organic-Inorganic Tri-halide Perovskite. *arXiv preprint arXiv:1504.07025* (2015).
[36] W.-J. Yin, T. Shi, Y. Yan, Appl. Phys. Lett. 104 (2014) 063903.
[37] Z. Xiao, et al. Nat. Mater. 14 (2015) 193–198.
[38] Y. Kutes, et al. J. Phys. Chem. Lett. 5 (2014) 3335–3339.
[39] G.E. Eperon, et al. Energy Environ. Sci. 7 (2014) 982–988.
[40] W.J. Yin, T. Shi, Y. Yan, Adv. Mater. 26 (2014) 4653–4658.
[41] S. De Wolf, et al. J. Phys. Chem. Lett. 5 (2014) 1035–1039.
[42] J. Even, L. Pedesseau, J.-M. Jancu, C. Katan, J. Phys. Chem. Lett. 4 (2013) 2999–3005.
[43] W.-J. Yin, J.-H. Yang, J. Kang, Y. Yan, S.-H. Wei, J. Mater. Chem. A 3 (2015) 8926–8942.
[44] F. Zheng, H. Takenaka, F. Wang, N.Z. Koocher, A.M. Rappe, J. Phys. Chem. Lett. 6 (2014) 31–37.
[45] L.-C. Tang, C.-S. Chang, J.Y. Huang, J. Phys.: Condens. Matter 12 (2000) 9129.
[46] Q. Lin, A. Armin, R.C.R. Nagiri, P.L. Burn, P. Meredith, Nat. Photon. 9 (2015) 106–112.
[47] T. Kenichiro, et al. Solid State Commun. 127 (2003) 619–623.
[48] M.F. Jarvist, et al. Nano Lett. 14 (2014) 2584–2590.
[49] E.J. Juarez-Perez, et al. J. Phys. Chem. Lett. 5 (2014) 2390–2394.
[50] M. Hu, et al. Small 11 (2015) 2164–2169.
[51] J.M. Frost, K.T. Butler, A. Walsh, APL Mater. 2 (2014) 081506.
[52] R. Gottesman, et al. J. Phys. Chem. Lett. 6 (2015) 2332–2338.
[53] E. Mosconi, C. Quarti, T. Ivanovska, G. Ruani, F. Angelis, Phys. Chem. Chem. Phys. 16 (2014) 16137–16144.
[54] T. Baikie, N.S. Barrow, Y. Fang, P.J. Keenan, Mater. Chem. A 3 (2015) 9298–9307.
[55] Z. Fan, et al. J. Phys. Chem. Lett. 6 (2015) 1155–1161.
[56] R. Gottesman, et al. J. Phys. Chem. Lett. 5 (2014) 2662–2669.
[57] D.I. Valerio, et al. Nat. Commun. 5 (2014) 3586.
[58] D. Moses, J. Wang, A.J. Heeger, N. Kirova, S. Brazovski, Proc. Natl. Acad. Sci. U. S. A. 98 (2001) 13496–13500.
[59] D.S. Samuel, et al. Phys. Rev. Appl. 2 (2014) 034007.
[60] D. Shi, et al. Science 347 (2015) 519–522.
[61] I. Chung, et al. J. Am. Chem. Soc. 134 (2012) 8579–8587.
[62] C. Wehrenfennig, G.E. Eperon, M.B. Johnston, H.J. Snaith, L.M. Herz, Adv. Mater. 26 (2014) 1584–1589.
[63] Y. He, G. Galli, Chem. Mater. 26 (2014) 5394–5400.
[64] N.K. Noel, et al. Energy Environ. Sci. 7 (2014) 3061–3068.
[65] Y. Takahashi, H. Hasegawa, Y. Takahashi, T. Inabe, J. Solid State Chem. 205 (2013) 39–43.
[66] Y. Wang, Y. Zhang, P. Zhang, W. Zhang, Phys. Chem. Chem. Phys. 17 (2015) 11516–11520.
[67] Y. Mei, C. Zhang, Z. Vardeny, O. Jurchescu, MRS Commun. 5 (2015) 297–301.
[68] Chin, X.Y., Cortecchia, D., Yin, J., Bruno, A., Soci, C. Lead iodide perovskite light-emitting field-effect transistor. arXiv preprint arXiv:1501.04407 (2015).
[69] D.B. Mitzi, et al. Adv. Mater. 14 (2002) 1772–1776.
[70] C.S. Ponseca Jr., et al. J. Am. Chem. Soc. 136 (2014) 5189–5192.
[71] Z. Bao, J. Locklin, Organic Field-effect Transistors, CRC press, Boca Raton, 2007.
[72] T. Matsushima, K. Fujita, T. Tsutsui, Jpn. J. Appl. Phys. 43 (2004) L1199.
[73] D.B. Mitzi, J. Mater. Chem. 14 (2004) 2355–2365.
[74] D.B. Mitzi, C.D. Dimitrakopoulos, L.L. Kosbar, Chem. Mater. 13 (2001) 3728–3740.
[75] Y. Yuan, et al. Adv. Energ. Mater. 5 (2015) 1500615.
[76] W.J. Yin, H. Chen, T. Shi, S.H. Wei, Y. Yan, Adv. Electron. Mater. 1 (2015), http://dx.doi.org/10.1002/aelm.201500044.
[77] R. Dong, et al. Adv. Mater. 27 (2015) 1912–1918.
[78] S.M. Vorpahl, et al. Science 348 (2015) 683–686.
[79] T. Leijtens, et al. ACS Nano 8 (2014) 7147–7155.
[80] V. D'Innocenzo, et al. Nat. Commun. 5 (2014) 3586.
[81] W. Geng, L. Zhang, Y.-N. Zhang, W.-M. Lau, L.-M. Liu, J. Phys. Chem. C 118 (2014) 19565–19571.
[82] A. Zakutayev, et al. J. Phys. Chem. Lett. 5 (2014) 1117–1125.
[83] B. Suarez, et al. J. Phys. Chem. Lett. 5 (2014) 1628–1635.
[84] S. Zhang, S.-H. Wei, A. Zunger, H. Katayama-Yoshida, Phys. Rev. B 57 (1998) 9642.
[85] J. Kim, S.-H. Lee, J.H. Lee, K.-H. Hong, J. Phys. Chem. Lett. 5 (2014) 1312–1317.
[86] M.-H. Du, J. Mater. Chem. A 2 (2014) 9091–9098.
[87] Q. Wang, et al. Appl. Phys. Lett. 105 (2014) 163508.
[88] P. Schulz, et al. Energy Environ. Sci. 7 (2014) 1377–1381.
[89] B. Conings, et al. Adv. Mater. 26 (2014) 2041–2046.
[90] M.-H. Du, J. Phys. Chem. Lett. 6 (2015) 1461–1466.
[91] M.L. Agiorgousis, Y.-Y. Sun, H. Zeng, S. Zhang, J. Am. Chem. Soc. 136 (2014) 14570–14575.
[92] A. Buin, et al. Nano Lett. 14 (2014) 6281–6286.
[93] J. Xu, et al. Nat. Commun. 6 (2015) 7081.
[94] P.W. Liang, C.C. Chueh, S.T. Williams, A.K.Y. Jen, Adv. Energy Mater. (2015).
[95] K. Wojciechowski, et al. ACS Nano 8 (2014) 12701–12709.
[96] N.K. Noel, et al. ACS Nano 8 (2014) 9815–9821.
[97] T. Supasai, N. Rujisamphan, K. Ullrich, A. Chemseddine, T. Dittrich, Appl. Phys. Lett. 103 (2013) 183906.
[98] Q. Chen, et al. Nano Lett. 14 (2014) 4158–4163.
[99] L. Wang, C. McCleese, A. Kovalsky, Y. Zhao, C. Burda, J. Am. Chem. Soc. 136 (2014) 12205–12208.
[100] A. Dualeh, et al. Adv. Funct. Mater. 24 (2014) 3250–3258.
[101] G.E. Eperon, V.M. Burlakov, P. Docampo, A. Goriely, H.J. Snaith, Adv. Funct. Mater. 24 (2014) 151–157.
[102] N.J. Jeon, et al. Nature 517 (2015) 476–480.
[103] W. Nie, et al. Science 347 (2015) 522–525.
[104] J.H. Im, I.H. Jang, N. Pellet, M. Gratzel, N.G. Park, Nat. Nanotechnol. 9 (2014) 927–932.
[105] W.S. Yang, et al. Science 348 (2015) 1234.
[106] Q. Chen, et al. J. Am. Chem. Soc. 136 (2014) 622–625.
[107] F. Hao, C.C. Stoumpos, Z. Liu, R.P. Chang, M.G. Kanatzidis, J. Am. Chem. Soc. 136 (2014) 16411–16419.
[108] Y. Li, et al. J. Phys. Chem. Lett. 6 (2015) 493–499.
[109] Y. Deng, et al. Energy Environ. Sci. 8 (2015) 1544–1550.
[110] K. Hwang, et al. Adv. Mater. 27 (2015) 1241–1247.
[111] J.H. Kim, S.T. Williams, N. Cho, C.-C. Chueh, A.K.Y. Jen, Adv. Energy Mater. 5 (2015) 1401229.
[112] Z. Yang, et al. Adv. Energy Mater. 5 (2015) 1500328.
[113] A.T. Barrows, et al. Energy Environ. Sci. 7 (2014) 2944.
[114] S. Das, et al. ACS Photon. 2 (2015) 680–686.
[115] G.E. Eperon, V.M. Burlakov, P. Docampo, A. Goriely, H.J. Snaith, Adv. Funct. Mater. 24 (2013) 151–157.
[116] R.F. Service, Science 342 (2013) 794–797.
[117] M. Xiao, et al. Angew. Chem. 126 (2014) 10056–10061.
[118] N.J. Jeon, et al. Nat. Mater. 13 (2014) 897–903.
[119] Z. Xiao, et al. Adv. Mater. 26 (2014) 3068–3075.
[120] J. Peet, et al. Nat. Mater. 6 (2007) 497–500.
[121] Y. Sun, et al. Nat. Mater. 11 (2012) 44–48.
[122] C.-C. Chueh, et al. J. Mater. Chem. A: Mater. Energy Sustain. 16 (2014) 9058–9062.
[123] P.W. Liang, et al. Adv. Mater. 26 (2014) 3748–3754.
[124] F. Wang, H. Yu, H. Xu, N. Zhao, Adv. Funct. Mater. 25 (2015) 1120–1126.
[125] J.H. Heo, et al. Adv. Mater. 27 (2015) 3424–3430.
[126] H.-B. Kim, et al. Nanoscale 6 (2014) 6679–6683.
[127] Y.-J. Jeon, et al. Sci. Rep. 4 (2014) 6953.
[128] C.-Y. Chang, et al. ACS Appl. Mater. Interfaces 7 (2015) 4955–4961.
[129] W. Zhang, et al. Nat. Commun. 6 (2015) 6142.
[130] D.T. Moore, H. Sai, K.W. Tan, L.A. Estroff, U. Wiesner, APL Mater. 2 (2014) 081802.
[131] E.L. Unger, et al. Chem. Mater. 26 (2014) 7158–7165.
[132] L. Zuo, et al. J. Am. Chem. Soc. 137 (2015) 2674–2679.
[133] Y. Ogomi, et al. J. Phys. Chem. C 118 (2014) 16651–16659.
[134] D. Sanjib, et al. ACS Photon. 2 (2015) 680–686.
[135] X.P. Cui, et al. Chem. Commun. (Camb.) 51 (2015) 1457–1460.
[136] G. Li, et al. Nat. Mater. 4 (2005) 864–868.
[137] G. Li, et al. Adv. Funct. Mater. 17 (2007) 1636.
[138] J. You, et al. Appl. Phys. Lett. 105 (2014) 183902.
[139] Z. Zhou, et al. Angew. Chem. Int. Ed. 54 (2015) 9705–9709.
[140] E. Edri, et al. Nat. Commun. 5 (2014) 3461.
[141] E. Edri, et al. Nano Lett. 14 (2014) 1000–1004.
[142] P. Docampo, et al. Adv. Energy Mater. 4 (2014) 1400355.
[143] S. Colella, et al. Chem. Mater. 25 (2013) 4613–4618.
[144] Y. Zhao, K. Zhu, J. Phys. Chem. C 118 (2014) 9412–9418.
[145] E.L. Unger, et al. Chem. Mater. 26 (2014) 7158–7165.
[146] H. Yu, et al. Adv. Funct. Mater. 24 (2014) 7102–7108.
[147] S. Colella, et al. J. Phys. Chem. Lett. 5 (2014) 3532–3538.
[148] S.T. Williams, et al. ACS Nano 8 (2014) 10640–10654.
[149] M.I. Dar, et al. Nano Lett. 14 (2014) 6991–6996.
[150] Q. Dong, et al. Energy Environ. Sci. 8 (2015) 2464–2470.
[151] Z.-K. Tan, et al. Nat. Nanotechnol. 9 (2014) 687–692.
[152] W. Ke, et al. Nat. Commun. 6 (2015) 6700.
[153] A. Mei, et al. Science 345 (2014) 295–298.
[154] W.A. Laban, L. Etgar, Energy Environ. Sci. 6 (2013) 3249–3253.
[155] K. Mahmood, B.S. Swain, A. Amassian, Adv. Mater. 27 (2015) 2859–2865.
[156] T. Leijtens, et al. Nat. Commun. 4 (2013) 2885.
[157] W.S. Yang, et al. Science (2015) (aaa9272).
[158] J.T.-W. Wang, et al. Nano Lett. 14 (2013) 724–730.
[159] Z. Zhu, et al. J. Am. Chem. Soc. 136 (2014) 3760–3763.
[160] D. Liu, T.L. Kelly, Nat. Photon. 8 (2014) 133–138.
[161] W. Ke, et al. J. Am. Chem. Soc. 137 (2015) 6730–6733.
[162] S.S. Shin, et al. Nat. Commun. 6 (2015) 7410.
[163] O. Malinkiewicz, et al. Nat. Photon. 8 (2014) 128–132.
[164] Y. Shao, Z. Xiao, C. Bi, Y. Yuan, J. Huang, Nat. Commun. 5 (2014) 5784.
[165] S. Kazim, et al. Energy Environ. Sci. 8 (2015) 1816–1823.
[166] N. Ahn, et al. J. Am. Chem. Soc. 137 (2015) 8696–8699.
[167] K.G. Lim, et al. Adv. Mater. 26 (2014) 6461–6466.
[168] D. Zhao, et al. Adv. Energy Mater. 5 (2015) 1401855.
[169] J.H. Heo, D.H. Song, S.H. Im, Adv. Mater. 26 (2014) 8179–8183.
[170] Q. Wang, C. Bi, J. Huang, Nano Energy 15 (2015) 275–280.
[171] J.Y. Jeng, et al. Adv. Mater. 26 (2014) 4107–4113.
[172] K.-C. Wang, et al. Sci. Rep. 4 (2014) 4756.
[173] Z. Zhu, et al. Angew. Chem. 126 (2014) 12779–12783.

[174] J.H. Kim, et al. Adv. Mater. 27 (2015) 695–701.
[175] Y. Zhao, A.M. Nardes, K. Zhu, Appl. Phys. Lett. 104 (2014) 213906.
[176] J.A. Christians, R.C. Fung, P.V. Kamat, J. Am. Chem. Soc. 136 (2013) 758–764.
[177] P. Qin, et al. Nat. Commun. 5 (2014) 3834.
[178] W. Chen, et al. Science 350 (2015) 944–948.
[179] S. Liu, et al. J. Phys. Chem. Lett. 6 (2015) 693–699.
[180] J.M. Frost, et al. Nano Lett. 14 (2014) 2584–2590.
[181] S. Dall'Olio, R. Dovesi, R. Resta, Phys. Rev. B 56 (1997) 10105.
[182] F. Zheng, H. Takenaka, F. Wang, N.Z. Koocher, A.M. Rappe, J. Phys. Chem. Lett. 6 (2015) 31–37.
[183] J. Wei, et al. J. Phys. Chem. Lett. 5 (2014) 3937–3945.
[184] L. Pintilie, M. Alexe, Appl. Phys. Lett. 87 (2005) 112903.
[185] J. Scott, J. Phys. Condens. Matter 20 (2008) 021001.
[186] N. Balke, et al. Nano Lett. 12 (2012) 3399–3403.
[187] C. Bark, et al. Nano Lett. 12 (2012) 1765–1771.
[188] D.B. Strukov, G.S. Snider, D.R. Stewart, R.S. Williams, Nature 453 (2008) 80–83.
[189] S. van Reenen, M. Kemerink, H.J. Snaith, J. Phys. Chem. Lett. 6 (2015) 3808–3814.
[190] Y. Zhao, et al. Energy Environ. Sci. 8 (2015) 1256–1260.
[191] Y. Yuan, et al. Adv. Energy Mater. (2015), http://dx.doi.org/10.1002/aenm.201501803.
[192] del Cueto, J.A., Deline, C., Albin, D., Rummel, S., Anderberg, A. Proceedings of the SPIE Solar Energy + Technology, 741204-741204-741212. International Society for Optics and Photonics.
[193] M. Herman, M. Jankovec, M. Topič, Int. J. Photoenergy 2012 (2012) 151452.
[194] E. Unger, et al. Energy Environ. Sci. 7 (2014) 3690–3698.
[195] H.-S. Kim, N.-G. Park, J. Phys. Chem. Lett. 5 (2014) 2927–2934.
[196] V. Shrotriya, et al. Adv. Funct. Mater. 16 (2006) 2016–2023.
[197] S. Ito, et al. Prog. Photovolt.: Res. Appl. 14 (2006) 589–601.
[198] G. Hodes, J. Phys. Chem. Lett. 3 (2012) 1208–1213.
[199] H.J. Snaith, Energy Environ. Sci. 5 (2012) 6513–6520.
[201] J.A. Christians, J.S. Manser, P.V. Kamat, J. Phys. Chem. Lett. 6 (2015) 852–857.
[202] K. Masuko, et al. Photovolt. IEEE J. 4 (2014) 1433–1435.
[203] M.A. Green, K. Emery, Y. Hishikawa, W. Warta, E.D. Dunlop, Prog. Photovolt.: Res. Appl. 23 (2015) 1–9.
[204] A. Richter, M. Hermle, S.W. Glunz, Photovolt. IEEE J. 3 (2013) 1184–1191.
[205] C.D. Bailie, et al. Energy Environ. Sci. 8 (2015) 956–963.
[206] M. Graetzel, R.A.J. Janssen, D.B. Mitzi, E.H. Sargent, Nature 488 (2012) 304–312.
[207] W.S. Yang, et al. Science 348 (2015) 1234–1237.
[208] C. Bi, Y. Yuan, Y. Fang, J. Huang, Adv. Energy Mater. 5 (2015) 1401616.
[209] P. Loper, et al. Phys. Chem. Chem. Phys. 17 (2015) 1619–1629.
[210] L. Kranz, et al. J. Phys. Chem. Lett. 6 (2015) 2676–2681.
[211] F. Fu, et al. Nat. Commun. 6 (2015) 8932.
[212] H. Uzu, et al. Appl. Phys. Lett. 106 (2015) 013506.
[213] T. Todorov, T. Gershon, O. Gunawan, C. Sturdevant, S. Guha, Appl. Phys. Lett. 105 (2014) 173902.
[214] C.-C. Chen, et al. Mater. Horiz. 2 (2015) 203–211.
[215] J.P. Mailoa, et al. Appl. Phys. Lett. 106 (2015) 121105.
[216] P. You, Z. Liu, Q. Tai, S. Liu, F. Yan, Adv. Mater. 27 (2015) 3632–3638.
[217] A. Colsmann, et al. Adv. Energy Mater. 1 (2011) 599–603.
[218] G. Li, C.-W. Chu, V. Shrotriya, J. Huang, Y. Yang, Appl. Phys. Lett. 88 (2006) 253503.
[219] J.-Y. Lee, S.T. Connor, Y. Cui, P. Peumans, Nano Lett. 10 (2010) 1276–1279.
[220] C.-C. Chen, et al. ACS Nano 6 (2012) 7185–7190.
[221] J. Czolk, et al. Adv. Energy Mater. 3 (2013) 386–390.
[222] A. Colsmann, et al. Sol. Energy Mater. 98 (2012) 118–123.
[223] Y.-Y. Lee, et al. ACS Nano 5 (2011) 6564–6570.
[224] Z. Liu, et al. ACS Nano 6 (2012) 810–818.
[225] X. Xia, et al. J. Mater. Chem. 20 (2010) 8478–8482.
[226] Y.H. Kim, et al. Sol. Energy Mater. 96 (2012) 244–250.
[227] C. Roldan-Carmona, et al. Energy Environ. Sci. 7 (2014) 2968–2973.
[228] E. Della Gaspera, et al. Nano Energy 13 (2015) 249–257.
[229] Y. Yang, et al. ACS Nano 9 (2015) 7714–7721.
[230] F. Guo, et al. Nanoscale 7 (2015) 1642–1649.
[231] D. Bryant, et al. Adv. Mater. 26 (2014) 7499–7504.
[232] T.-B. Song, et al. J. Mater. Chem. A 3 (2015) 9032–9050.
[233] I.C. Smith, E.T. Hoke, D. Solis-Ibarra, M.D. McGehee, H.I. Karunadasa, Angew. Chem. 126 (2014) 11414–11417.
[234] J.H. Noh, S.H. Im, J.H. Heo, T.N. Mandal, S.I. Seok, Nano Lett. 13 (2013) 1764–1769.
[235] A. Binek, F.C. Hanusch, P. Docampo, T. Bein, J. Phys. Chem. Lett. 6 (2015) 1249–1253.
[236] Y. Deng, Z. Xiao, J. Huang, Adv. Energy Mater. (2015), http://dx.doi.org/10.1002/aenm.201500721.
[237] E.T. Hoke, et al. Chem. Sci. 6 (2015) 613–617.
[238] S.N. Habisreutinger, et al. Nano Lett. 14 (2014) 5561–5568.
[239] H. Choi, et al. Nat. Commun. 6 (2015) 7348.
[240] J. You, et al. Nat. Nanotechnol. (2015), http://dx.doi.org/10.1038/nnano.2015.1230.